CONFINEMENT STUDIES ON ASDEX

F. Wagner

IPP III/131 Februar 1988

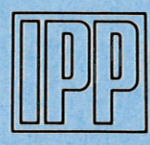

MAX-PLANCK-INSTITUT FÜR PLASMAPHYSIK

8046 GARCHING BEI MÜNCHEN

MAX-PLANCK-INSTITUT FÜR PLASMAPHYSIK

GARCHING BEI MÜNCHEN

CONFINEMENT STUDIES ON ASDEX

F. Wagner

IPP III/131 Februar 1988

HABILITATIONSSCHRIFT
zur
Erlangung der Venia legendi
für das Fach Physik
der
Ruprecht-Karls-Universität Heidelberg

Die nachstehende Arbeit wurde im Rahmen des Vertrages zwischen dem Max-Planck-Institut für Plasmaphysik und der Europäischen Atomgemeinschaft über die Zusammenarbeit auf dem Gebiete der Plasmaphysik durchgeführt.

Introduction

The aim of fusion oriented plasma research is the study and the understanding of hot plasma behaviour with the technological goal of ultimately providing the conditions for a burning plasma. The parameters which have to be achieved are well known: the product of density and energy confinement time has to be $2*10^{14} cm^{-3} s$ at an average plasma temperature of 10 keV. These two parameters have been reached separately: the temperature at a low confinement product and the confinement product at too low a temperature. The simultaneous attainment of both requirements was found to be difficult. The effort to increase the plasma temperature in a tokamak plasma gave rise to a severe degradation of confinement with the net result of no effective approach to the break-even conditions.

The energy confinement time in the present generation of large tokamak plasmas with auxiliary heating is largely determined by conductive heat transport predominantly by the plasma electrons. The measured electron heat transport is considerably larger than one calculates assuming the transport is dominated by a diffusive process determined by electron scattering with the gyro-radius in the toroidal or poloidal magnetic field as the step size. The actual heat conductivity in a tokamak plasma is dominated by the additional transport due to fluctuating electric and magnetic fields caused by plasma instabilities. The exploration of the mechanisms which give rise to the anomalously enhanced transport is one of the main topics in tokamak research. The lack of understanding prevents well founded predictions of the performance of future experimental devices and is the main reason for the still existing uncertainty about the feasibility of a burning plasma.

This report deals with investigations of plasma confinement carried out on the ASDEX divertor tokamak. It is comprised of two sections: the first section deals with the study of the confinement degradation in auxiliary heated discharges; in the second section a regime will be described where the severe deterioration of the confinement quality at high heating power is avoided. This regime is called the H-mode because of the high confinement charateristics in contrast to the low confinement L-mode. There is evidence that the L-mode charateristics will not lead to sufficient confinement quality for successful plasma burning. The H-mode was observed for the first time on ASDEX. At present it is considered as the confinement regime with the best prospects for future tokamak operation. But both the study of L- and H-mode confinement physics have increased our understanding on energy transport in tokamaks.

PART A: L-MODE STUDIES

TABLE OF CONTENTS

I. Introduction

This paper describes energy confinement properties observed in ASDEX at low auxiliary heating power in the transitional range from ohmic heating to the L-regime. Most of the results are obtained with neutral injection (NI) heating but the most important aspects are backed by results obtained alternatively with ion cyclotron resonance heating (ICRH). ASDEX was operated in the standard double-null divertor configuration (R=1.65 m, a=0.4 m). The varied parameters are the heating power (which can be changed in the case of NI in steps of ~0.5 MW; the upper power limit for the present investigations is generally 2 MW, to avoid H-mode transitions), line-averaged density ($1.5 < \bar{n}_e < 7 \times 10^{13}$ cm^{-3}), plasma current ($0.2 < I_p < 0.45$ MA) and hydrogen species mix ($H^0 \rightarrow H^+$ and $H^0 \rightarrow D^+$). The toroidal magnetic field was fixed at 2.2 T. The NI beam energy was 42 keV; the sources are oriented tangentially in the co-direction; ICRH was applied at $2\Omega_{CH}$ (67 MHz) to pure hydrogen plasmas and in some cases to H^+/D^+ mixtures or as minority heating D(H) in deuterium plasmas with a hydrogen minority (33.5 MHz).

The first section describes the roles of the various external parameters in confinement under ohmic and auxiliary heating conditions. In particular, the importance of the heating power and plasma current is documented. Heating power leads to the known degradation of confinement, while high plasma current improves it. Experiments are described in which the local heating power was varied, leading to local changes of plasma confinement. It is argued that already the ohmic heating power causes confinement degradation, which with auxiliary heating continues into the L-regime. The effect of the plasma current is introduced through the shape of the plasma profiles, being the same under ohmic and auxiliary heating conditions. Ohmic heating creates a degenerate situation insofar as the beneficial effect of higher current is compensated by the higher ohmic heating power. This degeneration is removed under auxiliary heating conditions. As in other auxiliary-heated tokamaks, a discontinuity is observed in the slope of the energy content W versus the heating power P at the transition from ohmic to auxiliary heating /1, 2, 3, 4/. The discontinuity is due to the different ways the plasma current changes in a power scan: with beam heating I_p is generally constant; under ohmic conditions I_p rises roughly proportionally to the power.

In the second section we study the scaling of the confinement time in the intermediate power range. The degradation with power can be described by an

offset-linear relation

$$W = W_{oh} + \tau_{inc}/(P-P_{OH}) \quad \text{(equ. 1)}$$

(W_{oh} = energy of the ohmic target plasma, τ_{inc}= incremental confinement time) /2, 3, 4/. The remaining density dependence of the global energy confinement time

$$\tau_E = W/(P-\dot{W})$$

is introduced via W_{oh}; τ_{inc} is found to increase linearly with the plasma current and also depends on the isotope mass (deuterium being better than hydrogen). With these assumptions the transition in τ_E from ohmic heating to auxiliary heating can well be described.
In the final section the role of the electron temperature T_e and the T_e gradient - their increase with power could be responsible for the degradation of confinement - are studied.

2. Description of different confinement regimes

2.1. The ohmic linear regime

At low density the global energy confinement time of ohmically heated plasmas is known to increase linearly with the line-averaged density. There may be an additional q_a dependence in the linear regime in favour of high-q_a, low-current discharges /5, 6/.

2.2. Degraded regimes

At higher densities τ_E saturates. In the case of ASDEX the roll-over occurs at $\bar{n}_e = 3\times10^{13}$ cm^{-3} in deuterium or helium plasmas at $\tau_E = 90$ ms. The transition density corresponds to a Murakami parameter of about 2.5. The saturation regime is only accessible if the density limit is sufficiently high. In ohmic gas-fuelled plasmas Murakami parameters of up to 7.2 have been achieved in ASDEX /1/. In the saturation regime τ_E has a tendency to decrease slightly with density. No pronounced I_p or B_t dependence is observed at high density.
Auxiliary heating is known to degrade the confinement (the corresponding confinement regime is termed L-mode), irrespective of whether it is applied to an ohmic target plasma in the linear or saturation regime. At 3MW, τ_E in the L-mode of ASDEX is in the range of 25-35 ms /7/. τ_E depends on the heating power in the form of a power law ($\tau_E \propto P^{-\alpha}$) or in the form $\tau_E = a+b/P$. There is accumulating evidence that the linear offset description fits the data better and in ASDEX it seems to describe the ICRH data well /8/; the situation with NI is not yet so clear. Further important scaling

results of auxiliary-heated discharges are the proportionality of τ_E to the plasma current I_p and the lack of density dependence. No element of the ohmic confinement scaling seems to be preserved with auxiliary heating. The change of parameter scaling with auxiliary heating is the subject of Section 4.

2.3. Improved confinement regimes

The degradation of confinement with auxiliary heating is not inevitable. Under ohmic conditions the replacement of gas-puff refuelling by pellet injection leads to improved confinement. At line densities deep in the saturation regime, τ_E can be as high as 150 ms /9/. The pellet results demonstrate that the ohmic saturation regime is indeed a regime of degraded confinement. A characteristic feature of the pellet regime are peaked density profiles (the density profile parameter $n_{eo}/\langle n_e \rangle$ increases from 1.7 with gas-puff to 3.1 with pellets). With auxiliary heating the confinement degradation can largely be avoided by operating under conditions which allow the H-mode /10/. In the case of ASDEX, τ_E values are typically a factor of 2 above the L-mode ones and are comparable to the ohmic values. τ_E in the H-mode also increases linearly with the plasma current and does not exhibit ohmic scaling features.

Figure 1 plots the ohmic τ_E scaling with density for deuterium and hydrogen plasmas with gas puffing and shows the transition from linear dependence to saturation. The gas-puff results are compared with those obtained with pellet refuelling (deuterium pellets into a deuterium plasma). Figure 2 plots τ_E of NI and ICRF-heated plasmas versus power as an example of L-mode behaviour with various heating methods.

3. The effect of external parameters on confinement

In the following, we first discuss how the parameters set from the outside, such as the auxiliary heating power, plasma current, and density, affect plasma profiles, confinement and energy content. In the case of ohmic heating, the heating power P_{oh} is not an independent quantity but is determined by T_e and Z_{eff}. Nevertheless we include P_{oh} in the present considerations.

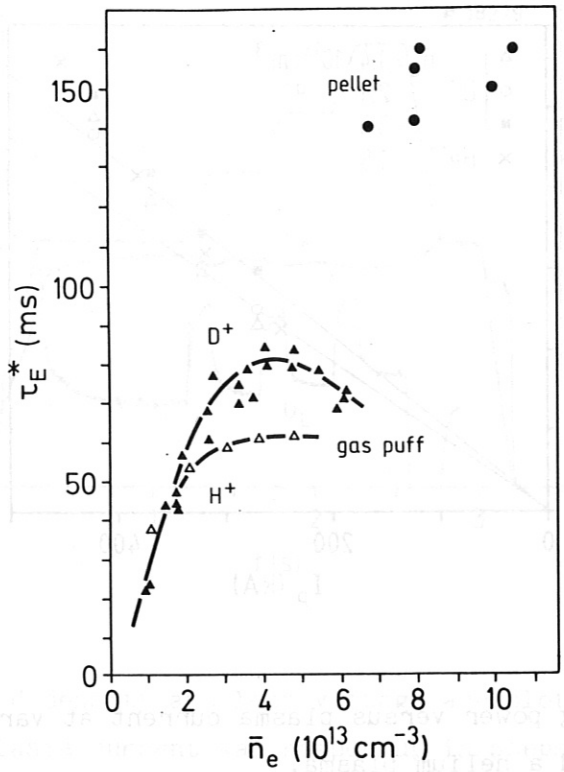

Fig. 1 The global energy confinement time (measured diamagnetically) versus density in ohmically heated plasmas with gas puff and pellet refuelling. B_T = 2.2 T, gas-puff: I_p = 420 kA, pellet: I_p = 380 kA.

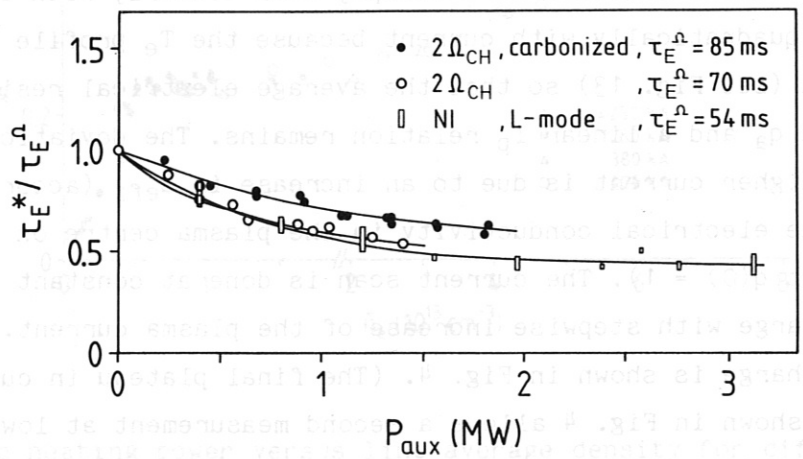

Fig. 2 The global energy confinement time normalized to the ohmic value versus auxiliary heating power for ICRH and NI heated plasmas. The differences in τ_E^{Ω} are due to various isotope mixtures.

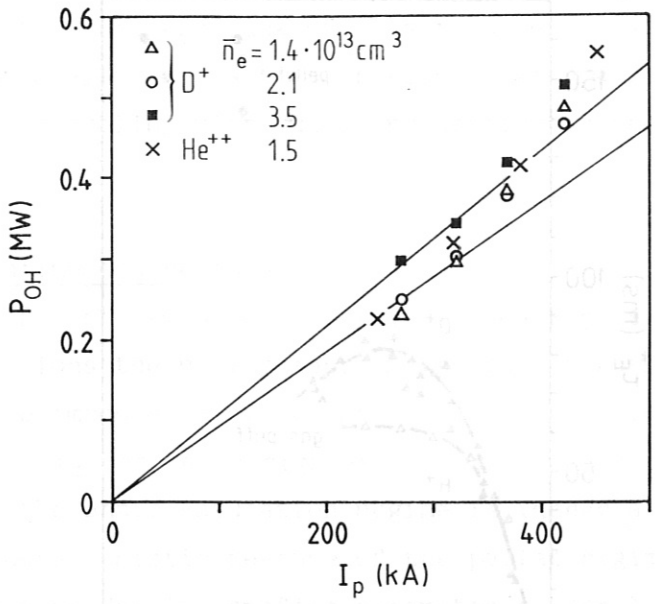

Fig. 3 Ohmic heating power versus plasma current at various densities for deuterium and a helium plasma.

3.1. Heating power

Ohmic heating: The ohmic heating power is most easily changed via the plasma current. In Fig. 3 P_{oh} is plotted versus the plasma current for discharges of various densities for deuterium and for a low-density helium plasma. P_{oh} increases somewhat more steeply than linearly with current. P_{oh} does not rise quadratically with current because the T_e profile broadens in a current scan (see Fig. 13) so that the average electrical resistivity decreases with q_a and a linear I_p relation remains. The deviation from linearity at higher current is due to an increase in Z_{eff} (according to the analysis of the electrical conductivity in the plasma centre on the assumption that $q(0) = 1$). The current scan is done at constant density in a single discharge with stepwise increase of the plasma current. An example of such a discharge is shown in Fig. 4. (The final plateau in current of the discharge shown in Fig. 4 allows a second measurement at low current to monitor any uncontrolled changes during the current scan.)

Another way to change the ohmic input power is via density. Figure 5 plots P_{oh} as a function of the line density in a wide density range for different current values. The actual data are given for the 280 kA series; to allow better comparison, the results at other current values are linearly scaled

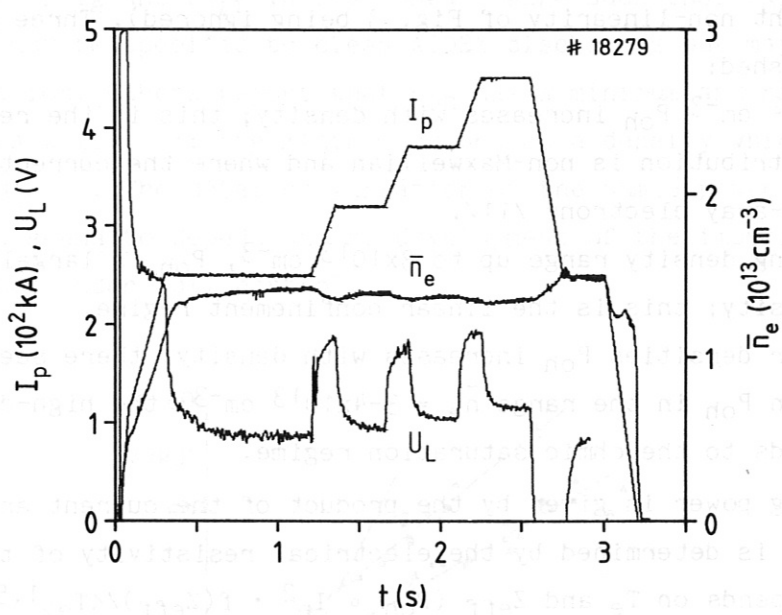

Fig. 4 Line averaged density and loop voltage are plotted for a discharge where the plasma current was ramped up in steps to allow for current scans in a single discharge.

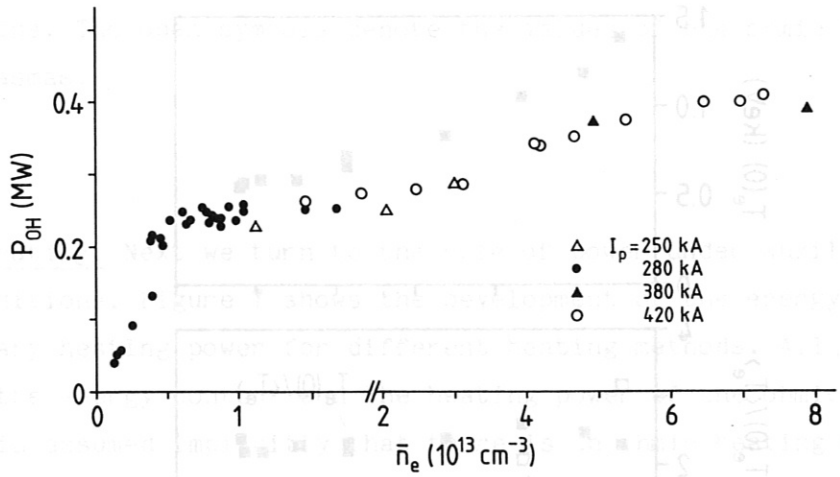

Fig. 5 Ohmic heating power versus line average density for different plasma current values. The absolute values of P_{OH} correspond to the 280 kA series. The other current scans are linearly scaled to the 280 kA series. Note the change in scale in the abscissa at $\bar{n}_e = 2 \times 10^{13}$ cm^{-3}.

(the actual slight non-linearity of Fig. 3 being ignored). Three regimes can be distinguished:

- For $\bar{n}_e < 6x10^{12}$ cm^{-3} P_{oh} increases with density; this is the regime where the electron distribution is non-Maxwellian and where the current is carried by slide-away electrons /11/.
- In the following density range up to $3x10^{13}$ cm^{-3}, P_{oh} is largely independent of density; this is the linear confinement regime.
- For even higher densities P_{oh} increases with density; there seems to be a step-like rise in P_{oh} in the range $\bar{n}_e = 3\text{-}4x10^{13}$ cm^{-3}; the high-density regime corresponds to the ohmic saturation regime.

The ohmic heating power is given by the product of the current and loop voltage V_l which is determined by the electrical resistivity of the discharge, which depends on T_e and Z_{eff} ($P_{oh} \propto I_p^2 \cdot f(Z_{eff})/\langle T_e \rangle^{1.5}$ (equ. 2)). The constituents of equ.2 are plotted in Fig. 6 for various densities at constant current. Both $T_e(0)$ and Z_{eff} decrease with rising density. There is a smooth transition in $T_e(0)$ from the linear to the saturation regime; the T_e profile parameter $T_e(0)/\langle T_e \rangle$ does not change but Z_{eff} is close to 1 at the transition. In the linear regime the effects of decreasing T_e and Z_{eff} on P_{oh} just cancel; when Z_{eff} has reached 1, further decrease of T_e causes the electrical resistivity to rise, and the ohmic power input along with it.

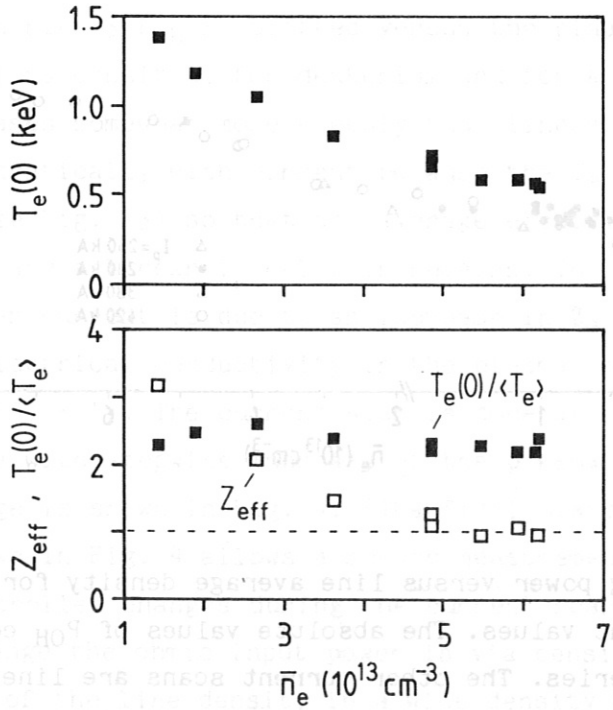

Fig. 6 The central electron temperature $T_e(0)$, Z_{eff} and the T_e-profile shape parameter $T_e(0)/\langle T_e \rangle$ for an ohmic density scan.

The variation of T_e and Z_{eff} in the linear range such that P_{oh} is constant (see Fig. 5) may be specific to clean ASDEX discharges but may not be the general situation. Others report that P_{oh} has a minimum and rises towards low density as well /13/; the minimum occurs at a density which depends on the plasma current. The detailed variation of the ohmic power input in the linear regime seems to depend on the development of the impurity concentration and is not under full control.

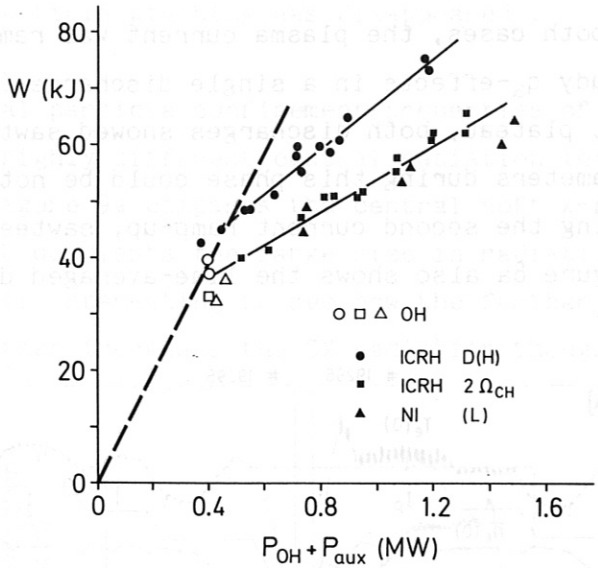

Fig. 7 Energy content versus total heating power for ICRH and NI power scans. The open symbols denote the values of the ohmic target plasmas.

Auxiliary heating: Next we turn to the role of power under auxiliary heating conditions. Figure 7 shows the development of the energy content with auxiliary heating power for different heating methods. All curves start with the energy content and the heating power of the ohmic target plasma. It is assumed implicitly that there is an ohmic heating relation given by the connection line of the ohmic point and the origin. The degradation of confinement causes a deviation from the "ohmic curve"; it sets in as soon as auxiliary heating begins, even at low heating power levels and causes the energy content to rise with a reduced slope. This reduction in slope of the W vs. P trace which corresponds to a power-dependent global confinement time τ_E is caused by an increase of the thermal transport coefficients of the auxiliary-heated plasma in the L-phase /12/.

In order to illustrate the importance of the heating power for confinement in more detail, we describe three experimental situations which reveal the role of power flux for confinement.

The role of the power flux: The first example deals with the role of heating power in ohmic plasmas. We compare two successive ohmic discharges with identical plasma setting from the external controls but one with sawteeth (the common case) and the other without sawtooth relaxations in the plasma core. In both cases, the plasma current was ramped up to three plateau values to study q_a-effects in a single discharge (see Fig. 8a). In the first low-current plateau, both discharges showed sawteeth. Practically identical plasma parameters during this phase could be noted in all diagnostic channels. During the second current ramp-up, sawteeth were lost in discharge #19295. Figure 8a also shows the line-averaged density along two

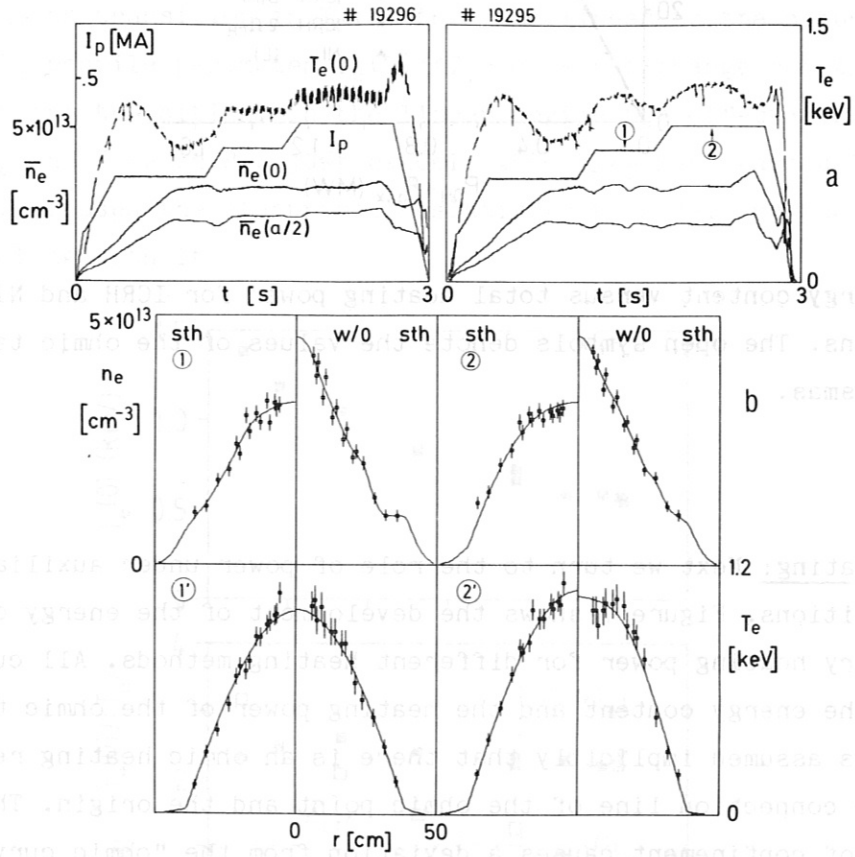

Fig. 8 a) Plasma current I_p, central temperature $T_e(0)$ and line averaged density $\bar{n}_e$ along two horizontal chords for a sawtoothing (w sth, #19296) and a sawtooth-free (w/0 sth, #19295) discharge.
b) Electron temperature and density profiles are shown for the two moments marked by 1 and 2 in the upper right picture.

horizontal chords (z = 0, z = 21 cm) and the central ECE electron temperature traces (indicating the different sawtooth behaviour). In all plateau phases, steady-state conditions are obtained apart from slight density oscillations in the case without sawteeth. Figure 8b compares the Thomson T_e and n_e profiles for two q_a values. With and without sawteeth, the T_e profiles are nearly identical, while the density profiles sharply peak without sawteeth, indicating an enhanced ratio of effective inward velocity /14/ to particle diffusion coefficient (because the sawtooth activity counteracting the particle pinching has disappeared).

The different central particle confinement properties of the two discharge types give rise to highly different central radiation levels (mostly by iron impurities). Figure 9a compares the central soft X-ray radiation for the two cases, which documents the large rise in radiation as soon as sawteeth are lost. It is interesting to see how the further reduction of q_a at the plasma edge further increases the SX radiation though there is no

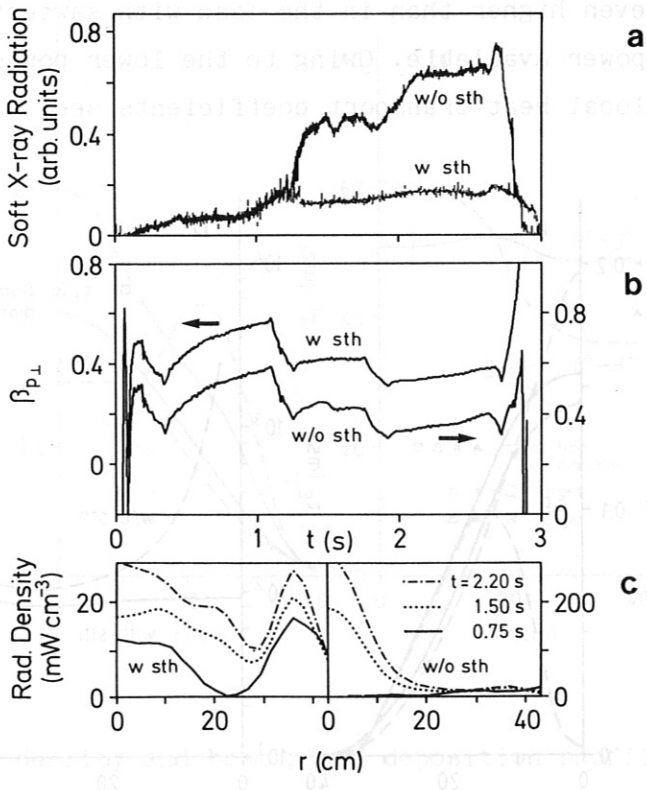

Fig. 9 Soft X-ray radiation along a chord through the plasma center (a), $\beta_{p_\perp}$ (b), and bolometrically measured impurity radiation density profiles (c) at the three current plateaus for the two cases with and without sawteeth.

indication that in this phase the impurity influx is enhanced. (The discharge with sawteeth does not show any significant change.) Figure 9b compares the two diamagnetically measured β_p traces, which are practically identical. The bolometrically measured radiation density is plotted in Fig. 9c for the two cases. In spite of the large radiation in the case without sawteeth, the energy content is the same for the two cases and in spite of the large central radiation the central electron energy density remains high and stationary. (The T_e drop shown in Fig. 8a in the later phase of the third plateau is caused by the sudden density increase.)

In Fig. 10a the radial variations of the energy density and actual heating power density (defined as ohmic minus radiation power density) and in Fig. 10b the radial variation of the energy confinement time τ_E are plotted ($\tau_E(r)=_o\int^r Er'dr'/_o\int^r pr'dr'$; as the ion temperature profile is not measured, it is assumed that the ion energy density is 0.9 of that of the electrons). In the case without sawteeth , the impurity radiation causes a reduction of the central heating power; nevertheless the central electron energy density is even higher than in the case with sawteeth in spite of the lower heating power available. Owing to the lower power flow in the plasma centre the local heat transport coefficients seem to be reduced.

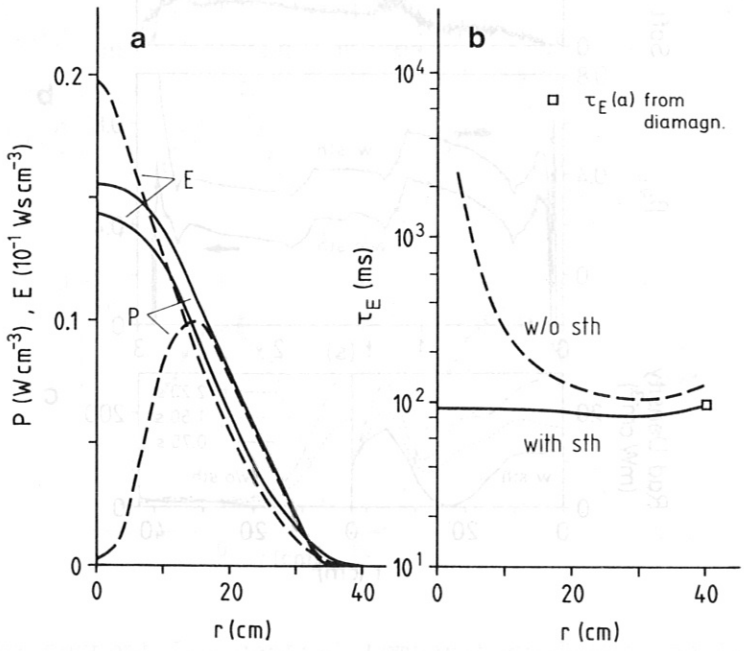

Fig. 10 a) Radial profiles of energy- and heating power density for the discharges shown in Fig. 9 with (solid) and without (dashed) sawteeth.

b) The corresponding τ_E profiles.

This results in an increase of the central confinement time such that a high and stationary energy density can be maintained for several global confinement times /15/. The case with impurity radiation has the somewhat higher global confinement time when the correction for impurity radiation is made. The global τ_E values from the diamagnetic measurement coincide for the two cases (no correction for impurity radiation). The symbol in Fig. 10b denotes the global τ_E values. Without further analysis it is obvious that in the sawtooth-free case the anomalous plasma transport is improved because the power flux to be transported is reduced by a large amount owing to the impurity radiation out of the core volume, where the heating power is deposited.

Another example which illustrates the role of power flux for confinement in the case of NI is the comparison of the central and off-axis power deposition /16/. The beam power deposition profile is varied by changing the voltage of the neutral injector sources. In one case 42 keV (high velocity) hydrogen is injected into a deuterium plasma of $\bar{n}_e = 5 \times 10^{13}$ cm^{-3}; in the

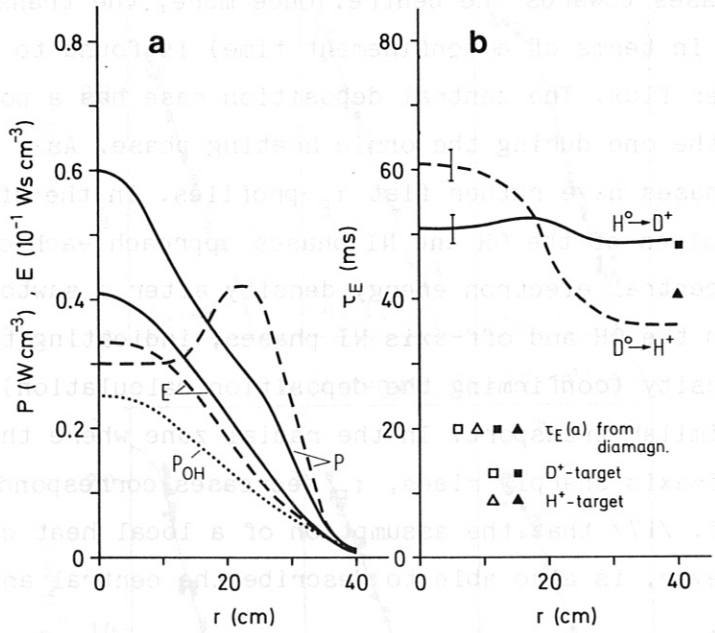

Fig. 11 a) Energy-density and beam power deposition profiles for central (solid lines; $H^o \rightarrow D^+$, 42 keV) and off-axis (dashed line, $H^o \rightarrow D^+$, 29 keV) deposition; $\bar{n}_e = 5 \times 10^{13}$ cm^{-3}, $I_p = 0.44$ MA. The dotted curve is the ohmic power during NI.
b) Radial dependence of the global energy confinement time for the two cases; the symbols represent the values from the diamagnetic loop.

other case, deuterium beams at 29 keV (low velocity) are injected into a hydrogen plasma of the same plasma density and at the same heating power. All other plasma parameters are kept constant. Different species of plasma and beam are chosen to allow determination of ion temperature profiles (by passive charge exchange), but at the cost of different global confinement times with $\tau_E(H^+) < \tau_E(D^+)$. All relevant plasma profiles are well documented for the two cases; the deposition profiles are calculated (see Fig. 11a). The difference in central power deposition to the electrons is reflected in a different rate of central electron energy density rise after a sawtooth drop. Figure 11a shows the energy density and the total beam power deposition profiles for the two cases; Fig. 11b plots the profiles of the local energy confinement times $\tau_E(r)$ during the beam heating phases. The symbols denoting the global τ_E values are obtained from diamagnetic measurements. The global τ_E values differ because of the isotope dominance of the respective target plasma.

In the case of off-axis deposition, where the power flow in the plasma core is low, τ_E increases towards the centre. Once more, the transport coefficient (expressed in terms of a confinement time) is found to adjust to the level of the power flux. The central deposition case has a power distribution similar to the one during the ohmic heating phase. As a consequence, the OH and NI phases have rather flat τ_E-profiles. In the off-axis case, the central τ_E values of the OH and NI phases approach each other. Indeed, the rise of the central electron energy density after a sawtooth drop is about the same in the OH and off-axis NI phases, indicating the same central power density (confirming the deposition calculation) and therefore giving rise to similar transport. In the radial zone where the power density deposited off-axis sharply rises, τ_E decreases correspondingly. It has been shown in Ref. /17/ that the assumption of a local heat conductivity coefficient, however, is also able to describe the central and off-axis deposition cases.

As a final example we mention the good confinement observed in slide-away discharges /11/. At low density, when the plasma current is carried by slide-away electrons, less ohmic heating power is required to maintain the plasma current (see Fig. 5). Possibly as a consequence of the reduced power flux, the confinement seems to improve. Other examples are current drive by lower hybrid heating /18/: In a narrow density window current drive by lower hybrid waves is possible with high efficiency such that a high cur-

rent can be maintained with less than the corresponding ohmic heating power. In such a case there are indications of improved global confinement. It should be mentioned that the presence of non-Maxwellian electron distributions adds a further complication to the not understood tokamak transport. Other mechanisms specific to the fast electrons may affect confinement in such cases /19/.

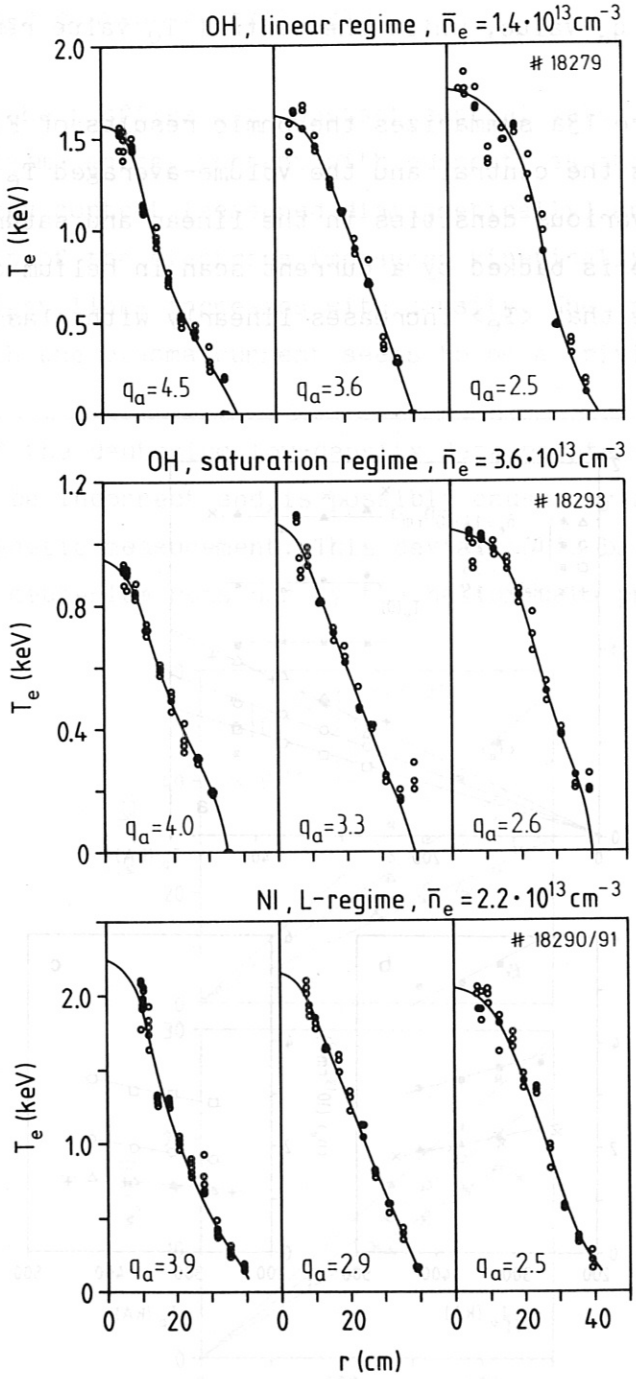

Fig. 12 T_e-profiles as measured by Thomson scattering for various q_a-values and confinement regimes.

3.2. Plasma current

The choice of the plasma current has a striking effect on the plasma profiles. Figure 12 compares T_e profiles measured by multiple Thomson scattering in the OH linear and saturation regimes and in the L-mode at a NI beam power of 1.6 MW in a case where the residual ohmic power input can be neglected (<20 % of P_{NI}). Irrespectively of the confinement regime and the heating method (ohmic or non-ohmic), the T_e profile broadens with rising current or dropping q_a value, while the central T_e value remains largely unchanged.

Ohmic heating: Figure 13a summarizes the ohmic results of Fig. 12 in a diagramm which plots the central and the volume-averaged T_e values versus plasma current for various densities in the linear and saturated regimes. The low-density case is backed by a current scan in helium discharges. It is important to note that $\langle T_e \rangle$ increases linearly with plasma current.

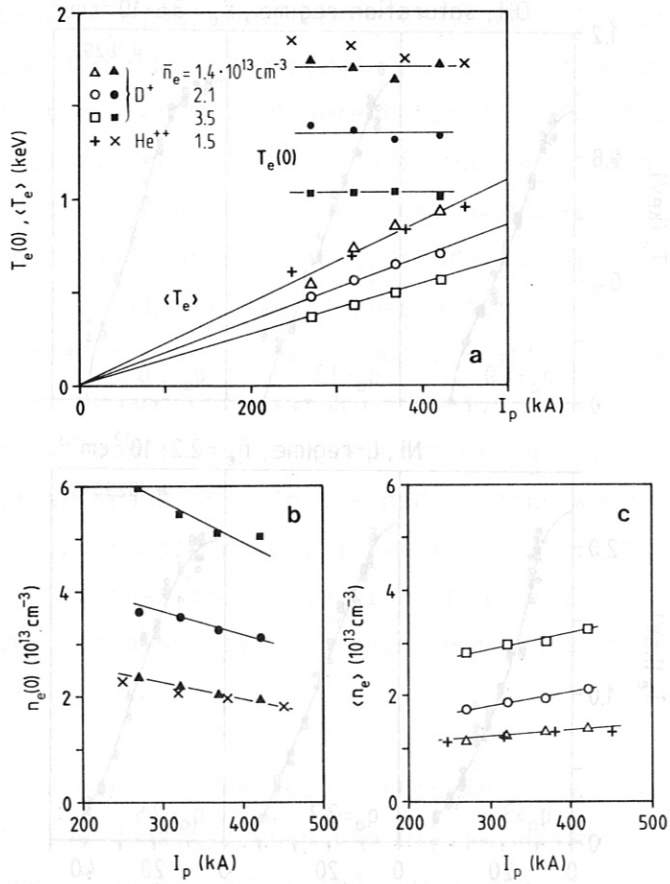

Fig. 13 Central and volume averaged electron temperature (a) and density (b,c) versus plasma current for various densities. The low density deuterium scan is backed by He-data.

Figure 13b and c show the same values for the density ; like the temperature, the volume-averaged density increases with current, but not linearly, since the central density decreases in a current scan where the line-averaged density was kept constant by a feedback system.
No systematic study of ion temperature profiles has yet been done; the few existing ohmic T_i profiles (measured by passive charge exchange /20/) reflect the same behaviour as the T_e profiles, viz. broadening at higher current and a rather content central value.

The broadening of the profiles (at constant central values) causes a linear increase of the plasma energy content with current, as shown in Fig. 14a for the total energy content (measured diamagnetically) and in Fig. 14b for the energy constant of the electrons (measured kinetically).* The actual slope of the straight lines increases with density. The increase of the energy content with the plasma current seems to be a trivial consequence of

---

* The deviation of the deuterium low-density data points at low current in Fig. 14a seems to be incorrect and is possibly caused by a not fully compensated diamagnetic measurement. This deviation is backed neither by other low-density deuterium runs nor by the helium data presented.

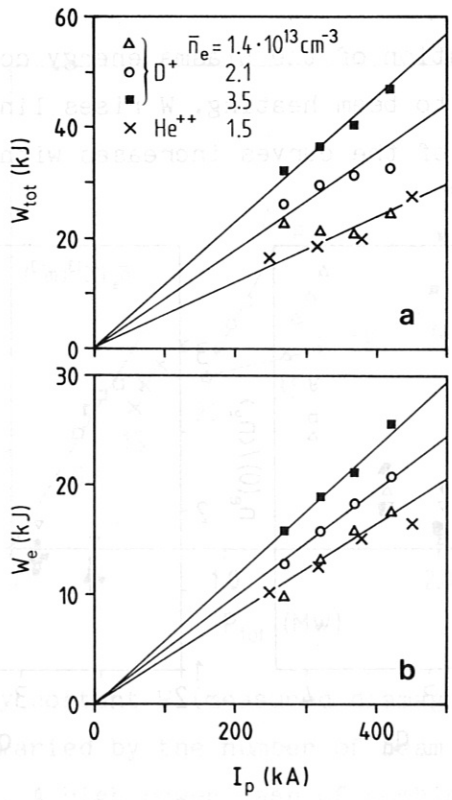

Fig. 14 Total (a) and electron (b) energy content versus plasma current for various density values.

slope of the straight lines increases with density. The increase of the energy content with the plasma current seems to be a trivial consequence of the simultaneous increase of ohmic heating power. It should be borne in mind, however, that the increase in energy content occurs via a broadening of the profiles at constant central values, as documented above, and not by an overall increase of parameters.

Auxiliary heating: In the next section we discuss the role of plasma current in determining the energy content with beam heating in the L-mode. The effect of current on profiles is the same as under ohmic heating conditions (see Fig. 12c). Figure 15 summarizes the effect of I_p (expressed as the safety factor q_a) on the T_e and n_e profile shape parameters at various heating power levels and compares them with the OH results. There is no basic difference. It is a remarkable (of course already well-known fact /6/) that the effect of current on profile shapes is the same, irrespectively of whether the heating method is ohmic /21/ or non-ohmic. In the case of the n_e profiles the effect of the spatially different source distribution with beam heating is overcome by the effect of I_p on the density profile; only at very low density does the effect of central beam fuelling give rise to peaking of n_e.

Figure 16 plots the variation of the plasma energy content versus current on transition from ohmic to beam heating. W rises linearly with current in both cases and the slope of the curves increases with heating power (less

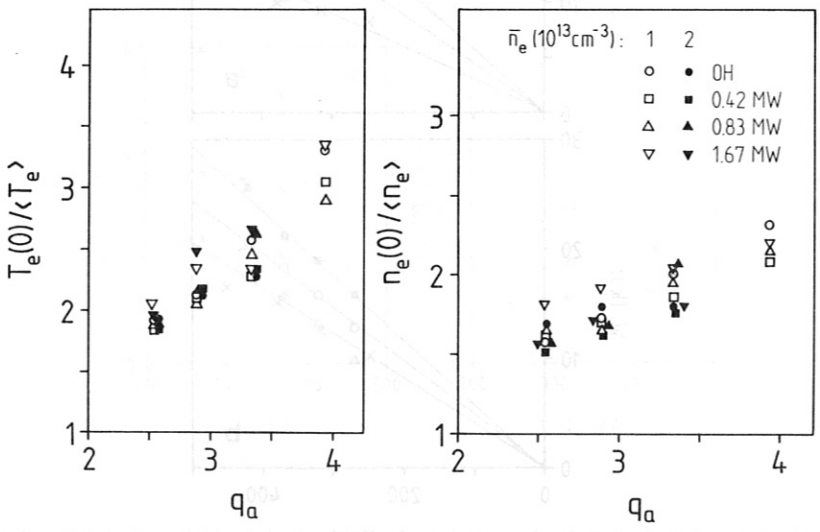

Fig. 15 Electron temperature and density profile parameters versus q_a for different densities and heating power levels.

than linear because of the degradation in confinement with power). Again this similarity in behaviour is striking because in the ohmic case the linear rise in energy content is caused by the heating of the plasma, while with auxiliary heating it is due to the improvement of the energy confinement time with current. But both with ohmic and non-ohmic heating, the increase in energy content with current occurs via profile broadening.

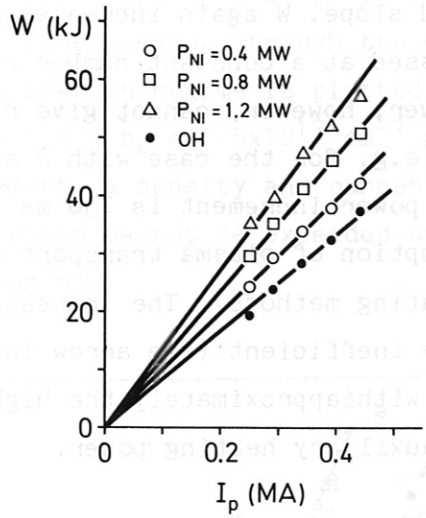

Fig. 16 Total energy content (measured diamagnetically) versus plasma current at the transition from ohmic to beam heating.

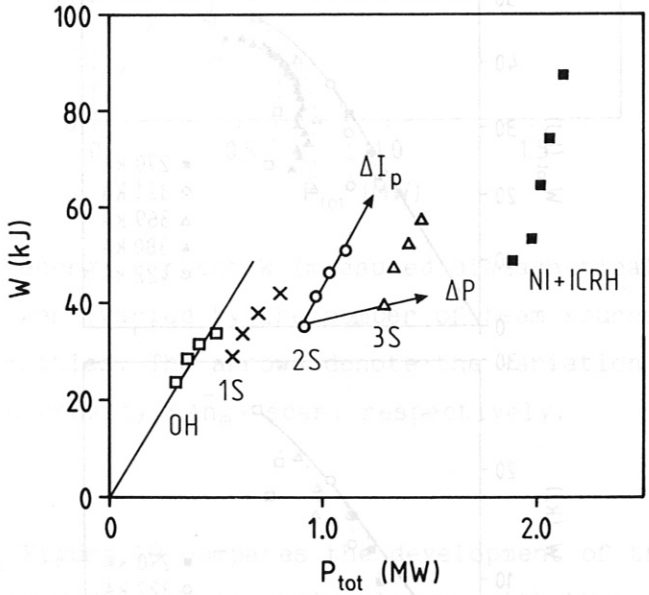

Fig. 17 The total energy content W (measured diamagnetically) versus total heating power (varied by the number of beam sources) for various plasma currents. A high power case of combined NI and ICRF heating is also shown. The arrows denote the variation of W in a power (ΔP or a current (ΔI_p) scan, respectively.

Figure 17 plots the total energy content of the plasma at various currents starting from the OH target plasma, with neutral injection in the transitional power range, and with ICRH at high power. The ohmic data points are shown as open symbols. They denote the "good" ohmic confinement in the sense of a steep rise of W with heating power along a line which passes through the origin. Already at low auxiliary heating power W increases along a curve with reduced slope. W again increases along a steep curve when the current is increased at a constant number of heating sources. The residual ohmic heating power, however, cannot give rise to the large increase in energy content (e.g. for the case with 2 sources) unless the confinement time for this power increment is 230 ms (an unlikely value and an unlikely physical assumption of plasma transport discriminating between the power of different heating methods). The increase of energy content via heating seems to be highly inefficient (see arrow in Fig. 17), while it can be increased with current with approximately the high efficiency of the ohmic phase even at high auxiliary heating power.

3.3. Plasma density

The T_e profile is rather independent of density with ohmic heating in the linear or saturation regime or with beam heating (see Fig. 12).

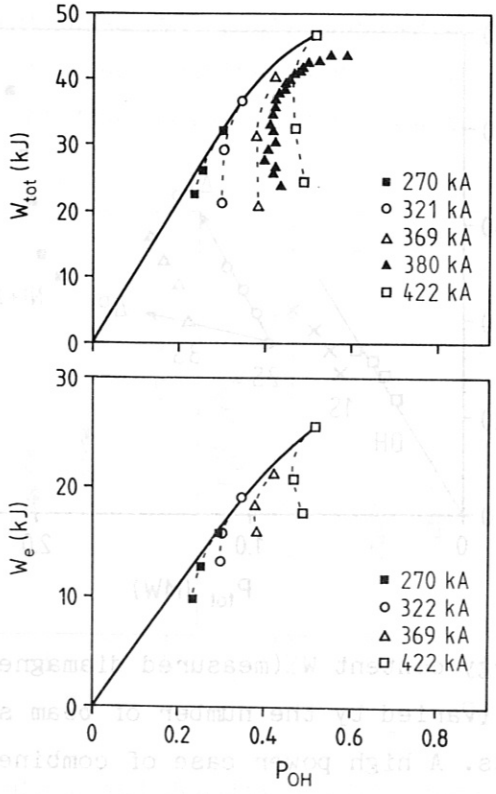

Fig. 18 The total and the electron energy content versus heating power in density scans for various plasma currents.

Ohmic heating: In the ohmic phase the density is a simple means of increasing the energy content. Figure 18 plots the variation of the total and the electron energy content, W_{tot} and W_e, as function of the ohmic heating power, which was varied in density scans ($\bar{n}_e$=1.5, 2.1, 3.5x10^{13} cm^{-3}) for different current values. In the linear regime the energy increases at nearly constant heating power (because of the compensation of T_e and Z_{eff} variation); in the saturation regime the slope is reduced and W follows a heating curve (a straight line passing through the origin). The transition from the linear to the saturation regime is plotted in detail by another density scan in the range $1.5 < \bar{n}_e < 6.5\text{x}10^{13}$ cm^{-3} at 380 kA. Because of the saturation in confinement, a density and current scan, like the one of Fig 18, maps out a curve which cannot be exceeded under ohmic conditions with gas-puffing (solid curve).

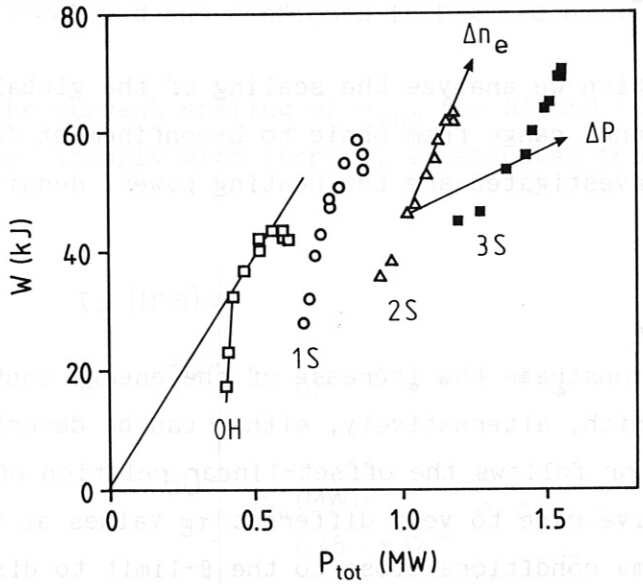

Fig. 19 The total energy content W (measured diamagnetically) versus total heating power (varied by the number of beam sources) for various plasma densities. The arrows denote the variation of W in a power (ΔP) and a density ($\Delta\bar{n}_e$) scan, respectively.

Auxiliary heating: Figure 19 compares the development of the energy content with the line-averaged density in ohmic plasmas with that with auxiliary heating at various heating power levels for H^0 injection into D^+ plasmas ($1.5 < \bar{n}_e < 7.2\text{x}10^{13}$ cm^{-3}). The variation of the density with beam heating has the same effect on the energy content as the variation of the current shown in Fig. 17. Auxiliary heating is again found to be rather insuffi-

cient for increasing the energy content (see arrows in Fig.19). Unlike the current scan, the power-increase is only partly additional ohmic power at higher density. The major part is increased beam power because of improved beam deposition at higher density. As in the current scan, it cannot be argued that the steep rises in the energy content with density in the auxiliary heating phases are due to improved confinement of the additionally supplied power. The steep increase of W under beam heating conditions indicates that there remains a fraction of the total energy content which can be increased with density, irrespectively of the heating method and the level of heating power. The rise of W with density with auxiliary heating is comparable to that under ohmic conditions.

4. Scaling of the global confinement time in the transitional power range

In the following section we analyze the scaling of the global confinement time in the transitional range from ohmic to L-confinement /22/. The scaling parameters investigated are the heating power, density, current and isotope mass /23/.

4.1. Power dependence

Figures 17 and 19 demonstrate the increase of the energy content with auxiliary heating, which, alternatively, either can be described by a power law $W \propto P^{-\alpha}$ ($\alpha \sim 0.5$) or follows the offset-linear relation of equ. 1. The two relations will give rise to very different τ_E values at high power and it will require plasma conditions close to the β-limit to discriminate between the two. It is not the intention of this paper to try to clarify this aspect of confinement, particularly since high-power NI yields rather a power-law dependence /7/, while the ICRH-cases /8/ or ICRH plus NI /24/ are better described by a linear-offset relation, even at high power. There might be additional effects not related to confinement but to heating efficiency which could give rise to a power-law dependence in the NI case, e.g. those linked to plasma rotation /25/. The power-law dependence is also observed in isotopically clean situations as with D^0 injection into D^+ plasmas so that the gradual transition of a basically deuterium plasma to a hydrogen one at high beam power could only aggravate the situation with H^0 injection into D^+ plasmas, but it is not the general explanation of the different scalings of τ_E with NI or ICRF heating.

In the following we analyze the data according to the offset-linear relation $W = W_{OH} + \tau_{inc} \Delta P$ with W being the total energy content, W_{OH} that

of the ohmic target plasma, $\Delta P = P_{tot} - P_{OH}$ the difference between total and ohmic heating power, and τ_{inc} the so-called incremental confinement time. According to Figs. 7, 17, and 19 this relation describes well the transition from the OH to the L-regime in ASDEX and it is a form which satisfies the results of other experiments, too.

4.2. Current dependence

The effect of current on the energy content of an ohmic and an NI-heated plasma is plotted in Fig. 17. The energy content rises with current in the ohmic case along with the heating power, giving rise to a current and power-independent confinement time; in the auxiliary heating case the energy content rises with current at constant heating power, causing the known current dependence of τ_E. Figure 20 plots τ_E versus I_p on transition from ohmic to beam heating ($H^0 \rightarrow D^+$); at high power the linear τ_E to I_p scaling is fully developed and confirmed in Fig. 20 by NI and ICRF heating results.

Figure 21 shows the current scaling of τ_{inc} for NI and ICRH; also this quantity increases linearly with current, as expected from the effect of

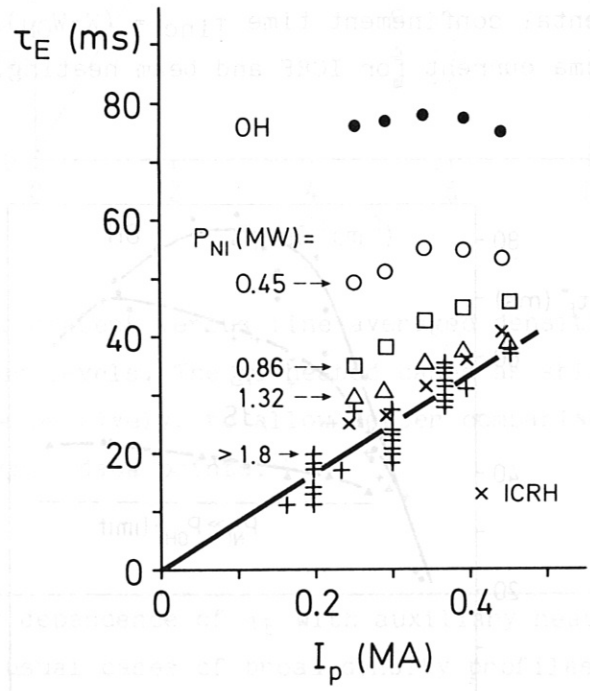

Fig. 20 Global energy confinement time versus plasma current at the transition from ohmic to beam heating. At high heating power, the results of ICRF heating are also shown (x). For the NI cases: $\bar{n}_e = 3.3 \times 10^{13}$ cm^{-3}.

current on T_e and n_e profiles under beam heating conditions. The current dependence of τ_{inc} implies of course that a current scan at high auxiliary heating power changes W more than at low or ohmic power. The simultaneous linear current scaling of τ_E and τ_{inc} is possible in the limit of $P_{tot} >> P_{oh}$.

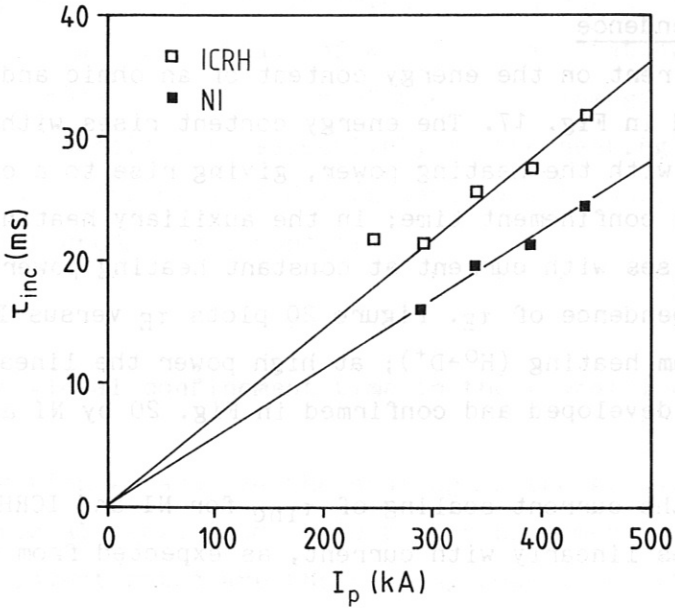

Fig. 21 The incremental confinement time $\tau_{inc} = (W-W_{OH})/(P_{tot}-P_{OH})$ versus plasma current for ICRF and beam heating.

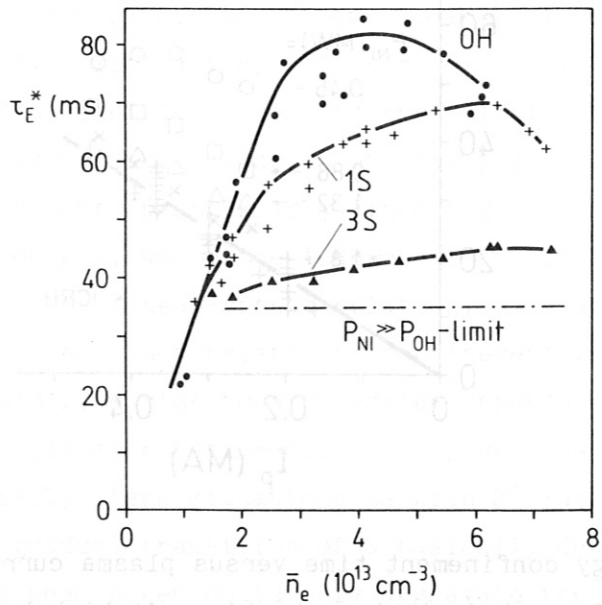

Fig. 22 Density scaling of the global energy confinement time of deuterium discharges. S = number of NI-sources; I_p = 0.4 MA, B_T = 2.2 T, q_a = 2.6; $\bar{n}_e = 3.3 \times 10^{13}$ cm^{-3}.

4.3. Density dependence

Figure 22 plots the density dependence of the global energy confinement time τ_E versus the line-averaged density on transition from ohmic to beam heating ($H^0 \rightarrow D^+$). The ohmic curve displays the linear and the saturation regime; at high density close to the density limit τ_E decreases. With auxiliary heating the density dependence of τ_E is reduced and gradually lost towards high power.*

The increase in plasma energy due to NI is largely independent of the density for the linear (as was already observed in JFT-2M /3/) and the saturation regime as shown in Fig. 23. In order to demonstrate the

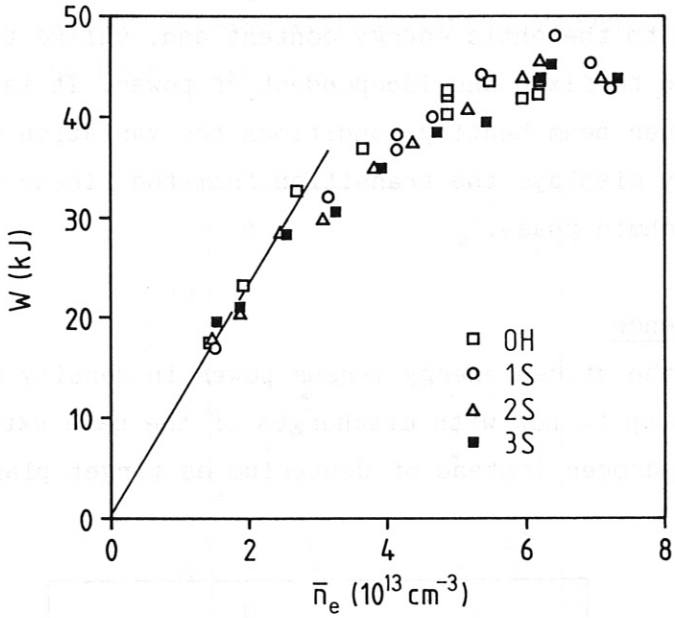

Fig. 23 Total energy content versus line averaged densities for various heating power levels. The NI heated cases as shifted by 11, 18.5 or 26 kJ, respectively, to allow better comparison with the unshifted ohmic data points.

---

* The lack of density dependence of τ_E with auxiliary heating and τ_{inc} may be restricted to the usual cases of broad density profiles; there is another class of discharges where the density profile is peaked and generally the sawteeth are lost or are ineffective (see Fig. 8). The most remarkable representatives are pellet-refuelled discharges and counter NI; one has to await further studies to determine whether both τ_E^L and τ_{inc} are still density-independent under such profile conditions.

identical variation of the total energy content with the density at all power levels, the results obtained with beam heating were shifted along the W-axis onto the unshifted ohmic curve. The curve with 1, 2, 3 sources were shifted by 11, 18.5, and 26 kJ, respectively. Figure 23 shows τ_{inc} to be independent of the density, which is also observed with ICRF heating. The remaining density dependence of the global confinement time seems to be caused by the density dependence of a residual ohmic contribution to the total energy content, as indicated by Fig. 23. At high heating power, when the ohmic power contribution is negligible the meaning of an ohmic energy content is questionable. Nevertheless, Fig. 19 documents that also under beam heating conditions when $P_{oh} << P_{tot}$ the energy content of the discharge can be raised by increasing the density. The maximal increase roughly corresponds to the ohmic energy content and, unlike the effect of current, it seems to be fixed and independent of power. It is interesting to see that even under beam heating conditions the variation of the energy content with density displays the transition from the linear to the saturation regime of the ohmic phase.

4.4. Isotope dependence

Figure 24 compares the stored energy versus power in density scans for the $H^0 \rightarrow D^+$ cases studied up to now with discharges of the same external settings but with hydrogen instead of deuterium as target plasma. The

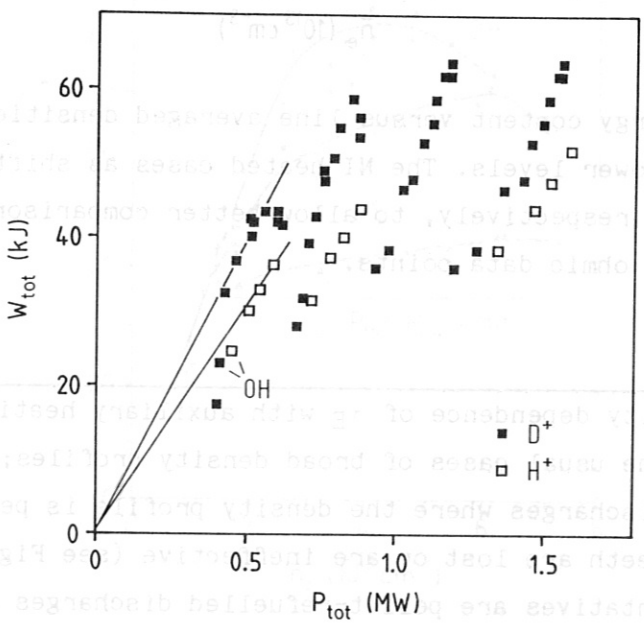

Fig. 24 Total energy versus heating power in density scans of deuterium ($H^0 \rightarrow D^+$) and hydrogen ($H^0 \rightarrow H^+$) target plasmas.

isotope dependence of the ohmic confinement (see Fig. 1) continues into the beam heating phase with deuterium being superior to hydrogen (even when hydrogen is injected). The same scaling study as presented above yields τ_{inc}=20 ms for hydrogen.

4.5. Confinement scaling in the low-power L-regime

With the above results the transition in confinement from ohmic to auxiliary heating can be described on the basis of relation 1. τ_{inc} is a function of I_p only ($\tau_{inc}(s) = 0.061 \times I_p(MA)$); the density dependence of τ_E is caused by the n_e dependence of a residual ohmic energy fraction $W_{OH'} = \tau_E^{OH'} \cdot P_{OH'}$; $W_{OH'}$ lies on the linear-offset W versus P_{tot} relation at the reduced ohmic power input $P_{OH'}$; $\tau_E^{OH'}$ is the global energy confinement time of a fictitious ohmic plasma with unchanged current I_p but with a heating power reduced from P_{OH} to $P_{OH'}$.

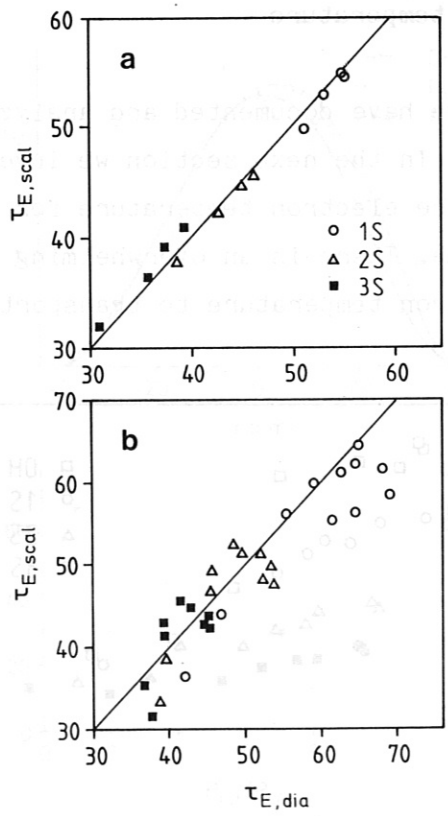

Fig. 25 Comparison of the scaled to the measured energy confinement time for current (a) and density (b) scans at various heating power levels (1 source ≈ 0.45 MW).

$$\tau_E^{scal} = W/P_{tot} = \{W_{OH} - (P_{OH} - P_{OH'}) \times \tau_{inc} + (P_{tot} - P_{OH'}) \times \tau_{inc}\}/P_{tot},$$

$$\tau_E^{scal} = \tau_E^{OH}(\bar{n}_e) \times P_{OH}/P_{tot} + \tau_{inc}(I_p) \times (1 - P_{OH}/P_{tot})$$

Figure 25 compares the measured τ_E with the scaled one τ_E^{scal} for (a) current scans and (b) density scans of NI-heated plasmas in the transitional power range. τ_{inc} is determined by minimizing the quadratic deviation from the τ_E data of the current scan. The current scaling gives τ_{inc}=25.5 ms for the density scan data of Fig. 25(b) (I_p=0.42 MA). There is satisfactory agreement between the measured data and the scaled ones on the basis of a current-dependent incremental confinement time and of a density dependence introduced through just the ohmic confinement time which, however, maintains its linear or saturated characteristics.

5. The role of electron temperature

In the previous sections we have documented and analyzed the effect of the power flux on confinement. In the next section we investigate in more detail the importance of the electron temperature for the degradation of confinement in the L-regime. There is an overwhelming amount of theoretical work which links the electron temperature to transport and confinement via

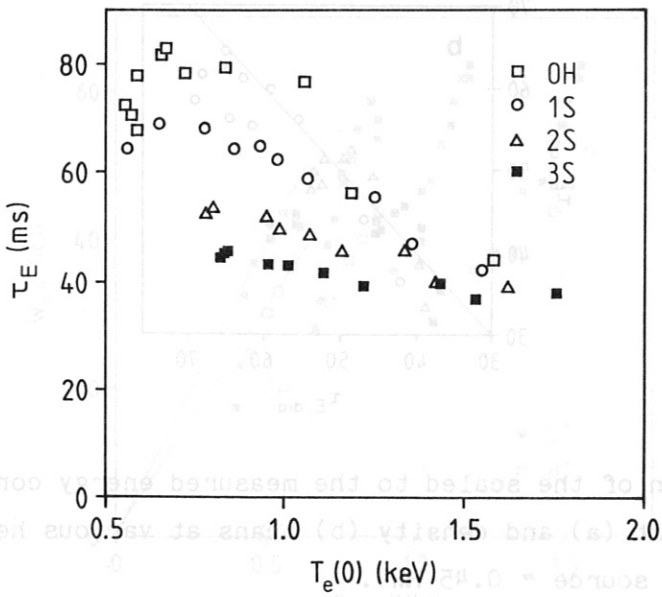

Fig. 26 The global energy confinement time plotted versus the central electron temperature in density scans at various beam power I_p = 0.42 MA.

electron collisionality, electrical resistivity or electron temperature gradient. As the degradation of confinement is - according to transport analysis - predominantly caused by the increase of the electron heat diffusivity χ_e, our main interest is to explore whether χ_e is a sensitive function of T_e or its gradient or whether χ_e directly increases when the necessity arises to transport a higher heat flux (because the T_e gradient is restricted by a separate condition /21, 26, 27/).
The electron temperature can be varied in a wide range depending on density, impurities, toroidal field, and heating power. In Fig. 26 the global confinement time is plotted versus the central electron temperature for density scans under ohmic and beam heating conditions with different power levels. The density is scanned from 1.5 - 7.5x10^{13} cm^{-3}. Under ohmic conditions, basically the same T_e range is accessible as with beam heating after slight adjustments of the density. There is no unique dependence between the global confinement time and central electron temperature.

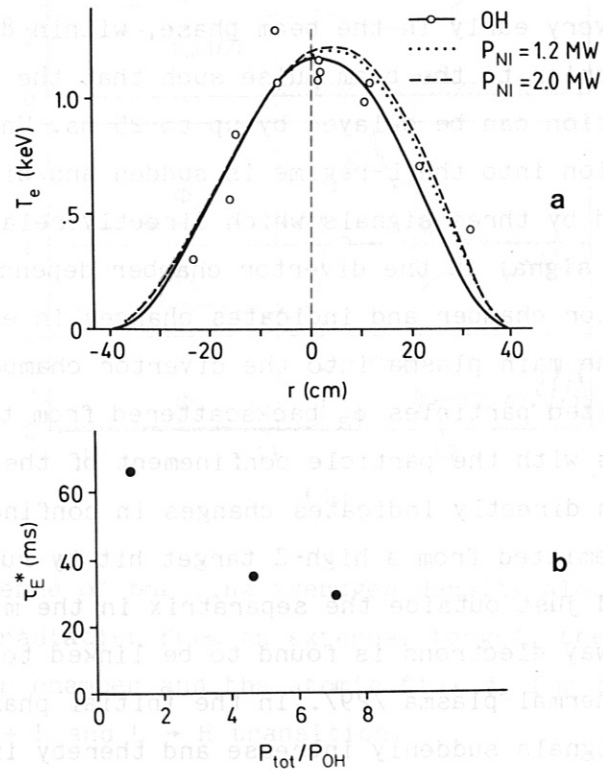

Fig. 27 Variation of the energy confinement time τ_E^* (measured diamagnetically) with normalized heating power (b). The electron temperature profile (a) is kept constant for the three cases (individual data points are shown for the ohmic case) by increasing the density with power (OH: $\bar{n}_e$ = 2.1x10^{13} cm^{-3}, 1.2 MW: $\bar{n}_e$ = 3.4x10^{13} cm^{-3}, 2.0 MW: $\bar{n}_e$ = 4.2x10^{13} cm^{-3}).

In order to study the role of the electron temperature and the T_e profile in more detail, in a sequence of special discharges T_e was kept constant in a neutral injection (NI) power scan. In order to keep T_e invariant, the heating by the beams was offset by increasing the plasma density by matched gas-puffing from the outside. Figure 27a shows the three T_e profiles for the cases $P_{NI} = 0$, $\bar{n}_e = 2.1 \times 10^{13}$ cm^{-3}, $P_{NI} = 1.2$ MW, $\bar{n}_e = 3.4 \times 10^{13}$ cm^{-3}, and $P_{NI} = 2.0$ MW and $\bar{n}_e = 4.2 \times 10^{13}$ cm^{-3}; Fig. 27b plots the three τ_E values versus the beam power. No difference is noted in the power scaling of τ_E between the scan as described above and a scan at constant density (where T_e rises with beam power). Also the accompanying phenomena of degraded confinement, such as the increased loss of plasma particles and runaway electrons, are the same.

Another experimental possibility to investigate the reasons for confinement degradation is the study of the transition in confinement from ohmic to auxiliary heating in the initial heating phase. The following results are obtained with beam heating. Under normal conditions the degradation in confinement occurs very early in the beam phase, within 8-10 ms. With strong gas-puffing prior to the beam pulse such that the ohmic density increases, the transition can be delayed by up to 25 ms. Under such circumstances the transition into the L-regime is sudden and distinct. The L-transition is marked by three signals which directly relate to changes in confinement: The H_α signal in the divertor chamber depends on the power flux into the divertor chamber and indicates changes in energy confinement. The ion flux from the main plasma into the divertor chamber is measured via the flux of neutralized particles ϕ_a backscattered from the target plates; this flux correlates with the particle confinement of the main plasma /28/. Another signal which directly indicates changes in confinement is the hard X-ray radiation ϕ_X emitted from a high-Z target hit by runaway electrons; the target is placed just outside the separatrix in the mid-plane. The confinement of runaway electrons is found to be linked to the confinement properties of the thermal plasma /29/. In the initial phase of the beam pulse these three signals suddenly increase and thereby indicate the OH-L transition. If the conditions are such that there is an H-transition later in the beam pulse the transition is again indicated by these three confinement monitors since they now suddenly decrease.

Figure 28 shows as an example the transition first into the L-phase and then into the H-phase. The three direct confinement signals (ϕ_X, D_α and ϕ_a) are plotted together with the line averaged density along different chords

show the decrease in particle confinement). Later in the beam pulse an H-transition occurs which reverses the signal changes.

Figure 29a shows the line averaged density along the chords and the parallel charge exchange flux at high energy close to the injection energy to mark the beginning of NI. The density starts to rise when the external gas flux ϕ_G is applied. Figure 29b plots the development of the electron temperature profile starting from the ohmic one, in the beam phase prior to and after the L-transition. The points of time of the different profiles of Fig. 29b are indicated in Fig. 29a. The first heating response occurs in the plasma centre; the L-transition happens when the plasma edge starts to be heated. It is not clear whether the T_e-broadening is the cause of the confinement degradation.

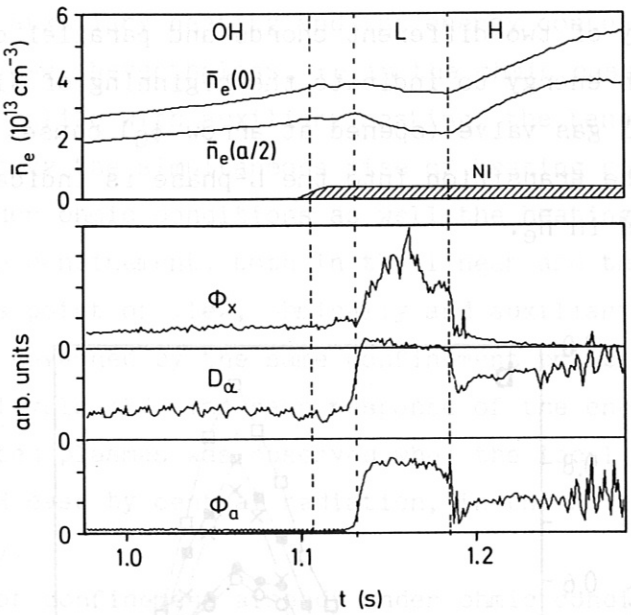

Fig. 28 Time dependence of the line averaged density along two chords, the hard X-ray radiation from an external target, the H_α-radiation in the divertor chamber and the atomic flux ϕ_a for the target plate for the OH → L and L → H transition.

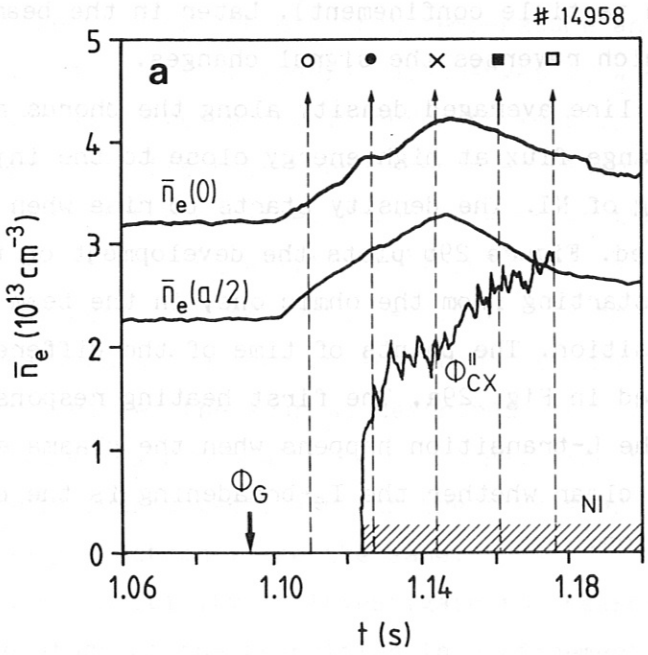

Fig. 29a Line density of two different chords and parallel charge exchange flux at high energy to indicate the beginning of NI.
The external gas valve (opened at arrow ϕ_G) causes $\bar{n}_e$ to increase. The transition into the L-phase is indicated by the sudden drops in $\bar{n}_e$.

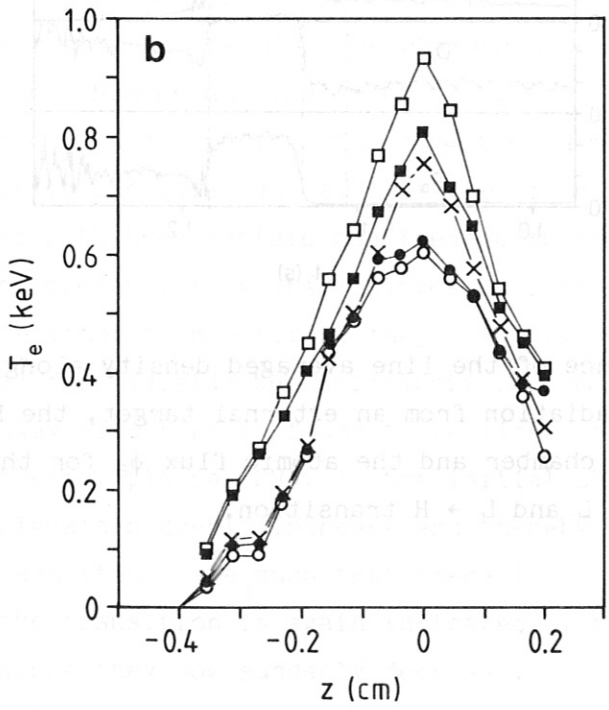

Fig. 29b The development of the T_e profile in the initial NI heating phase at the transition from ohmic to beam heating. The time points of the different profiles are shown in Fig 28a.

6. Discussion

Auxiliary heating power, plasma current, and density are external parameters which independently affect confinement. In the case of ohmic heating the heating power is not an externally controllable parameter and variation of density or current changes the power input. The direct effect of current and density on confinement can therefore be modified in the ohmic case owing to the additional relations between power and current or density. The effect of current on confinement is most clearly shown with auxiliary heating. The increase of current broadens the T_e and n_e profiles and increases in a linear relation the energy content at constant heating power. This effect on profiles ultimately gives rise to the linear scaling of the global energy confinement time τ_E with plasma current.

In the ohmic phase the same effect of current on the plasma profiles is observed as with auxiliary heating and the energy content rises with current in the same way. Nevertheless, τ_E in the ohmic case is independent of current because, unlike with auxiliary heating, the beneficial effect of current is offset by the simultaneous rise of heating power. We have to conclude that under ohmic conditions as well the heating power has a degrading effect on confinement, both in the linear and the saturation regime. From this point of view, ohmically and auxiliary-heated plasmas in the L-regime are governed by the same confinement principles only at different power levels /1/. The same response of the energy transport in ohmic and NI-heated plasmas was observed when the local power density was varied (in the OH case by central radiation, in the NI case by off-axis power deposition).

The degradation of confinement already under ohmic conditions points to a fundamental role of the power flux in confinement and indicates the existence of a basic non-linear relation between the energy content and heating power.

The role of current and heating power in confinement can be independently studied only with auxiliary heating when the ohmic degeneration - the rough proportionality between current and heating power - is removed. It is obvious from the above discussion that the current scaling of the confinement time is the fundamental one which should apply to all heating methods as soon as the ohmic power input becomes negligible. The current scaling reflects the role of the magnetic configuration in confinement, which enters through profile widths at constant central values. Current scaling is therefore not a new confinement feature of auxiliary-heated plasmas,

rather it is the disappearance of a common element, viz. the dominance of the ohmic heating power and its proportionality to the plasma current. A consequence of these considerations is that τ_E is proportional to the current in the H-mode too /7/, despite the distinct differences to the L-mode in the development of the two phases and in the absolute values of τ_E. Also in the H-mode, the ohmic heating power is $P_{oh} << P_{NI}$.

From this analysis it is obvious that there has to be a discontinuity in the slopes of a W versus P diagram on transition from ohmic to auxiliary heating as shown in Figs. 7, 17, and 19. The discontinuity arises when one views the OH data lying on a linear relation, as in an ohmic power scan (varied via current) where the actual degradation of confinement is masked. The degradation in confinement becomes obvious as soon as auxiliary heating sets in.

The observation of a discontinuity as discussed above has occasionally been interpreted in terms of a special quality of ohmic heating in comparison with auxiliary heating (the link between the current density and heating power profile might lead to self-optimization of the system, resulting in good confinement properties). The actual reason for the discontinuity seems to be the change in "operational direction" on transition from ohmic to auxiliary heating as indicated in the W-P-I_p diagram of Fig. 30, which shows schematically the non-linear dependence of W on P and the effect of current. An ohmic power scan occurs in a plane where P/I_p is constant; with auxiliary heating, however, a power scan is continued in an I_p=const. plane In order to stay on the "good" ohmic curve, the current has to be increased along with the auxiliary heating power, which is, however, eventually prevented by MHD-stability criteria. The ohmic W vs. P trace (dashed line in Fig. 30) is therefore not a relation which can be scaled to arbitrary power. The plasma state with better than ohmic confinement is at lower power than the ohmic power and is not accessible with ohmic heating of a thermal plasma. One can speculate that in this power range most of the non-linearity of the W vs. P relation may occur so that at the auxiliary heating power levels the offset-linear relation $W = b+aP$ is a good description.

In the ohmic linear regime a $\tau_E \propto q_a^{\alpha}$ scaling with $0.5 < \alpha < 0.8$ is observed in some cases which implies that confinement <u>improves</u> when the plasma current is <u>decreased</u>. But also in the linear regime the plasma profiles broaden with current and there has to be another mechanism which offsets and even reverses this trend. As the ohmic heating power increases

with plasma current in the linear regime, too, the effect of profile broadening is compensated by power as at higher densities. Because of this balance other variables such as Z_{eff} or P_{ei}, the power transfered collisionally from electrons to ions may play a role. Z_{eff} can vary with different wall conditions and from machine to machine. It may be Z_{eff} which ultimately gives rise to the q_a-dependence of τ_E in the linear regime and the uncontrolled variability of this parameter may be the reason for the lack of unanimous agreement about the general nature of this scaling. A stronger than linear rise of P_{oh} with current may occur at lower density because of intensified plasma-wall interaction, resulting in reduction of confinement and introduction of a q_a-dependence /13/. The existence of a reversed I_p scaling may be seen as indirect confirmation that power has to degrade confinement already under ohmic conditions. Without the balance of P_{OH} and I_p it is difficult to see how the profile effect is offset and even reversed.

At present we are not able to substitute a plasma parameter for the power flux as the quantity which determines the heat conductivity and causes confinement degradation. Neither T_e nor its gradient or dependent parameters such as collisionality seem to be responsible for the additional confinement degradation with auxiliary heating. Further experiments not

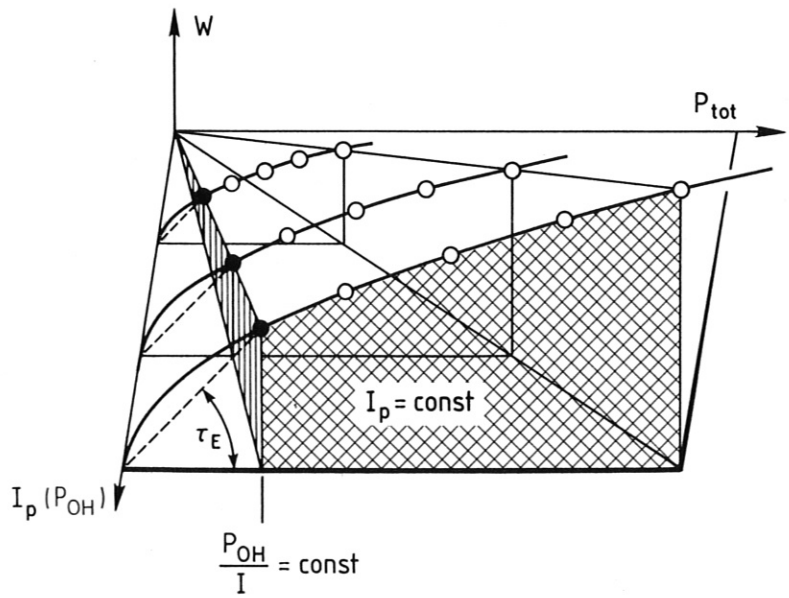

Fig. 30 3-dim. plot which shows schematically the expected non-linear relation between W and P at constant I_p and the different paths of ohmic and auxiliary heating power scans.

discussed here in detail indicate that also plasma pressure is not the crucial element. A comparison of β_p of ohmic discharges with gas-puff or pellet refuelling or of L- and H-mode plasmas indiate that the discharge with higher β_p has the better confinement. As an experimental example may there be the study of the OH→L transition. The degradation occurs when the plasma pressure has hardly risen but the power flux is already increased. On the one hand, we observe (as others do) that the T_e profile is rather resilient to changes of shape unless the plasma current is varied. On the other hand, the absolute value of T_e and its gradient can easily be changed even under ohmic conditions in a wide range without the disadvantage of confinement degradation, while the effort to increase T_e via additional heating power leads to immediate degradation. We have to conclude that the power flux and poloidal field largely determine confinement.

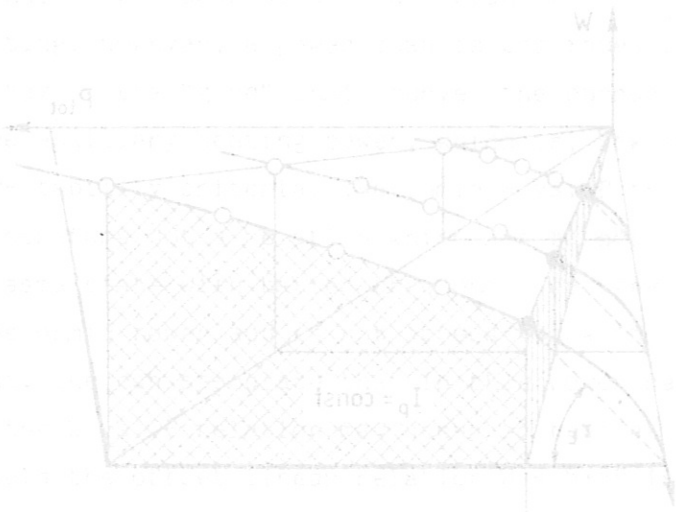

Acknowledgement

The authors would like to thank their colleagues of the ASDEX team for contributing experimental results and valuable ideas to the discussions of confinement aspects; in particular, they are indebted to P. Diamond, W. Tang and H. Furth for their specific comments and ideas on this paper. They would also like to thank H. Volkenandt and C. Weller for preparing the manuscript.

References

/1/ H. Niedermeyer, F. Wagner, G. Becker, K. Büchl, A. Eberhagen et al., Proceedings of the 11th Int. Conf. on Plasma Phys. and Contr. Nucl. Fusion Research, Kyoto, 1986 (IAEA, Vienna, 1987), Vol. 1, p. 125.

/2/ J.G. Cordey, D.V. Bartlett, V. Bhatnagar, R.J. Bickerton, M. Bures et al., as Ref. /1/, Vol. 1, p. 99.

/3/ H. Odajima, H. Hoshino, S. Kasai, T. Kawakami, H. Kawashima et al., Phys. Rev. Letters 57 (1986) 2814.

/4/ P.E. Vandenplas, H.L. Bay, G. Bertschinger, W. Bieger, P. Bogen et al., as Ref. /1/, Vol. 1, p. 485.

/5/ J. Hugill, Nucl. Fusion, 23 (1983) 331.

/6/ R.J. Goldston, Plasma Phys. Controlled Fusion 26 (1984) 87.

/7/ A. Stäbler, F. Wagner, G. Becker, K. Bernhardi, U. Ditte et al. 4th Intern. Symp. on Heating in Tor. Plasmas, Rome (1984), Vol. I, p. 3.

/8/ K. Steinmetz, M. Brambilla, A. Eberhagen, F. Wagner, F. Wesner et al., Proc. 14th Europ. Conf. Contr. Fusion and Plasma Phys., Madrid (1987), Vol. III, p. 946.

/9/ M. Kaufmann, K. Büchl, G. Fussmann, O. Gehre, K. Grassie et al., Nucl. Fusion, to be published

/10/ F. Wagner, G. Becker, K. Behringer, D. Campbell, A. Eberhagen et al., Phys. Rev. Letters, 49 (1982) 1408.

/11/ G. Fußmann, D. Campbell, A. Eberhagen, W. Engelhardt, F. Karger et al., Phys. Rev. Letters, 47 (1981) 1004.

/12/ G. Becker, D. Campbell, A. Eberhagen, O. Gehre, J. Gernhardt, et al., Nucl. Fusion 23 (1983) 1293.

/13/ S. Ejima, T.W. Petrie, A.C. Riviere et al., Nucl. Fusion 22 (1982) 1627.

/14/ W. Engelhardt, Proc. Course and Workshop on Diagnostics for Fusion Reactor Conditions, Varenna, (1982), p. 11.

/15/ W.M. Manheimer, T.A. Antonsen, Jr., Phys. Fluids 22 (1979) 957.

/16/ F. Wagner, O. Gruber, K. Lackner, H.D. Murmann, E. Speth et al., Pyhs. Rev. Lett. 56 (1986) 2187.

/17/ G. Becker, ASDEX-Team, Neutral Injection Team, submitted to Nuclear Fusion.

/18/ F. Söldner, D. Eckhartt, F. Leuterer, A. Eberhagen, A. Giuliana et al., Proc. 12th Europ. Conf. Contr. Fusion and Plasma Phys., Budapest (1985), Vol. II, p. 244.

/19/ D.C. Robinson, N.R. Ainsworth, P.R. Collins, A.N. Dellis, T. Edlington et al., as Ref. /1/, Vol. 1, p.. 575.

/20/ F. Wagner, Jour. Vac. Sci. Techn., 20 (1982) 1211.

/21/ B. Coppi, Comments Plasma Phys. Controlled Fusion 5 (1980) 261.

/22/ F. Wagner, O. Gruber, R. Bartiromo, G. Becker, H.S. Bosch et al., Proc. 12th Europ. Conf. Contr. Fusion and Plasma Phys., Budapest (1985), Vol. I, p. 335.

/23/ G. Becker, in Controlled Fusion and Plasma Heating (Proc. 13th Europ. Conf. Schliersee, 1986), Part I (1986) 224.

/24/ F. Wagner, F.X. Söldner, K. Steinmetz, G. Becker, H.S. Bosch et al., Plasma Physics and Controlled Fusion, 28 (1986) 1225.

/25/ M. Bitter et al., Plasma Physics and Controlled Fusion, to be published.

/26/ H. Furth, Plasma Physics and Controlled Fusion, 28 (1986) 1305.

/27/ P.H. Rebut, M. Brusati, M. Hugon, P.P. Lallia, as Ref. /1/, Vol. 2, p. 187.

/28/ F. Wagner, Nucl. Fusion 25 (1985) 525.

/29/ F. Wagner, G. Fußmann, G. Becker, H.S. Bosch, H. Brocken et al., as Ref. /8/, Vol. I, p. 222.

PART B: H-MODE STUDIES

TABLE OF CONTENTS

1. Introduction and overview of the H-mode

The difference in the energy confinement property is the most important aspect of an H-mode in comparison to an L-mode plasma /1, 2/. The improvement of the global energy confinement time is caused by a reduction of the electron heat diffusivity. The particle confinement also improves together with the energy confinement. The different energy and particle confinement properties of L- and H-discharges are evident from the different variation of β_p and the line-averaged density $\bar{n}_e$ during an NI pulse. Figure 1 compares L- and H-discharges of the same external parameter setting and the same heating power. Plotted are the line-averaged density $\bar{n}_e$, β_p+li/2 from the plasma equilibrium, β_p measured diamagnetically and the H_α-intensity of the H-discharge measured inside the divertor chamber. The plasma particle content is kept constant in the ohmic phase by a density feedback system; in an L-discharge the density decreases despite additional particle fuelling by the beams and intensified gas puffing from the outside. In an H-discharge the plasma particle content sharply rises without external gas feed. The improvement in energy confinement causes the energy content of the discharge to rise, as is obvious from both the equilibrium and the diamagnetic signal. The energy content of the H-mode plasma is nearly twice that of the L-discharge and - as the heating power is the same for the two cases - τ_E is nearly twice as large. H_α in the divertor chamber is determined by the local recycling due to the ionization of the neutral gas in the divertor chamber by the divertor plasma and the neutralization of the divertor plasma at the target plates. The intensity of this circular process - neutralization and re-ionization - depends on the power flux into the divertor chamber. The H_α-intensity in the divertor chamber is therefore a measure of the energy confinement of the main plasma. In particular, a change in the H_α-intensity signals a change in energy confinement properties. For example, the transition into the H-phase (dashed vertical line) is indicated by the sudden drop in H_α-intensity.

A characteristic feature of the H-discharge is that it develops from a preceding L-phase. A case where an ohmic plasma immediately develops into an H-mode as soon as the beams are initiated has never been observed. The transition from the L- to the H-phase can be seen in Fig. 1 and is shown in more detail in Fig. 2. Plotted is the time development of $\bar{n}_e$, β_p, and the atom flux ϕ_a emitted from the outer target plate, which is another recycling signal measured in the divertor chamber. It is caused by the

impinging ions which are neutralized and backreflected. As ϕ_a is measured for energies >100 eV it only represents ions from the main plasma periphery and therefore its intensity is related to the particle confinement properties of the plasma bound by the separatrix.

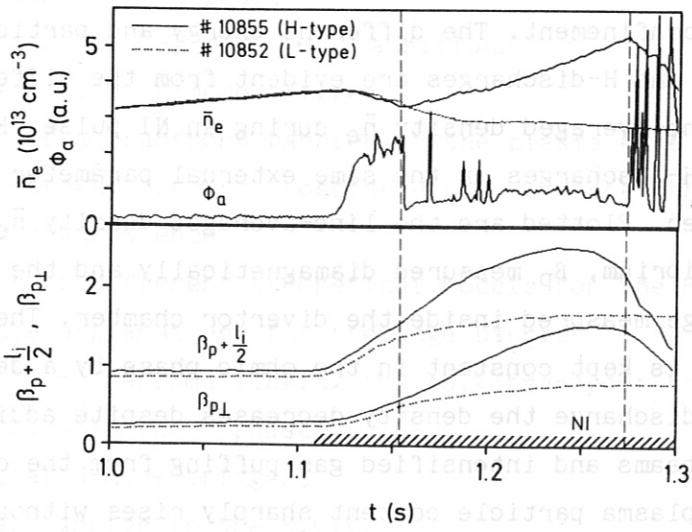

Fig. 1 Variation of the line average density $\bar{n}_e$, the atom flux ϕ_a emerging from the outer neutralizer plate at the separatrix intersection $\beta_p + l_i/2$ (from the plasma equilibrium), and $\beta_{p\perp}$ (from the diamagnetic signal) during the neutral injection pulse (hatched area). Compared are an H- (solid lines) and an L-discharge (dotted lines). The H-transition is indicated by the dashed vertical line.

The preceding L-phase in Fig. 2 is characterized by a high atom flux ϕ_a, decreasing density and a moderate increase in β_p. The H-transition is indicated in a sudden drop of ϕ_a equivalent to the sudden reduction of the H_α-intensity in Fig. 1. ϕ_a drops to a value comparable to the ohmic level. The simultaneous drop of the divertor signals (H_α or ϕ_a) and the correlated rises of the main plasma density and β_p mark the transition into the H-phase. The transition is sharp and can happen within 2 ms, indicating the existence of precise transition conditions. The transition occurs spontaneously without any operational intervention from the outside. The development of an H-discharge during the beam heating phase is determined by the setting of the plasma parameters for the preceding ohmic phase and by the level of heating power. The H-mode requires a high heating power

above a power threshold (see sect. 4). When the beam pulse is terminated, the plasma remains in the H-phase for about 35 ms (2-3 times the beam ion slowing-down time), when suddenly ϕ_a increases once more. Symmetrically to the initial beam phase, but now in a phase with hardly any power input at all, a second L-transition occurs and gives rise to a discontinuity of the slopes of $\bar{n}_e$ and β_p, which then decrease even faster. Apparently, the plasma cannot develop the H-phase from the ohmic phase nor directly return to ohmic transport properties. The plasma evolution with an H-mode during the beam pulse always occurs in the sequence OH-L-H-L-OH.
The plasma conditions which develop in the H-phase give rise to a new type of MHD instability which repetitively modulates the H_α-radiation in the divertor chamber and the atom flux ϕ_a (see Fig. 1 and 2) and causes additional particle and energy losses, thereby somewhat degrading the good

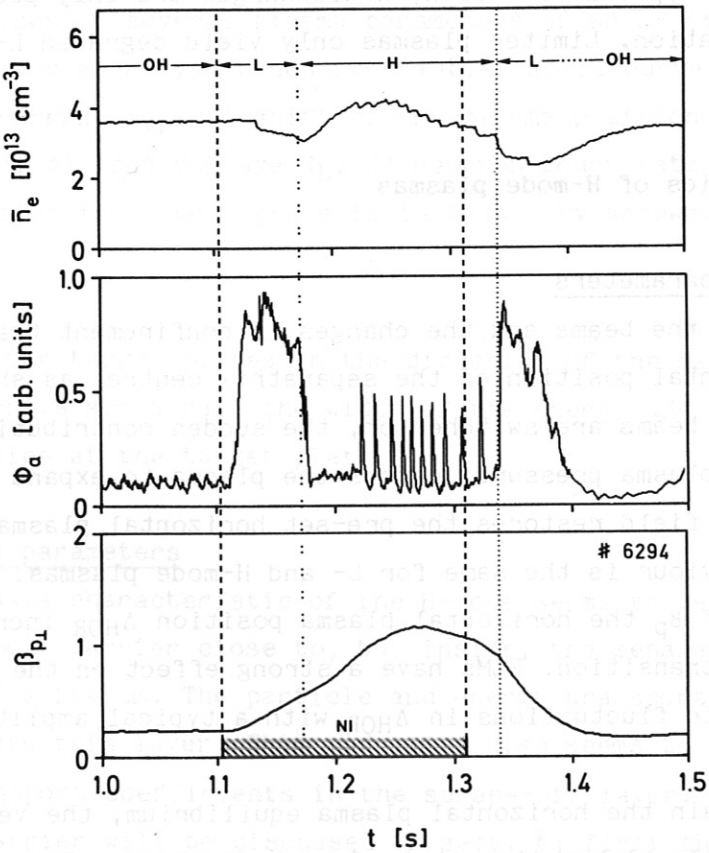

Fig. 2 Variation of the line averaged electron density $\bar{n}_e$, the atom flux ϕ_a emerging from the neutralizer plate at the separatrix intersection, and $\beta_{p\perp}$ from the diamagnetic loop during the neutral injection (NI) phase (hatched time interval) and during the different confinement regimes H and L.

confinement properties of the H-phase. These fluctuations have been dubbed edge localized modes (ELMs) because they affect primarily the plasma boundary /3/. By expanding the plasma major radius R_o in ASDEX from 165 cm to 170 cm ELMs can be avoided for 100-120 ms. These discharges are termed quiescent H-discharges (H*). They display the intrinsic transport properties of the H-mode without the additional MHD losses superimposed by the ELMs /4/.

There are several regimes with auxiliary heating which demonstrate improved confinement. An H-mode is characterized by a spontaneous and sharp transition during the beam phase. The transition is best indicated by the sudden drop of recycling signals in the divertor chamber and a simultaneous increase of the particle and energy contents /5, 6, 7, 8/. The development of confinement regimes always follows the symmetric pattern OH-L-H-L-OH. The improvement in energy confinement time in the H-mode is substantial, a factor of 2 being typical. In ASDEX, H-discharges are only possible in the divertor configuration. Limiter plasmas only yield degraded L-mode confinement.

2. Characteristics of H-mode plasmas

2.1. Equilibrium parameters

The initiation of the beams and the changes in confinement transiently affect the horizontal position of the separatrix centre, as shown in Fig. 3b. When the beams are switched on, the sudden contribution of the beam ions to the plasma pressure, causes the plasma to expand horizontally till the vertical field restores the pre-set horizontal plasma position. This initial behaviour is the same for L- and H-mode plasmas. Because of the improvement of β_p the horizontal plasma position Δ_{HOR} increases once more after the H-transition. ELMs have a strong effect on the plasma equilibrium and lead to fluctuations in Δ_{HOR} with a typical amplitude of 0.5 cm /9/.

In order to maintain the horizontal plasma equilibrium, the vertical field of an H-discharge is higher than that of an L-discharge; Fig. 3a compares the current I_{VF} in the vertical field coils of an L- and a comparable H-discharge. The rise of I_{VF} with beam heating is nearly twice that of an L-discharge of similar plasma and beam setting owing to the 2-fold increase in β_p.

The higher vertical field in the H-phase affects the separatrix position in the divertor chamber, too, and causes a shift of the intersection of the

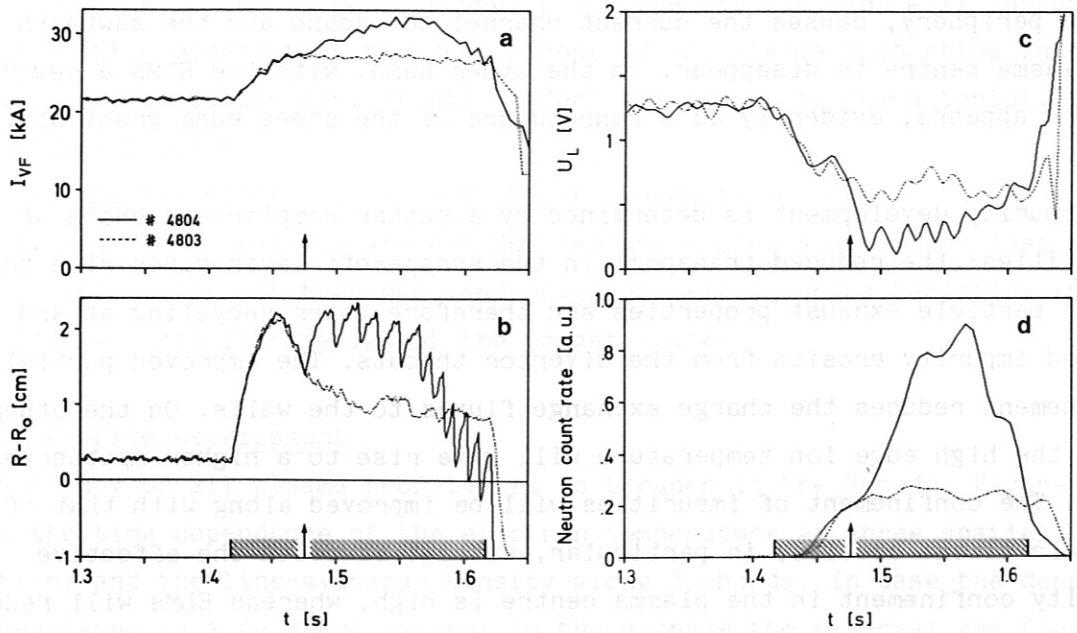

Fig. 3 Comparison of several plasma parameters of an L- (#4803, dashed curve) and an H-type discharge (#4804, solid curve); a) vertical field current I_{VF}; b) shift of the plasma position $R-R_o$ (R_o = 165 cm); c) loop voltage U_L; d) neutron count rate ϕ_n. The transition into the H-phase is indicated by arrows.

separatrix with the target plates in the direction of the main plasma by about 1 cm, which is about half the width of the energy and particle deposition profiles at the target plate.

2.2. Main plasma parameters

The dominant plasma characteristic of the H-mode seems to be the development of a transport barrier close to, but inside, the separatrix with a radial extent of a few cm. The particle and energy transport coefficients are reduced within this layer. This reduction also seems to reduce the cross-field transport coefficients in the scrape-off layer. The aspects of the transport barrier will be discussed in sect. 6; first the changes in plasma properties caused by it are described here: the transport barrier gives rise to rather broad plasma profiles with high peripheral values and steep gradients at the edge.

The profile change affect the MHD behaviour of the discharge: the high electrical conductivity at the edge, corollary to the good confinement up

to the periphery, causes the current channel to expand and the sawteeth in the plasma centre to disappear. On the other hand, with the ELMs a new MHD feature appears, evidently as a consequence of the steep edge gradients.

The impurity development is determined by a rather complicated chain of causalities: the reduced transport in the scrape-off layer gives rise to better particle exhaust properties and therefore lower recycling at and reduced impurity erosion from the divertor throats. The improved particle confinement reduces the charge exchange fluxes to the walls. On the other hand, the high edge ion temperature will give rise to a higher sputtering yield. The confinement of impurities will be improved along with that of the main plasma species; in particular, without sawteeth the effective impurity confinement in the plasma centre is high, whereas ELMs will reduce it in the boundary. The superposition of these different erosion and confinement effects determines the evolution of the impurity concentration in the plasma and the development of steady-state conditions.

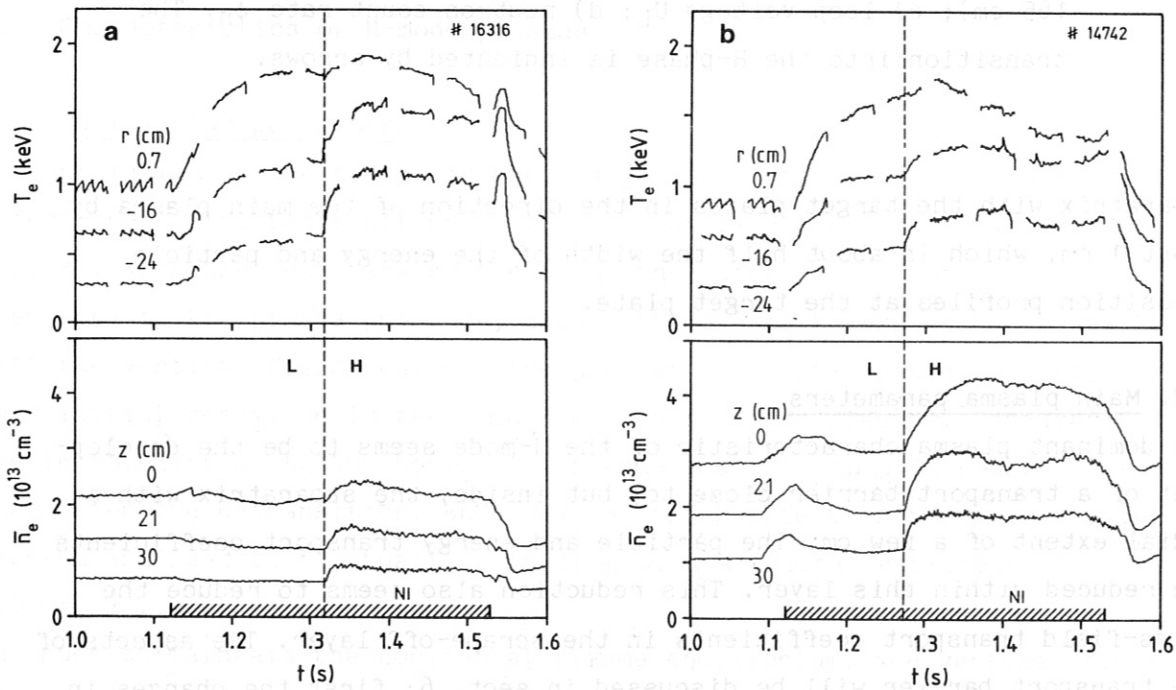

Fig. 4 Electron temperature and line averaged density at three positions during the beam phase with H transitions at the dashed vertical line. In case a) the density was regulated by a feed-back system; in case b) the internal gas flux was increased just prior to the beam pulse and kept at a constant level.

The broadening of the current channel after the H-transition will introduce a further time constant in the development of the plasma properties in the H-phase and, in particular, it will affect the stability characteristics at high plasma pressure.

Finally, the transport barrier affects the power fluxes out of the discharge, and ELMs - being a violent MHD feature - open a new power loss channel with different transport and power deposition characteristics which may require a specific design of the target plates.

2.2.1. Profile development

The tendency of all plasma profiles is to broaden in the H-mode. Figure 4 shows the time dependence of the electron temperature at three spatial locations and the line-averaged density along 3 chords. In case the density was regulated by a feedback system; in the H-phase the external gas flux becomes zero. In case a strong and constant gas flux was maintained during the beam phase. This additional gas flux was initiated shortly prior to the beam pulse and caused the ohmic density to rise. At the H-transition, T_e

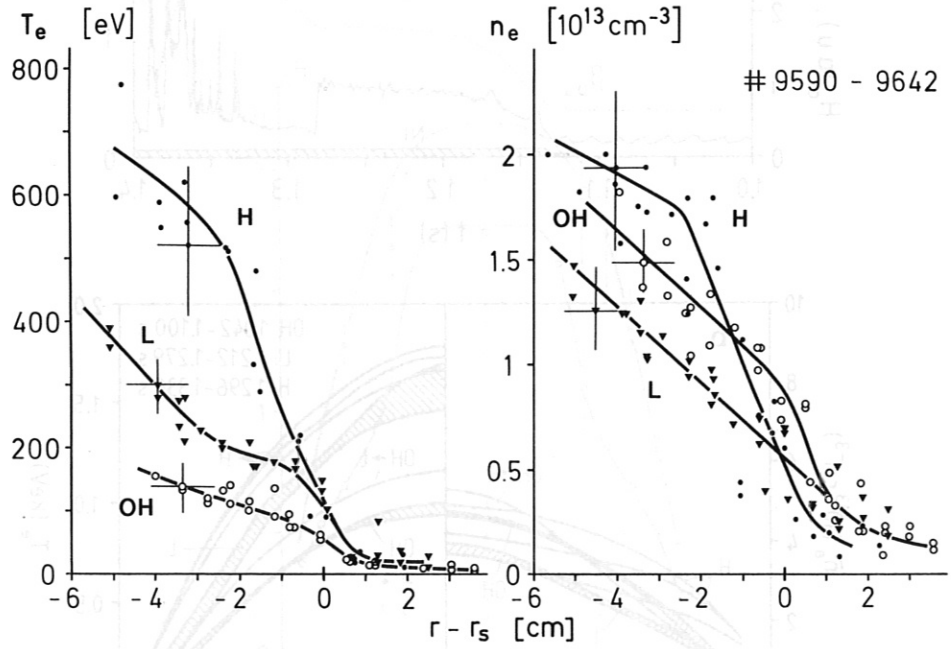

Fig. 5 Radial profiles of electron temperature T_e and electron density $\bar{n}_e$ at the plasma boundary for the 3 different confinement regimes OH, L and H. r_s is the separatrix radius. (The uncertainty in defining r_s is indicated by the horizontal error bars.) I_p = 0.32 MA, $\bar{n}_e = 4 \times 10^{13}$ cm^{-3}, P_{NI} = 2.85 MW.

rises if $\bar{n}_e$ is kept constant, in the other case there is a sharp rise in density. The relative increases rise of T_e and $\bar{n}_e$ toward the plasma edge. The edge electron density and temperature can be separately measured in ASDEX by using the edge Thomson scattering system. H-mode profiles at the plasma edge are plotted in Fig. 5 and compared with L-mode and OH results. As the diagnostics are limited to 5 observation channels which are spatially fixed, the plasma horizontal position was shifted from discharge to discharge to increase the spatial range. Remarkable are the high edge electron temperature of about 600 eV a few cm inside the separatrix and the steep gradient within the last 2 cm up to the separatrix. The H-mode for these measurements was one with ELMs; the data shown in Fig. 5 therefore represent average values such as develop with ELMs. No Thomson measurements of the edge profiles are available in quiescent H-discharges.

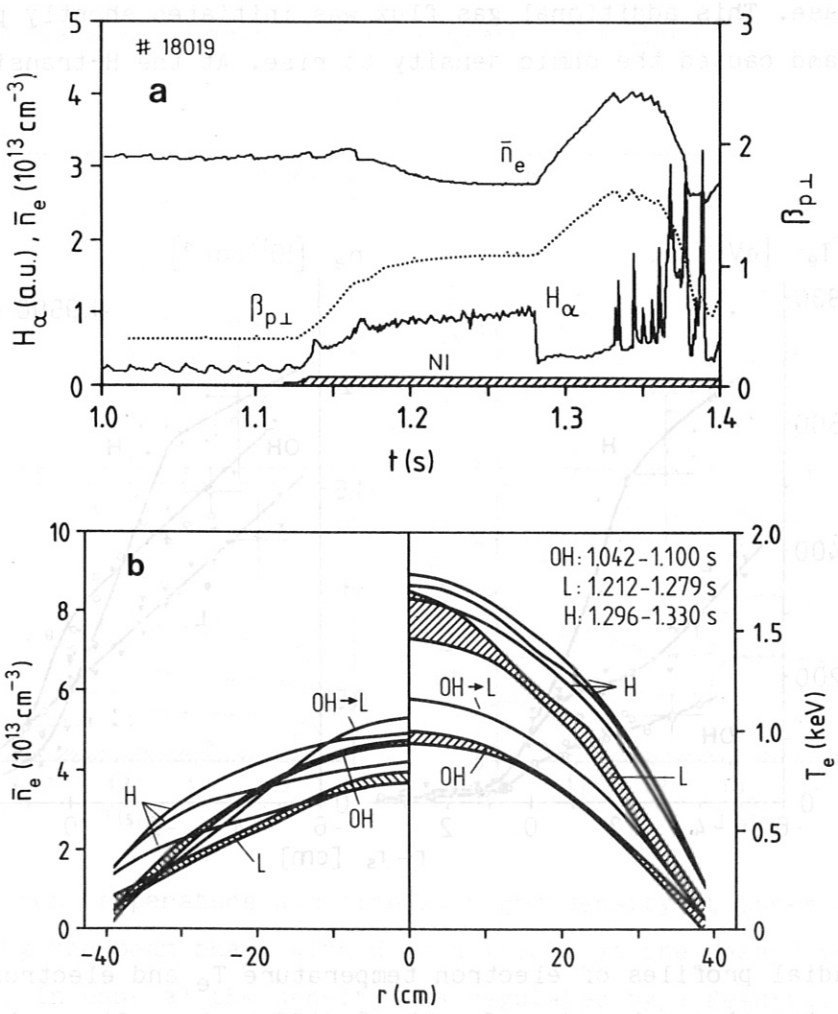

Fig. 6 Electron temperature and density profile development from the Ohmic phase into the L- and H-phases. For reference density, β_p and H_α-radiation in the divertor chamber are given.

Figure 6 shows the development of T_e and $\bar{n}_e$ profiles from the OH- via the L-phase into the H-phase measured with the multi-pulse Thomson scattering system, which gives a profile every 17 ms. High T_e and $\bar{n}_e$-values at the periphery are quickly developed in the H-phase from one laser time-point to the other. In some cases, both T_e- and $\bar{n}_e$-profiles develop shoulders at the edge. The density continuously increases after the H-transition and seems to develop along a different time scale. In this phase both the central T_e- and T_i-values decrease.

The T_e gradient at the edge increases from 45 eV/cm by a factor of 4 to 185 eV/cm. This increase reflects a change of the plasma heat diffusivity at the edge, which will be discussed in more detail in sect. 6.2.

The electron pressure at the edge increases from 1×10^{-4} W s/cm^4 by a factor of 6. The steep gradient at the edge of the H-mode plasma may provide the instability conditions for ELMs which will be discussed in sect. 2.3.

The increase of the electron temperature in the H-mode causes a further decrease of the loop voltage, which in some cases is close to zero.

Figure 3c compares the development of the loop voltage of an L- and an H-discharge. As the plasma current is driven partly inductively and with tangential beam heating in ASDEX and partly by the beams, no effort has been made to unravel possible bootstrap contributions to the plasma current at high β_p.

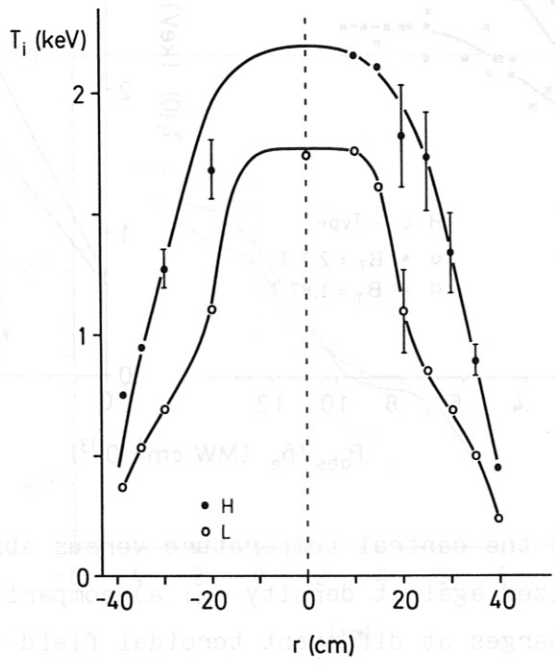

Fig. 7 Ion temperature profiles in the H-phase and at the end of the preceding L-phase as measured by passive charge exchange. I_p = 0.38 MA; B_t = 2.2T; P_{NI} = 3.3 MW.

Figure 7 finally compares Ti-profiles measured by passive charge exchange in the pre-transition phase with those in the H-mode. The tendency of the Ti-profile is to broaden also with the development of high values at the periphery. The high edge ion temperatures will give rise to increasesd charge exchange wall sputtering in the H-mode with the danger of higher impurity influx.

The thermal neutron flux ϕ_n increases after the H-transition with H^o injection into a D^+ plasma, as shown in Fig. 3d in comparison to an L-discharge. The increase in ϕ_n is mostly due to the rise in density in a confinement situation where, however, the ion temperature profile broadens. The heating efficiencies for electrons and ions $\eta_{e,i}$ ($\eta_{e,i}=\bar{n}_e \times \Delta T_{e,i}/\Delta P_{abs}$ = rise of electron or ion temperature with heating power normalized to line-averaged density) are found to be higher in the H-mode than the L-

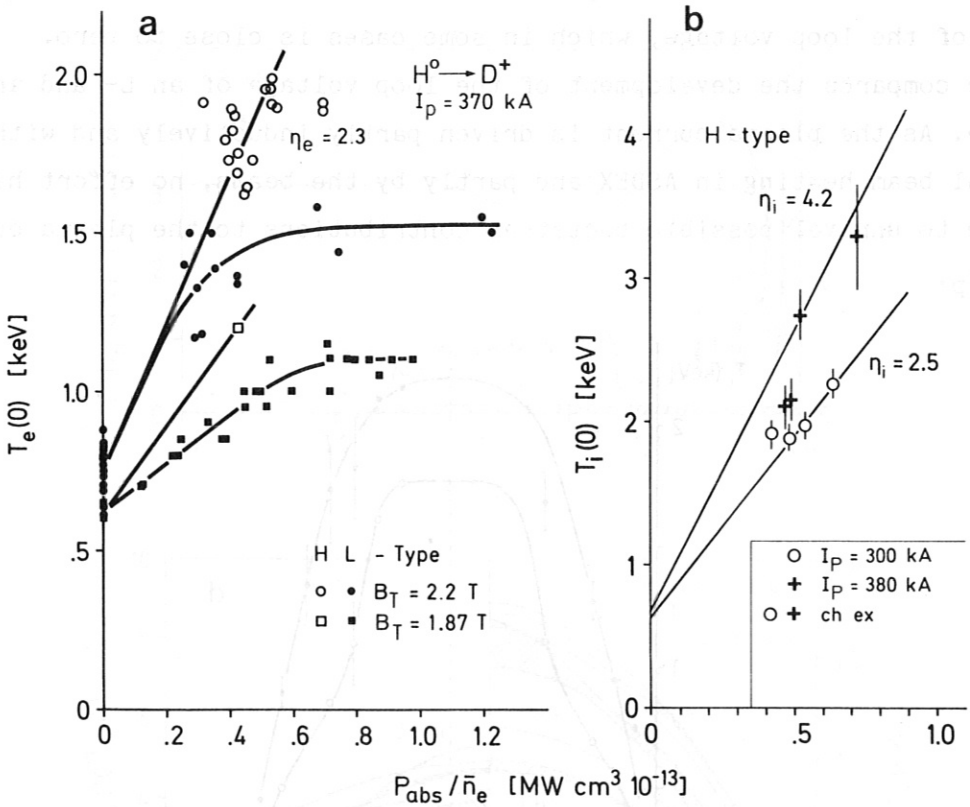

Fig. 8 Variation of the central temperature versus absorbed beam power P_{abs} normalized against density $\bar{n}_e$: a) comparison between L- and H-type discharges at different toroidal field values with NI into deuterium plasmas. η_e is the electron heating efficiency. b) central ion temperature versus $P_{abs}/\bar{n}_e$ for L- and H-type discharges at different plasma currents. η_i is the ion heating efficiency.

mode; in particular, T_e does not seem to saturate in the H-mode as in the case of the L-mode (see Fig. 8). For a plasma current of 300 (380)kA, n_i improves from 1.6 (2.8) keV/MW $cm^3 x 10^{13}$ in the L-mode to 2.5 (4.2) keV/MW $cm^3 x 10^{13}$ in the H-mode.

2.2.2. Scrape-off layer and divertor plasma parameters

The scrape-off layer (s.o.l) electron density in ASDEX is inferred from the intensity of the light emitted from lithium atoms which are impact excited by electrons in the scrape-off layer. The Li-beam is injected from the outside in the plasma mid-plane; the characteristic Li-light is measured perpendicularly at 10 spatial points along the beam.

Figure 9 compares the radial dependence of the electron density in the ohmic phase, the pre-transition L-phase and the H-phase between ELMs. The density shows a steep radial variation after the H-transition with a fall-off length λ_n which drops from 2.8 cm in the L-phase to 1.2 cm. In the H-phase λ_n is even smaller than in the OH phase, where λ_n = 1.9 cm is measured. λ_n is determined by perpendicular diffusion in the s.o.l. in the time it takes particles to drift along the magnetic field from the mid-

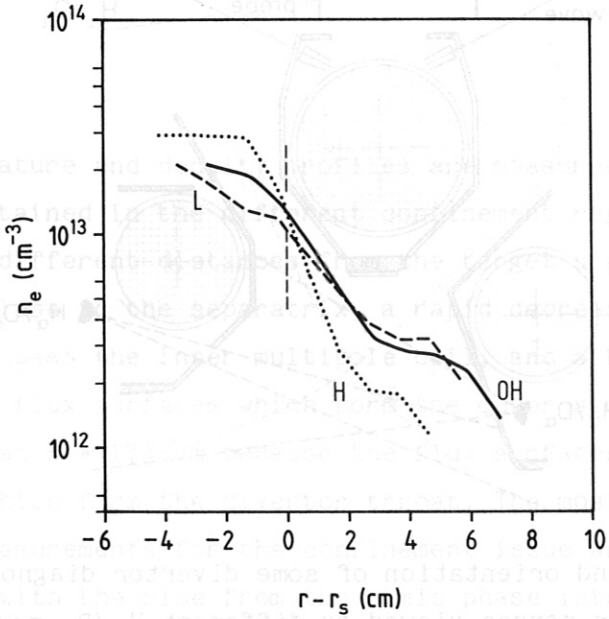

Fig. 9 Electron density in the scrape-off layer as measured by the lithium beam technique for OH-, L- and H-phases; r_s is the separatrix radius (40 cm).

plane onto the target plates located inside the divertor chambers. The decrease of λ_n in the H-phase reflects the reduction of the cross-field transport coefficient, which is equivalent to the increase of λ_n in the L-phase (λ_n becomes a function of heating power /10/), which is caused by increased perpendicular particle transport.

Figure 10 shows the location and the viewing angle and direction of different divertor diagnostics. The line-averaged electron density is measured interferometrically by a μ-wave system. The characteristic variation of the line density during the NI phase is plotted in Fig. 11. During the L-phase the line density increases up to a maximum and then decreases toward the ohmic level. At an H-transition this decrease occurs quickly. This variation seems to be the leading feature but it can easily be masked by changes in the external gas fuelling, to which the boundary layer density reacts sensitively, or by changes of the parallel flow velocity. The typical variation of the line density as described above and shown in Fig. 11 can be analyzed as a corollary to the particle confinement variation of the main plasma /11, 12/. During the H-phase, ELMs strongly modulate the line density.

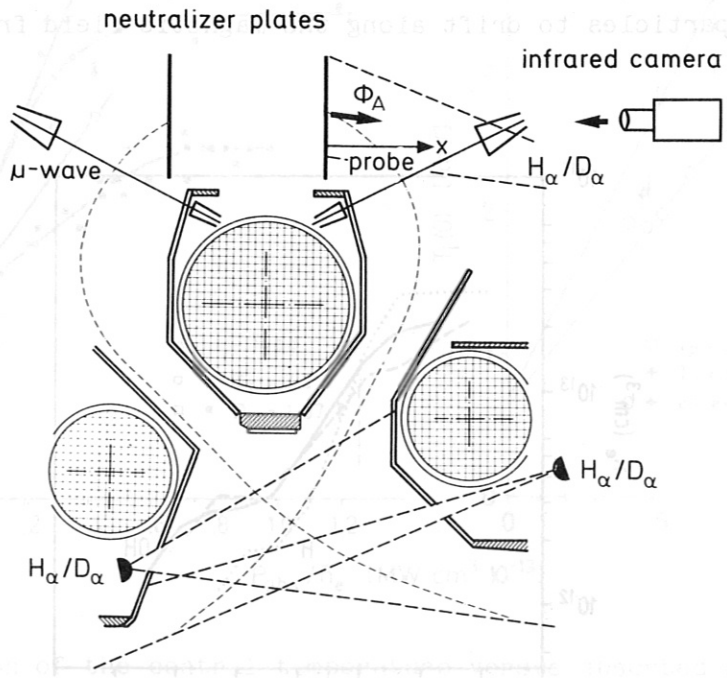

Fig. 10 Location and orientation of some divertor diagnostics. Shown are the angular ranges viewed by different H_α/D_α monitors; the chord, sampled by the Langmuir probe; the location of inside and outside μ-wave horns to measure the electron line density; the origin of the reflected flux ϕ_a at the intersection of separatrix and neutralizer plate; the line of sight of the infrared camera.

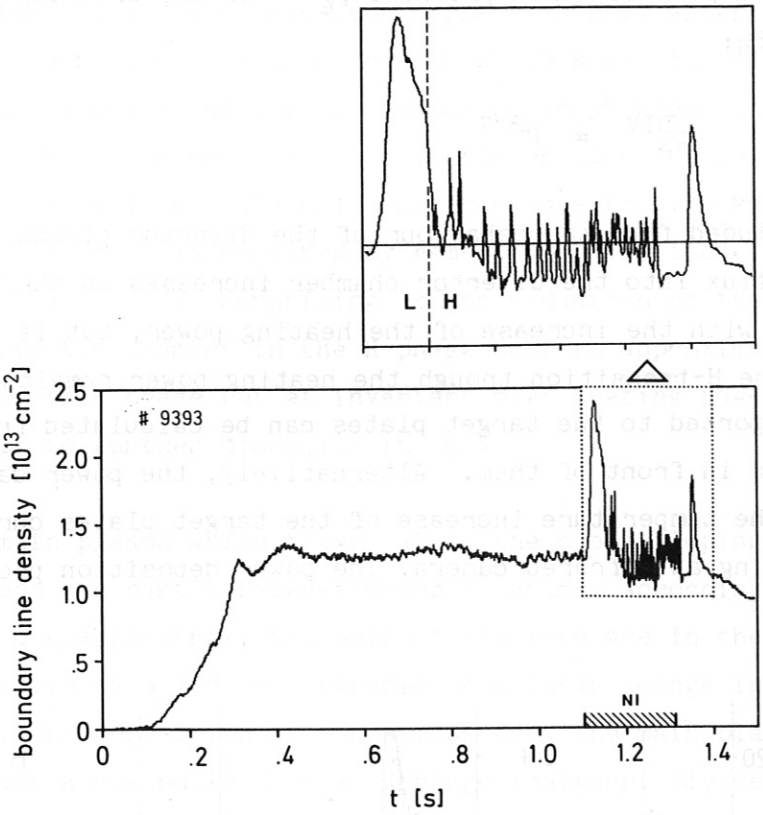

Fig. 11 Time dependence of the inner boundary layer line density; the NI-phase is plotted at an expanded time scale. I_p = 0.3 MA, $\bar{n}_e$ = 3 x 10^{13} cm^{-3}, P_{NI} = 3.0 MW.

The electron temperature and density profiles are measured with Langmuir probes. Examples obtained in the different confinement regimes are plotted in Fig. 12 for two different distances from the target plates. The profiles have a sharp peak close to the separatrix, a rapid decrease at the of flux surfaces which encompass the inner multipole coil, and a broad shoulder on the other side with flux surfaces which form the outer s.o.l. The shoulder is sharply cut off at R = 173 cm because the flux surfaces at larger radii intersect shields which form the divertor throat. The most important aspects of these measurements for the confinement issue are the variation of the peak values with the rise from the ohmic phase into the L-phase and then the drop back to the low peak values of the ohmic phase in the H-mode. For example, the peak electron pressure $\bar{n}_e * T_e$ increases from 20 (10^{13} eV cm^{-3}) in the ohmic phase to 50 (10^{13} eV cm^{-3}) in the L-phase and then back below 20 (10^{13} eV cm^{-3}) in the H-phase. The most simple one-dimensional

model relates the peak electron pressure p_e^{DIV} of the divertor plasma to the power flux P_H:

$$p_e^{DIV} \propto P^{2/7} \qquad (1)$$

It must be concluded from the behaviour of the divertor plasma parameters that the power flux into the divertor chamber increases in the L-mode in rough agreement with the increase of the heating power, but it is sharply reduced after the H-transition though the heating power remains the same. The power transported to the target plates can be calculated from the plasma parameter in front of them. Alternatively, the power can be measured from the temperature increase of the target plates during the discharge by using an infrared camera. The power deposition profile at the

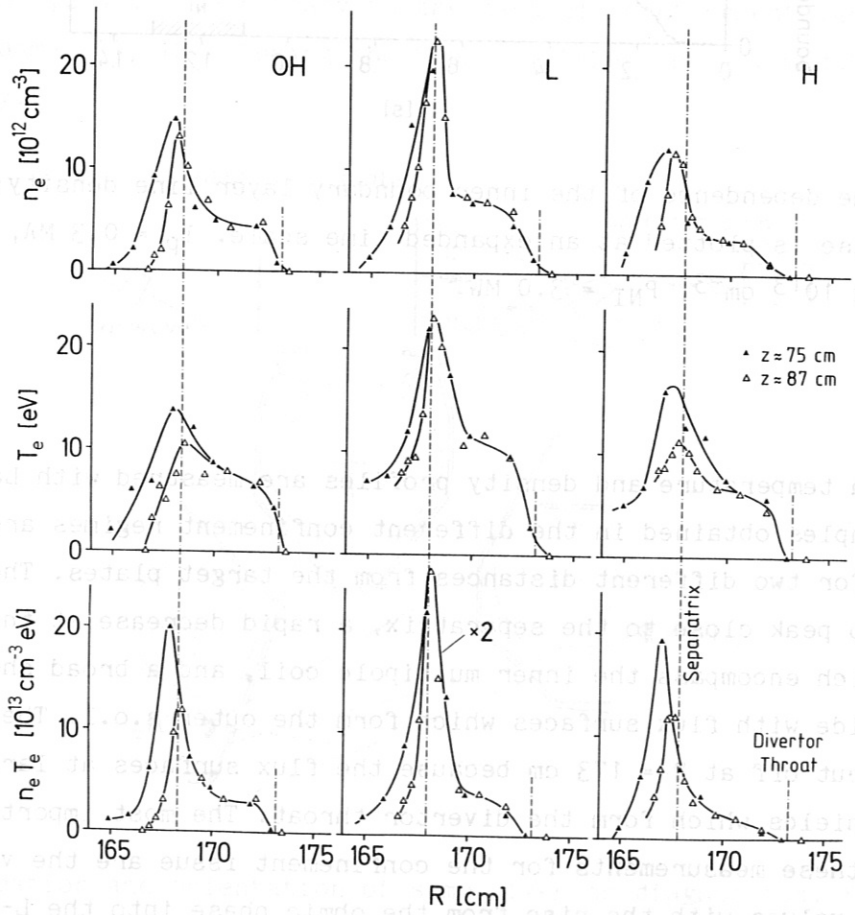

Fig. 12 Radial profiles of electron density, temperature and pressure of the divertor plasma at two positions from the target plates in OH-, L- and H-phases. I_p = 0.32 MA, $\bar{n}_e$ = 3.6 x 10^{13} cm^{-3}, P_{NI} = 3.1 MW.

outer target plate is shown in Fig. 13, again for the 3 confinement phases, i.e. the OH-, the L-, and the quiescent H-phase shortly after the transition. The peak power flux increases from about 10 W/cm^2 in the ohmic phase to 220 W/cm^2 in the preceding L-phase and drops to 35 W/cm^2 in the H-phase. The integrated power recovered in the divertor chamber (deposition plus radiation) is 0.25 MW in the OH-phase and increases to 1.85 MW in the L-phase. This variation is in expected agreement with the increase in heating power from 0.35 MW to 3 MW. Surprising is the reduction of the recovered power in the divertor chamber in the H-phase back to approximately the same value as in the ohmic phase but at invariant high heating power. This observation will be further discussed in sect. 6.

Ions from the main plasma which travel along the s.o.l. impinge on the target plates and are partly backreflected as atoms. According to the ion temperature at the separatrix, the bulk of the ions are in the energy range of 100 to a few 100 eV and do not experience a large change in energy after backreflection. The deposition of these ions from the main plasma can be measured by using a scannable charge exchange analyser. Figure 14 shows deposition profiles for L- and H-phases. The increased perpendicular diffusion coefficient D, which extends into the s.o.l. - as was documented by the behaviour of the s.o.l. density in Fig. 9 -, broadens the profile in the L-mode (in comparison with the OH-profile) and the reduction of D in the H-mode (between ELMs) causes it to shrink. The additional increase of β_p in the H-phase gives rise to a shift of the deposition maximum.

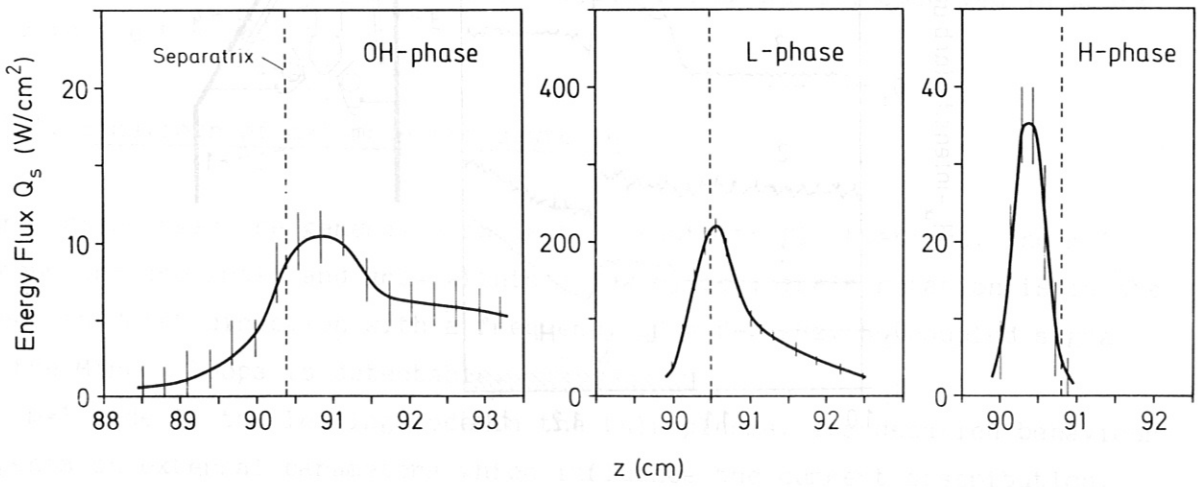

Fig. 13 Power deposition profiles at the upper outer target plate during OH-, L- and H*-phases. P_{NI} = 3 MW.

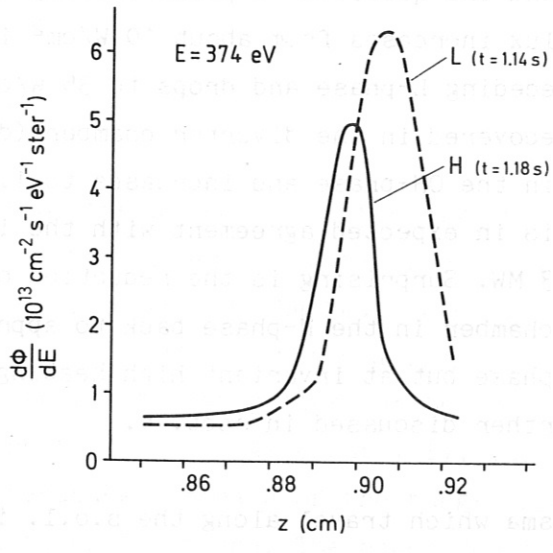

Fig. 14 Measured backscattering profiles during neutral injection of 2.8MW into L-discharge at initial injection phase (at 1.14 s, neutral injection starts at 1.1 s) and after H-transition 40 ms later (at 1.18 s). Displacement of backscattering profile is due to higher vertical magnetic field in the H-phase.

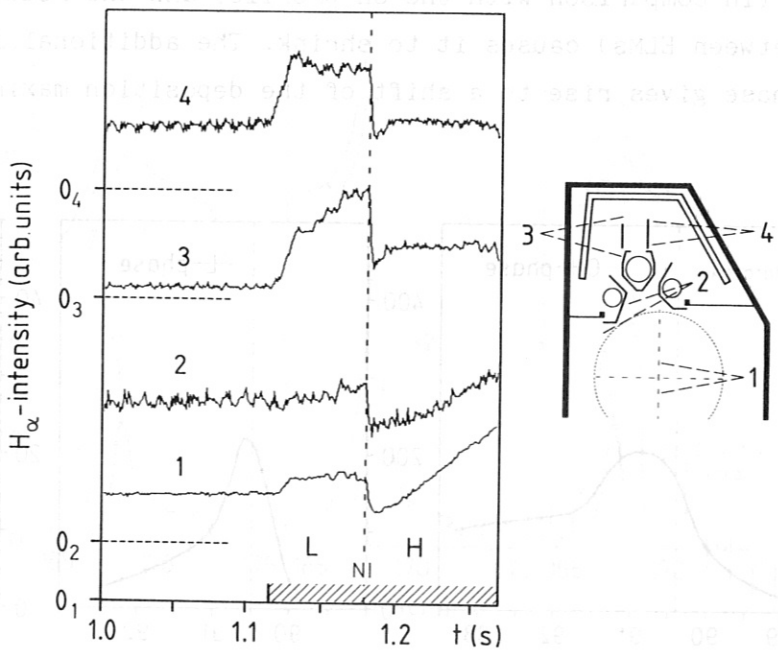

Fig. 15 Variation of the H_α intensity at different viewing angles (as shown in the insert) with neutral injection and at the L-H transition.

As the energy of the particles is measured, their residential time in the s.o.l. can be calculated by using 15 m as the average path length from the plasma mid-plane to the target plate; by assuming diffusive perpendicular transport in the s.o.l. it is possible to obtain a value of D which best fits the measured profiles. The following diffusion coefficients in the s.o.l. are obtained: D_{OH} = 4500 cm^2/s; D_L = 8000 cm^2/s; D_H = 3500 cm^2/s.

The recycling of hydrogen changes in the H-mode since the interaction of the s.o.l. with the vessel wall is reduced. Furthermore, a plasma with better particle confinement requires less gas influx to maintain the same particle content and to compensate the diffusive losses. At all positions where ASDEX is instrumented with H_α-monitors (they are uncalibrated and hence unsuitable for absolute determination of the ionization rate) the H_α intensity decreases at the transition. The H_α-radiation at locations important for recycling (divertor chamber and neck, stagnation point, typical wall section) are shown in Fig. 15. Because of the reduced recycling and because of the well-localized ionization of hydrogen in the region with steep gradients, the plasma boundary is sharp and well defined in the H-mode.

2.3. MHD characteristics of the H-mode

In this section we will discuss the MHD properties in the H-mode away from the β-limit. They are largely determined by the high edge electron temperature, which causes the current channel to expand and q(0) in the plasma centre to increase, and by the steep edge gradients, which provide the instability condition for ELMs - a new type of instability observed in ASDEX only in the H-mode.

2.3.1. Behaviour of m=1 mode and sawteeth

Ohmic discharges are generally subject to sawtooth fluctuations. The m=1 precursors are small and grow within a few cycles; their rotation is in the electron drift direction with a frequency of a few kHz. No coupled signal on the Mirnov loops is detectable.

The m=1 mode is the leading mode in the bulk plasma. Its detailed behaviour depends on external parameters which influence the current distribution, i.e. the plasma configuration (limiter vs. divertor), the NI power level, and the local electron transport properties, which are different in L and H-discharges and in hydrogen and deuterium plasmas.

NI into limiter discharges gives rise to periodically growing m=1 modes which cause sawtooth disruptions and then vanish. The sawtooth repetition time $\tau_{s.t.}$ increases somewhat with NI power but quickly saturates at about 35 ms.

Different behaviour is observed in divertor discharges. Figure 16 shows the m=1 and sawtooth behaviour at three different power levels. At low NI power (Fig. 16a), the m=1 amplitude is small and its occurrence is repetitive, being terminated by a sawtooth. Contrary to the limiter case, $\tau_{s.t.}$ increases with beam power. At an injection power above 2MW (Fig. 16c), the divertor discharges are free of sawteeth except for a single sawtooth at the beginning of the NI pulse. This sawtooth is caused by a slowly growing m=1 mode which leads to reconnection after about 50 cycles. After the sawtooth, when q_o has sufficiently dropped below 1 again, an m=1 mode appears which saturates at a large amplitude without giving rise to any further sawtooth. This change indicates the transition from a resistive to an ideal internal kink mode behaviour. Irrespective of the MHD fluctuation level, all three examples of Fig. 16 represent L-type discharges with deteriorated confinement.

In L-type discharges, the large m=1 mode can persist throughout the NI pulse. The β_p-values of the L-mode are sufficient to produce m≧2

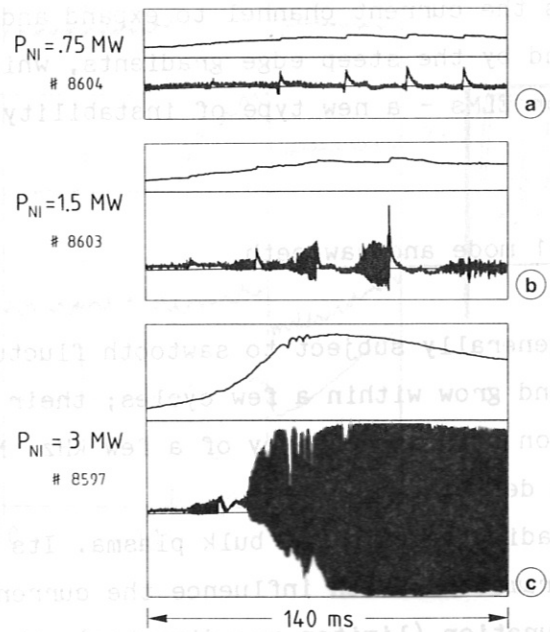

Fig. 16 Central soft X-ray signals showing the evolution of m = 1 modes and sawteeth during NI at different beam powers P_{NI}.

components of the same frequency and with the same amplitude variation as the driving m=1 mode. For example, sawtooth crashes lead to the disappearance of the mode amplitude in the Mirnov coils, as shown in Fig. 17. At the beginning of the NI pulse, the modes still rotate in the electron drift direction. Later in the NI phase, they rotate in the ion direction owing to the imparted angular momentum of the two co-beams.

The typical MHD behaviour of an H-discharge is shown in Fig. 17. Plotted are the signals of a near-centre soft X-ray detector (because of limited data storage two reproducible shots are necessary to show the SX-diode signal over the full NI-phase), an outside Mirnov loop, and, for reference, the signal of an H_α/D_α detector. As in the L-discharge, there is a single sawtooth at the beginning of the NI pulse and then large coupled m=1 and $m \geq 2$ modes. Figure 17 clearly illustrates the mode coupling: the exponential rise of the m=1 and $m \geq 2$ modes prior to the sawtooth and their disappearance at the sawtooth. Unlike the L-discharge, the coupled m=1, $m \geq 2$ modes disappear in the course of the H-phase. From the development of the m=1 mode with power, as summarized in Fig. 16, it is clear that a further broadening of the current channel will increase q above 1 and will cause the m=1 and its coupled modes to disappear. No internal mode is present thereafter and only ELMs, which give rise to sharp spikes on the

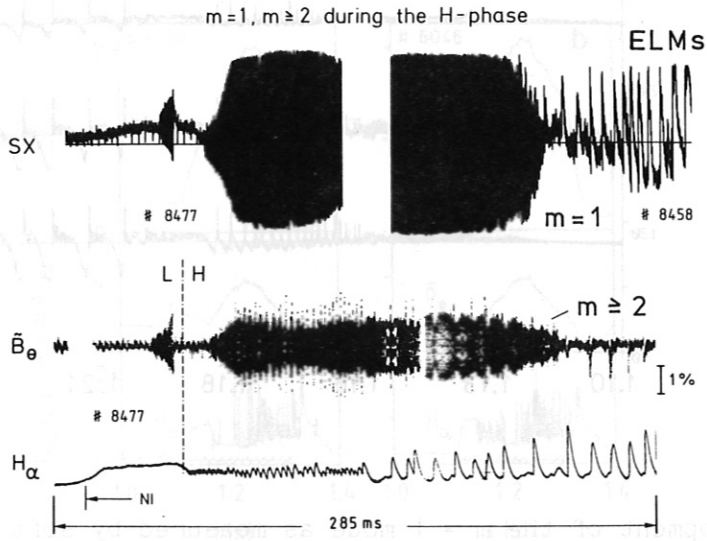

Fig. 17 Signals of a near centre soft X-ray detector (SX), an outside Mirnov loop ($\tilde{B}_\theta$) and an H_α/D_α detector (for reference) showing typical MHD behaviour (m = 1, $m \geq 2$ modes; sawteeth) during the H-phase.

Mirnov loop and soft X-ray signals, can be observed. The increase of q_o above 1 is supported by the analysis of the T_e-profiles as measured by ECE. These results shows that gross MHD behaviour, structured by the m=1 mode, affects neither global confinement nor the H-transition: L-type behaviour is found without large modes being present (see Fig. 16), whereas the H-phase can carry a large mode. The only obvious connection between MHD effects and the H-regime with good confinement is that the H-mode can be triggered by a sawtooth, as shown in Fig. 17. Sawtooth-initiated H-transitions mostly occur at high plasma current ($I_p \gtrsim 400$ kA, $q_a < 3$) and low injection power.

The requirement for an H-transition, however, is not $q_o > 1$, as is temporarily realized after a sawtooth. The transition can also occur with $q_o < 1$ and a fully developed m=1 mode present.

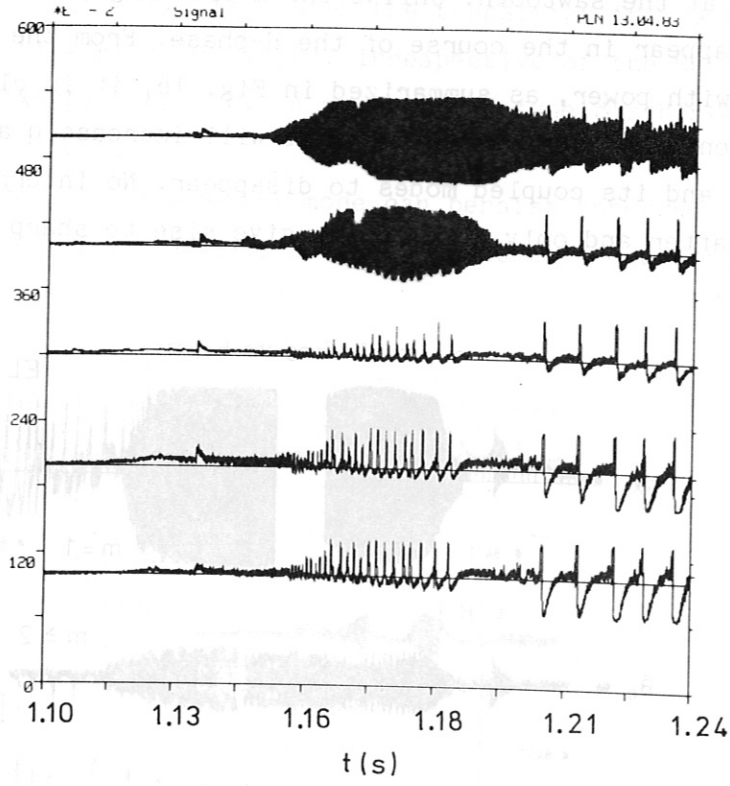

Fig. 18 Development of the m = 1 mode as measured by soft X-ray diagnostics during the H-mode which is triggered by the initial sawtooth. The upper channel views the plasma centre; the separation of the channels is 2.5 cm. The outer channels are modulated by ELMs.

Figure 18 shows an example of an H-mode transition without sawtooth trigger amidst a large saturated m≧1 mode. During the H-phase the mode disappears. The observation of the mode along different chords indicates that the q=1 surface shrinks in this process (see Fig. 18). At high plasma current and low injection power in deuterium discharges or up to the highest available power in hydrogen, sawteeth are also observed during the H-phase, thus demonstrating that q_o can vary in the H-phase in a periodic way between values above and below 1 as in other confinement regimes too.

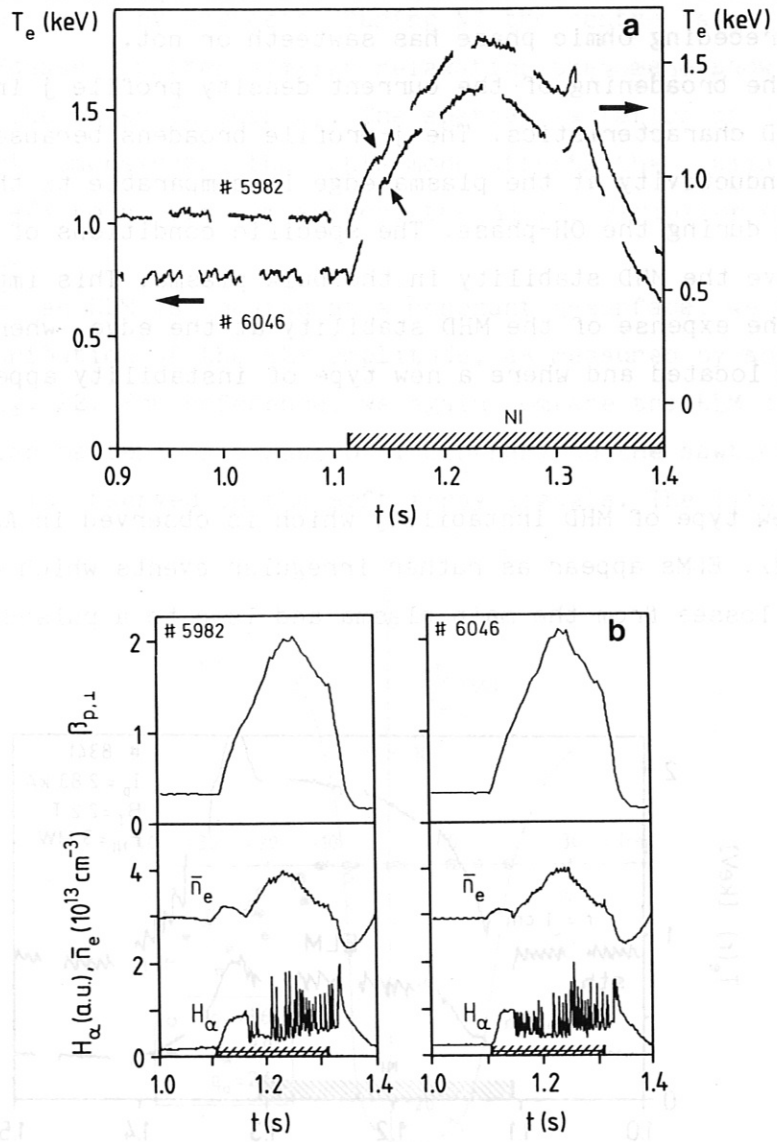

Fig. 19 a) central electron temperature for two discharges one with (#6046) and one without (#5982) sawteeth in the ohmic phase. The arrows devote the H-transition. b) compares the density, $\beta_{p_\perp}$, and H_α-radiation in the divertor chamger for the two cases.

It has been observed in DIII-D /13/ that the H-mode does not develop when NI is applied to an ohmic discharge without sawteeth. In ASDEX we had studied the importance of sawteeth in the ohmic phase for the development of the H-mode and compared discharges which only differed in this MHD aspect. Figure 19a shows the central electron temperature of the two discharges to document the lack of sawteeth in one of them. Figure 19b plots the time variation of the density, β_p and H_α in the divertor chamber. The comparison shows that the two discharges do not differ in any important aspect in the H-phase. Contrary to the DIII-D result, we come to the conclusion that it is irrelevant for the development of the H-mode whether the preceding ohmic phase has sawteeth or not.
In summary, the broadening of the current density profile j in the H-mode shapes the MHD characteristics. The j-profile broadens because the electrical conductivity at the plasma edge is comparable to that in the plasma centre during the OH-phase. The specific conditions of the H-mode seem to improve the MHD stability in the bulk plasma. This improvement is, however, at the expense of the MHD stability at the edge, where the steep gradients are located and where a new type of instability appears.

2.3.2. ELMs

ELMs are a new type of MHD instability which is observed in ASDEX in the H-phase only /3/. ELMs appear as rather irregular events which cause energy and particle losses from the main plasma and lead to a pulsed form of

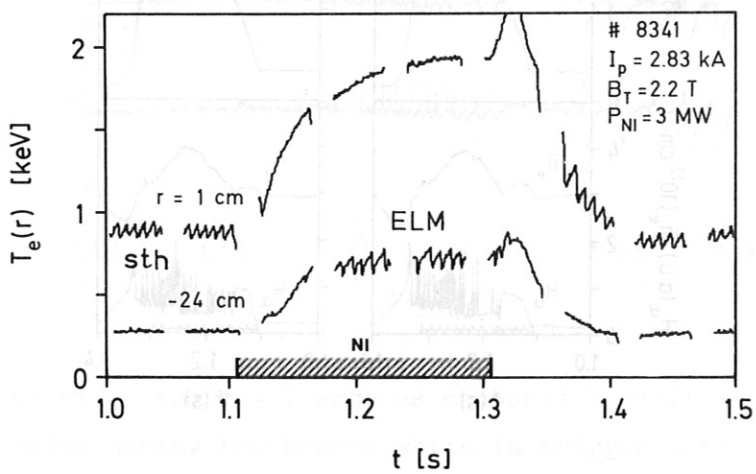

Fig. 20 ECE measured electron temperature T_e at the plasma centre (r = 1 cm) and half-way to the edge (r = -24 cm) showing that ELMs are localized in the outer part of the plasma. In the OH-phases the central T_e is modulated by sawteeth.

energy release into the divertor chamber. Since ELMs affect the plasma equilibrium through the reduction of β_p, lead to transiently enhanced recycling in the divertor (because of the enhanced power influx) and in the main plasma chamber (because of the increased fall-off length in the s.o.l.), and affect the confinement of the main plasma, practically all diagnostic signals respond to ELMs. ELMs are localized at the plasma edge. A first indication of the location of this mode is given in Fig. 20. Plotted is the ECE-measured electron temperature at the plasma centre (r = 1 cm) and halfway to the edge (r = -24 cm) during the NI phase, preceded and succeeded by ohmic phases. During the ohmic phases, the central T_e is periodically modulated by sawteeth. During NI the centre is unaffected, but - during the H-phase - rather similar relaxation phenomena show up as modulations on the outer T_e-channel. The spatial variation of $\Delta T_e/T_e$ as shown in Fig. 21 demonstrates that this mode affects the plasma roughly in the range from a/3 to a. For comparison, the $\Delta T_e/T_e$ variation of sawteeth is also plotted.

To study whether an ELM is located at a resonant q-surface, we investigated the radial distribution of the ELM amplitude, as measured by soft X-rays and shown in Fig. 22. For reference, we again compare the ELM distribution with the familiar pattern of a sawtooth. Contrary to the sawtooth, no inversion point is observed in the soft X-ray signals. The lithium beam

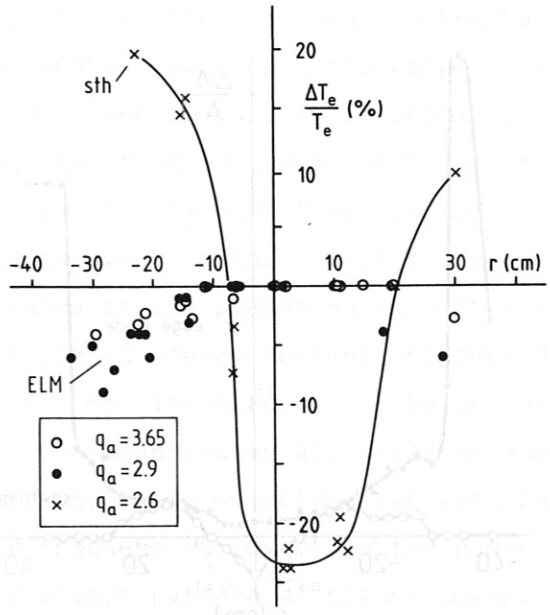

Fig. 21 The relative variation of the electron temperature versus plasma radius due to ELMs. The variation of T_e with ELMs is compared with that due to sawteeth.

diagnostic, which probes the local density around the separatrix during an ELM, shows an inversion point very close to the separatrix: during an ELM the density in the boundary layer increases at the expense of the density inside the separatrix. The soft X-ray emission profile shown in Fig. 22 exhibits a maximum at r = 36 cm. This maximum did not shift, when q_a (cylindrical definition) was varied between 2.4 and 5.6. It is therefore tentatively concluded that ELMs are not located at a fixed resonant surface (such as q = 2 or 3) but rather very close to the plasma boundary.
As ELMs are only observed in the H-mode, it is tempting to conclude that the crucial element which provides the H-mode - this seems to be the transport barrier at the edge - simultaneously gives rise to a new instability condition. As ELMs are localized close to the plasma edge, it is obvious to conclude that the steep edge gradients of the H-mode - either pressure or current density - are responsible for ELMs.
The explosive nature of ELMs leads to widening of the density fall-off length in the s.o.l. and a broadening of the particle and power deposition on the target plates. The increase of λ_n leads to transiently enhanced recycling as shown in strong H_α modulation (see Fig. 15), particularly in the divertor neck area where obstacles are closest. Figure 23 plots the power and particle deposition profiles at the target plates. The profiles as shown in Fig. 23 have to be compared with those during the quiescent

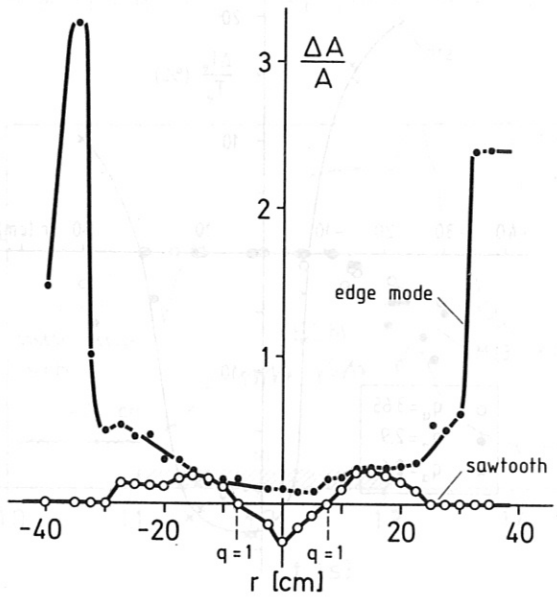

Fig. 22 Radial distribution of soft X-ray fluctuations connected with an edge localized mode and a sawtooth, respectively. The measurements indicate that ELMs are localized at the plasma edge.

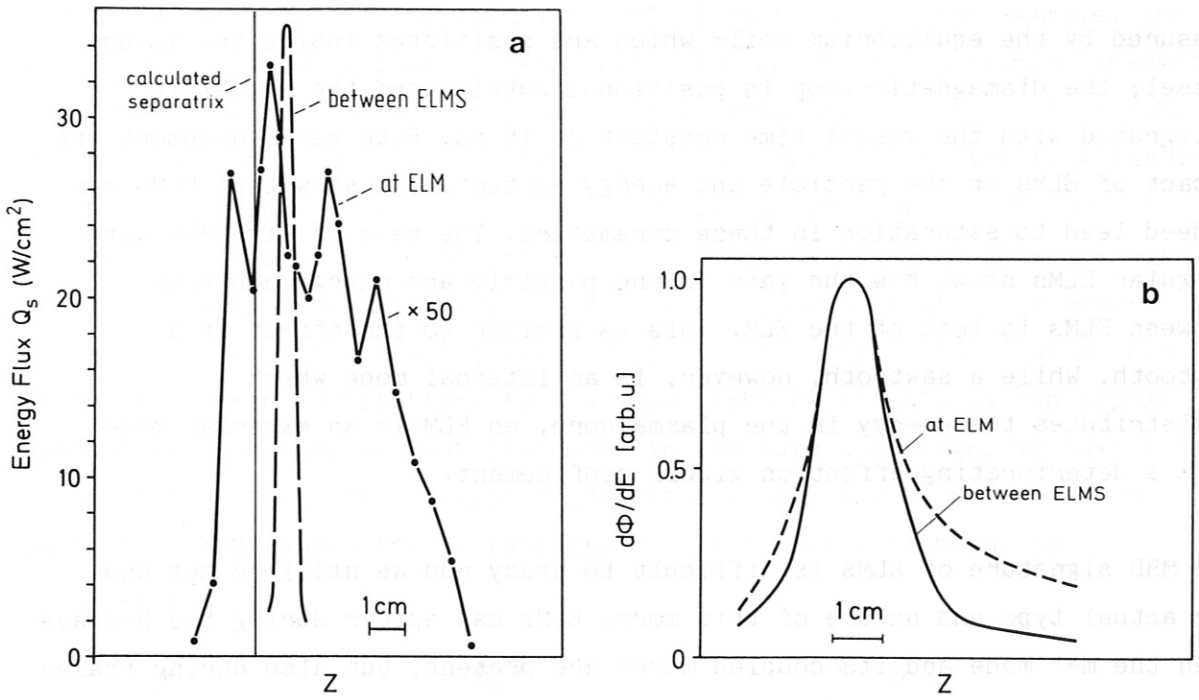

Fig. 23 Profile of (a) the power flux onto the target plate and (b) of the particles backreflected from the target plates at an ELM and between ELMs.

phases (also plotted in Fig. 23). 3. The power deposition profile width increases up to 7 cm and adopts rather irregular structures which vary from ELM to ELM. The integrated power onto the target plate can assume values up to 20 MW. The MHD part of the ELM is probably rather short and may last for only 10 μs; the enhanced power outflux from the plasma may last for 400 μs; the energy loss by an ELM can be up to 4 kJ onto one target plate, which, summed over all the target plates, corresponds to the energy content of an annulus at the plasma surface of several cm. Steady-state conditions for the plasma energy content are provided by ELMs alone at an ELM period of about 6 ms. The effect of ELMs on the confinement of an H-discharge cannot easily be assessed in all cases because ELMs can be of high frequency with small amplitude or seldom but with large amplitude. Generally, ELMs are more frequent at lower heating power and change to a less frequent but more distinct pattern at higher power. Figure 24 shows the development of the density, β_p, and the H_α-radiation in the divertor chamber for two cases: one which is characterized by frequent ELMs which suddenly stop for short quiescent periods and another one where a basically quiescent H-phase is interrupted by large ELMs. β_p, shown in Fig. 24, is

measured by the equilibrium coils which are positioned inside the vacuum vessel; the diamagnetic loop is positioned outside and the signal is integrated with the vessel time constant of 16 ms. Both cases document the impact of ELMs on the particle and energy contents and show that ELMs can indeed lead to saturation in these parameters. The case of Fig. 24b with singular ELMs shows how the gain in the particle and energy contents between ELMs is lost at the ELM. This is similar to the effect of a sawtooth. While a sawtooth, however, is an internal mode which redistributes the energy in the plasma core, an ELM is an external mode with a deteriorating effect on global confinement.

The MHD signature of ELMs is difficult to study and we still do not know the actual type and nature of this mode. ELMs can appear during the H-phase when the m=1 mode and its coupled modes are present, but also during phases with $q_o>1$ and no modes. (Both cases are shown in Fig. 17.) In cases where ELMs appear without modes, their inherent structure can be studied in more detail. Figure 25 shows signals from a Mirnov loop and a near-centre soft X-ray channel during an ELM. Although the sensitivity and time resolution

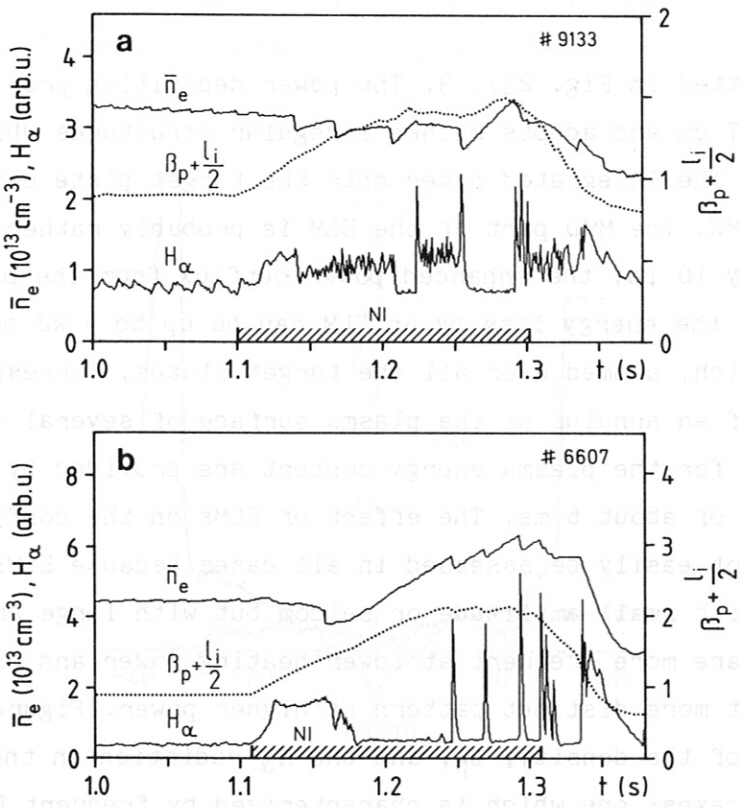

Fig. 24 Variation of density and $\beta_p + l_i/2$ (from the plasma equilibrium) (a) when ELMs suddenly are terminated or (b) with singular large ELMs.

of the two diagnostics are high and sufficient to show , for example, the growing m=2 mode preceding a major disruption or the m=1 precursor leading to a sawtooth, no similar oscillation is observed as precursor to an ELM. An ELM causes a sudden signal rise within less than 20 μs (the time resolution of the diagnostic) out of the quiet background level. ELMs do not seem to have a precursor oscillation; there are cases where ELMs are combined with a fishbone with a growing $m \geq 1$, n=1 signature which is erased after the ELM. Such a coupled event could erroneously be taken as an ELM with a precursor oscillation. As the same fishbone structures can appear without ELMs or ELMs without fishbones in the same discharge, we have to conclude that these are separated MHD events. The only connection seems to be that an ELM causes the instability condition for a fishbone to disappear.

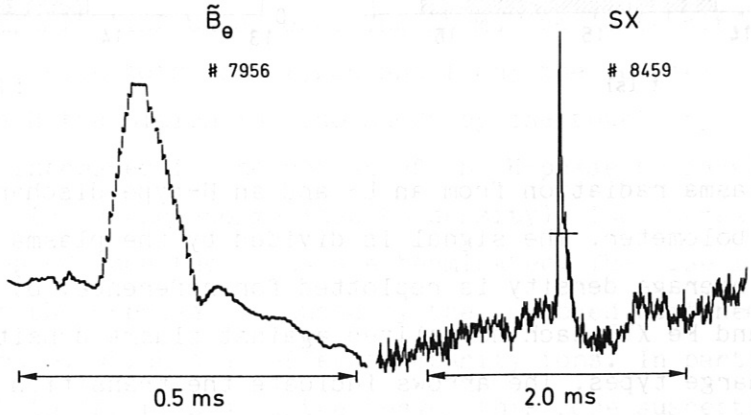

Fig. 25 Signals from a Mirnov loop ($\tilde{B}_\theta$) and a near centre soft X-ray detector (SX) showing the structure of an edge localized mode.

Since the repetition of ELMs is erratic, it is difficult to study the cause of their appearance. We find that their repetition time has the tendency to increase at lower current whereas the amplitude decreases, thus indicating that ELMs might be correlated to the current densities profile in the range of the steep T_e-gradient at the edge: As an ELM reduces the edge electron temperature, it might flatten the current profile there; between ELMs, the current profile steepens again, finally causing the next ELM. But no correlation of the ELM frequency has been observed when the plasma current was ramped up or down (when current was added or reduced specifically at the plasma edge during the H-phase).

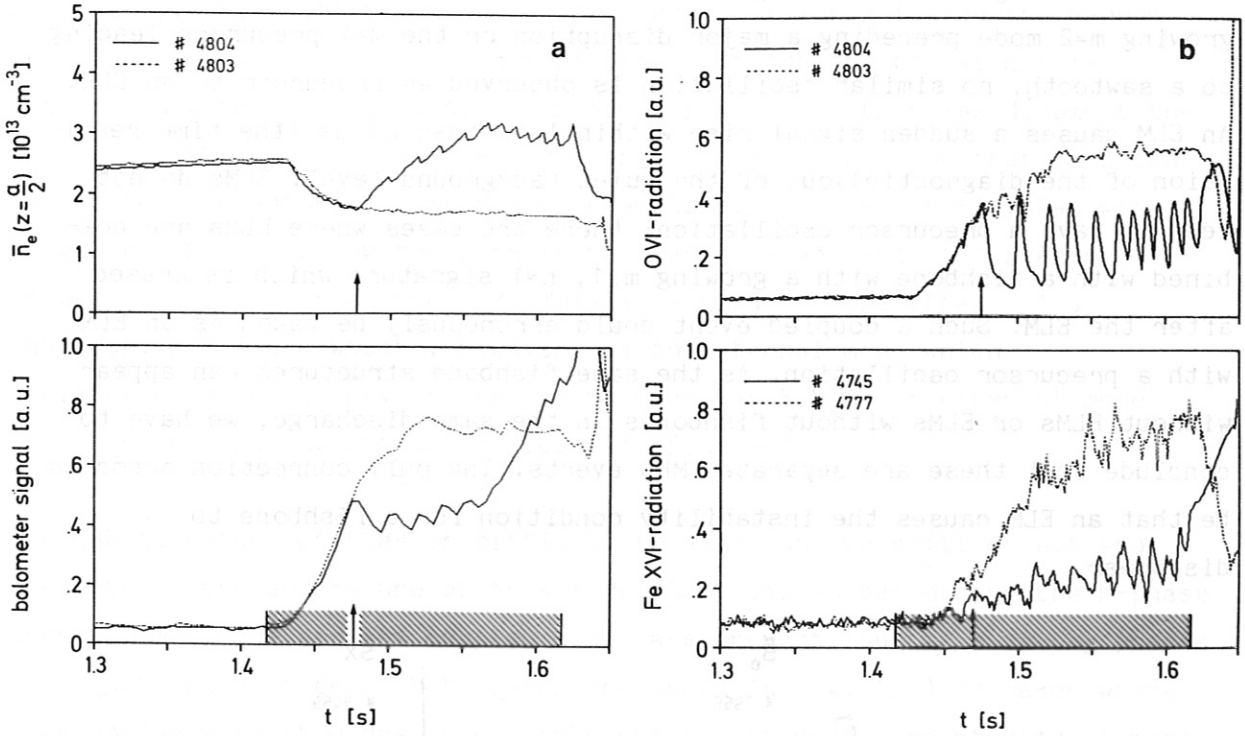

Fig. 26 a) Plasma radiation from an L- and an H-type discharge as measured by a bolometer. The signal is divided by the plasma density. The line average density is replotted for reference. b) Radiation of OVI and Fe XVI each normalized against plasma density from the two discharge types. The arrows indicate the transition from the L- into the H-phase.

Two interesting observations should be reported, though their significance is not understood. After an H-transition, there is generally a quiescent phase much longer than the period of ELMs later in the H-phase. This indicates that it takes a time for the instability condition to develop. If, however, the transition is triggered by a sawtooth, there is generally a rapid sequence of small ELMs (see Fig. 24b). Most puzzling, however, is the observation that a sawtooth occurring during the H-phase with frequent ELMs can stop ELMs and initiate a longer ELM-free phase. Such cases are shown in Fig. 24a where ELMs are quenched by sawteeth.

To summarize, it is concluded that ELMs are MHD surface modes. The short time scales indicate that they might be ideal MHD modes. Current density distributions corresponding to H-discharge temperature profiles at the edge are expected to be unstable to current-driven (kink or tearing) modes with

a resonance surface close to the outer edge of the strong gradient region. On the other hand, ELMs could also be pressure-driven by the steep pressure gradient at the edge. Within the accuracy of the edge measurements, the pressure gradient may be steep enough to violate the ideal ballooning limit (on the assumption of shear S = 2 at the edge). At present, no distinction between these two potential driving mechanisms is possible.

2.4. Impurity development in the H-mode

As already summarized in Sect. 2.2 the development of the impurity concentration in an H-discharge depends on many aspects: the reduced wall erosion in the H-phase and the changed confinement and MHD characteristics /14, 15/. Figure 26 plots spectroscopic traces which represent the influx of oxygen and iron together with the line density and the total radiation power. Radiation and spectroscopic data are normalized to the line density to reveal the impurity influx aspect. The normalized intensities decrease after the H-transition both for oxygen and iron; the decreased impurity, influx after the H-transition is also shown by the total impurity radiation which, however, increases in the course of the H-phase to levels above the L-mode radiation (even when normalized to density). The increase in radiation is stopped when the beams are terminated. The rise in impurity radiation during the H-phase is caused by the improved confinement properties in the H-phase, which also affects impurity ions. In particular, the loss of sawteeth in the plasma centre leaves this zone susceptible to impurity accumulation. The outer zone is affected by ELMs and the impurity development in the discharge depends very much on their presence and intensity.

Figure 27 compares a discharge without ELMs with a long discharge (stacking the beams) with ELMs. Empirically it was found that ELMs can be prevented by a horizontal shift of the plasma column by 4-6 cm closer to the outer wall. In the context of this section only the different development of impurity radiation and energy content is of interest. Without ELMs impurities quickly accumulate in the plasma centre causing the total and, in particular, the central radiation to increase. Otherwise ELMs prevent or slow down this accumulation process. In the plasma centre, since sawteeth do not develop, this inward flux of impurities is not counteracted. The increased impurity radiation causes saturation in the energy content of the discharge, a roll-over in β_p, and finally a forced transition back into the L-mode when the global radiation and central radiation densities match the power input.

The development of the measured impurity radiation in the discharge was modelled in order to evaluate the transport characteristics of impurities in the H-phase. The development of the iron impurity can best be described by assuming a constant diffusion coefficient of about D = 4000 cm^2/s (L-mode: D=9000 cm^2/s) with a step-like drop to D = 2000 cm^2/s in the vicinity of the separatrix and an inward velocity which rises quadratically to the plasma edge and assumes a value of $v_{in}(a)$ = 2000 cm/s (L-mode: $v_{in}(a)$ = 2000 cm/s). The reduction of D at the separatrix is necessary to describe the steep impurity gradients there.

Because of the high-Z wall (stainless steel) and target plate (titanium) material in ASDEX, the exceptional confinement properties of the quiescent H-mode cannot be utilized for high plasma energy content. With ELMs, however, steady-state conditions can be achieved for impurities and β_p, as shown in Fig. 27b.

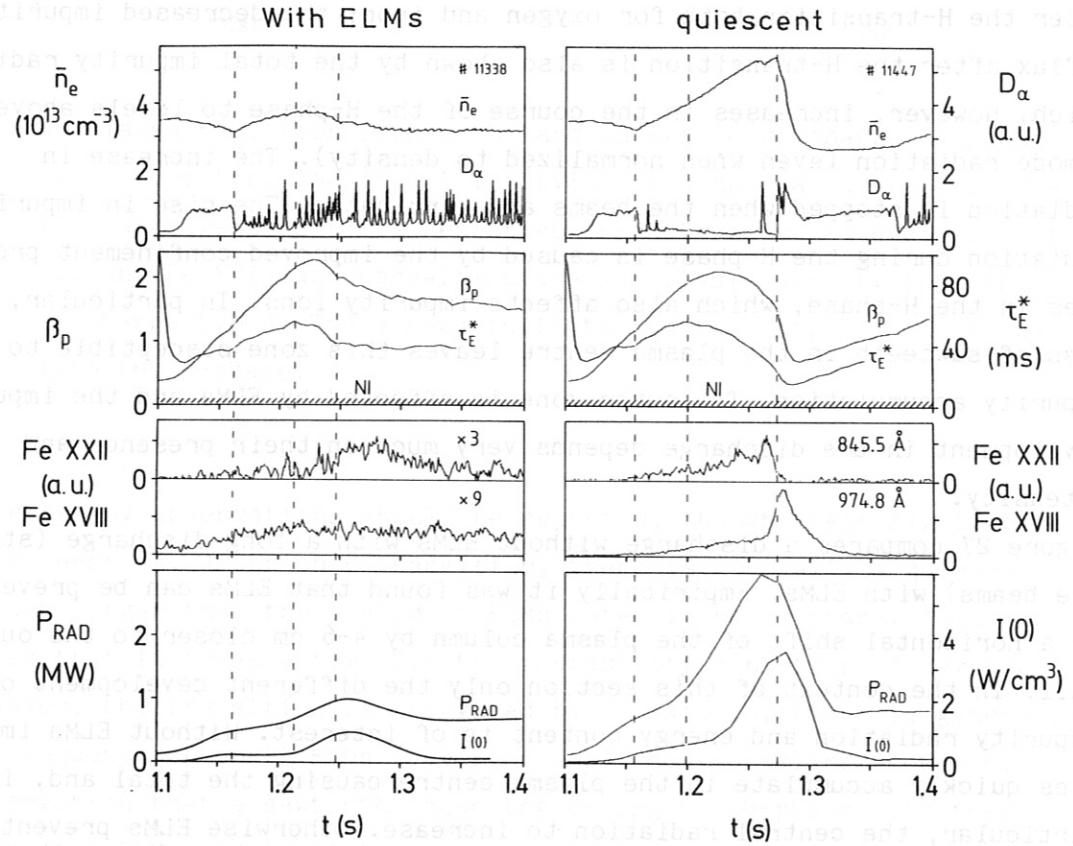

Fig. 27 Time evolution of various plasma parameters of H-mode discharges with and without ELMs (I = 0.32 MA, B_T = 2.17 T, P_{NI} = 3.3 MW, $H^0 \rightarrow D^+$): plotted are in the divertor chamber line averaged plasma density $\bar{n}_e$, D_α-light intensity, beta poloidal β_p, global energy confinement time τ^*_E; Fe XVIII and Fe XXII line intensities (representative of ion radiation from r/a ≃ 2/3 and the plasma centre), and finally total and central radiation losses P_{RAD} and I(o).

3. Confinement in the H-mode

3.1. Power fluxes in the H-mode

The power transported into the divertor chamber is the main power loss channel in the OH and L-phases in keeping with the radial anomalous heat conduction by electrons across the separatrix. The power flux into the divertor chamber splits up into radiated power via volume processes (impurity radiation and charge exchange losses) and power deposited onto the target plates. Another power loss channel is impurity radiation and charge exchange onto the walls around the main plasma. Because of the high cleanliness of divertor discharges both under ohmic and beam heating conditions, the impurity radiation power is small. The process of power transfer from the main plasma into the divertor chamber is understood in terms of classical electron heat conduction along the magnetic field lines in the s.o.l. A consistent picture exists for plasmas under ohmic and beam heating conditions in the L-regime.

The situation is totally different after the H-transition: at invariant heating power the power transported into the divertor chamber drops approximately to the ohmic level at the H-transition. This rapid and surprising reduction in power flux into the divertor chamber is plotted in Fig. 28, which shows both power radiated from and power transferred to the target plates. The reason for the sudden decrease of power fluxes into the divertor chamber is not a sudden defect of the magnetic configuration. Particles and energy are still transported onto the target plates where the separatrix is supposed to intersect it. The quality of the s.o.l. has even improved and the deposition peaks shrink, as was shown in Fig. 13. But as a consequence of the reduced power inflow the parameters of the divertor plasma (density, electron temperature, H_α-radiation) resume the ohmic values.

Also between ELMs the power fluxes into the divertor chambers are low. With ELMs the power seems to be transported into the divertor chamber in pulses. Averaged over these pulses (as with a bolometer), the radiated power within the divertor chamber is somewhat below that of the pre-transition L-phase and much above the level during a quiescent H-phase. Probably with ELMs there is no severe problem with power accountability.

A transient reduction of the power loss across the separatrix has to occur after a change in confinement. Within 2-3 confinement times, however, when the energy content of the discharge has been built up and steady-state

conditions are restored, the original power loss is established. The expected variation of the power losses into the divertor chamber are plotted in Fig. 28 for different confinement times. The measured power loss, however, remains low at the level assumed immediately after the transition. The power accountability cannot successfully be done just after the H-transition. At present we can only conclude in rather indirect ways the existence of a hidden power loss channel and we do not know the origin of this power loss or the location at which it is deposited. General possibilities are toroidal asymmetries in radiated power either in the main plasma or the divertor chamber. Because of the symmetry of the magnetic field configuration of ASDEX, such asymmetries are unlikely. The hidden losses could be along drift orbits which allow particles to cross magnetic field lines and ignore the magnetic field topology. Such a loss channel might be opened at the H-transition where even the plasma edge is collisionless, and the possibility for such losses might be closely connected to the physics prerequisites for the H-transition to occur as discussed in sect. 6.

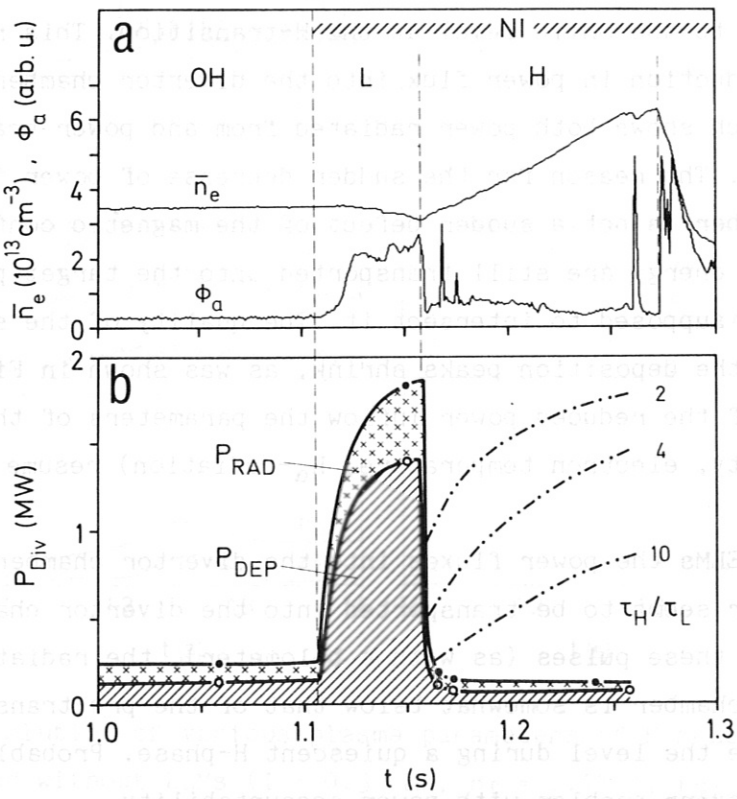

Fig. 28 (a) $\bar{n}_e$ and ϕ_a and (b) the total power flow P_{DIV} into the divertor chambers. The dashed-dotted curves show the variation of the normalized transport losses for energy confinement time changes at the H transition (I_p = 1.315 MA; P_{NI} = 3.5 MW).

3.2. Global confinement

The global confinement is in most cases determined from β_p measured by a well-compensated diamagnetic loop. The results are regularly tested for consistency with $\beta_p+l_i/2$ measured with equilibrium coils and with β_{pe} of the electrons as provided in a quasi-continuous manner by the multi-pulse Thomson scattering diagnostics. In some cases T_i-profiles are measured and full kinetic β_p determination is possible.

Figure 29 compares the τ_E-values of H-mode plasmas for 300 and 370 kA with L-mode results of 300 kA for a heating power above 2 MW (H^o injection into D^+ plasmas; H-mode with ELMs), measured either diamagnetically or via profiles /10/. At low density L-mode data are possible with the divertor configuration; for densities above $3x10^{13}$ cm^{-3} only H-mode discharges develop. In this density range a comparison of confinement times is only possible with limiter data. At the same current τ_E^H exceeds τ_E^L by a factor of 2; τ_E^H increases as the plasma current (see sect. 3.4) with the same current scaling as L-mode plasmas. Because of the scattering of the data (predominantly introduced by the irregular nature of the ELMs) a density dependence cannot be determined but a steep or even linear density dependence - as in the low-density ohmic phase - can be excluded.

Figure 29 compares the H-mode results also with ohmic data. For clarity, only smooth curves through the ohmic data points are shown. Results for various isotope compositions are plotted. The high-current H-mode results compare well with the ohmic values and the $H^o \rightarrow D^+$ data lie between the ohmic hydrogen and deuterium results. Because of the current scaling and the lack of a pronounced density dependence H-discharges are obviously not simply beam-heated plasmas with prevailing ohmic transport characteristics. The isotope dependence of ohmic and L-mode plasmas is maintained unter H-mode conditions, too.

The improved particle confinement at the H-transition is obvious from the sudden increase in density, which leads to reduced or even zero external gas consumption. The plasma is then externally fuelled by just the beams. In the quiescent H-mode the rise in the density content is higher than the beam fuelling rate; under these circumstances the plasma is refuelled with gas accumulated in the divertor chambers and the chamber walls. Figure 30 compares the line-averaged density and external gas fuelling of an L- and an H-discharge. The external gas flux is sharply increased with the initiation of the beams to counteract the density decrease that otherwise occurs during the L-phase.

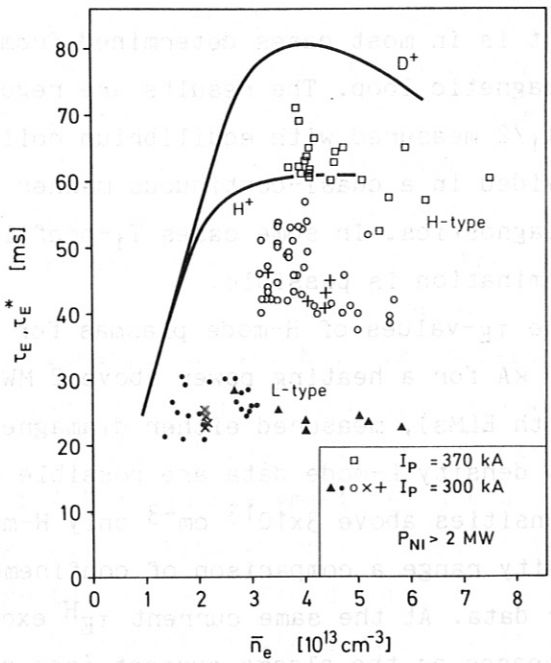

Fig. 29 Global energy confinement time versus density. The solid curves show the Ohmic relation for hydrogen and deuterium plasmas. The solid data points are L-type discharges (dots: divertor, triangles: limiter discharges); the open symbols are H-type discharges at two different currents. Crosses denote τ_E-values deduced kinetically; the other symbols are based on diamagnetic loop measurements (τ_E^*).

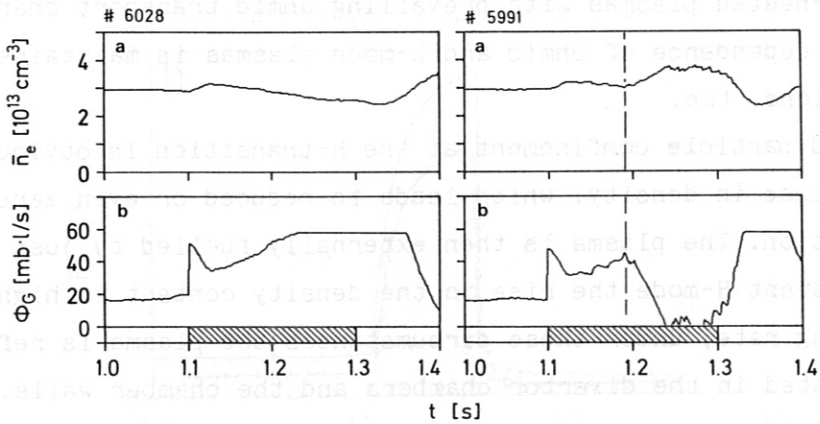

Fig. 30 Time dependence of line averaged density $\bar{n}_e$ and external gas flux ϕ_G of L-type (left column) and H-type (right column) discharges. The dashed line indicates the transition from the L- into the H-regime.

The absolute values of the particle confinement time in the different confinement regimes are difficult to assess. Particle transport will be addressed in separate sections dealing with transport analysis of the main plasma, in the boundary layer, and of impurities.
Here we just summarize the different constituents of the particle balance equation for the different confinement regimes:

$$dN/dt = -N/\tau_P + \Phi_G + \Phi_B + \Phi_R, \qquad (2)$$

with N the particle content within the separatrix, τ_P the global particle confinement time of the plasma bound by the separatrix, Φ_G the external gas flux through the valve, Φ_B the fuelling rate of the beams and Φ_R the recycling flux. In ASDEX the recycling source is the amount of neutral gas stored within the divertor chamber and its walls. The recycling flux is therefore approximated by

$$\Phi_R = N_o/\tau_D, \qquad (3)$$

with N_o being the neutral particle content of the divertor chambers and τ_D the confinement for neutral particles in the divertor chamber, which is largely determined by the conductance of the divertor throats.
Typical values for the components of equ. 2 are listed in Table 1; the quoted τ_P values have to be taken with caution but they clearly demonstrate the drastically improved particle confinement of the H-mode.

TABLE 1

	dN/dt (s^{-1})	Φ_G (s^{-1})	Φ_B [2] (s^{-1})	Φ_R [1] (s^{-1})	τ_P (s)
OH	0	10^{21}	0	$2*10^{21}$	0.05
L	0	$6*10^{21}$	$8*10^{20}$	$2*10^{21}$	0.01
H*	$2*10^{21}$	0	$8*10^{20}$	$2*10^{21}$	0.15

1) The recycling flux is not well known
2) Particle flux at 3MW

3.3. Transport analysis

Transport analysis shows that the changes in confinement, both for L and H plasmas, are due to modifications of the electron transport. Electron thermal diffusivity and the particle diffusion coefficient which is always correlated to it, increase in the L-phase and decrease after the H-transition /17, 4/. The ion heat conductivity is found to be neoclassical, irrespective of the confinement regime /17/. Figure 31 shows the radial variation of the electron thermal diffusivity as obtained from transport analysis for the ohmic-, L-, and quiescent H*-phases. Results for the quiescent H*-mode are shown to demonstrate the intrinsic heat transport characteristics undisturbed by superimposed transport contributions from ELMs. Over most of the cross-section, χ_e^{H*} is comparable to χ_e^{OH}, which, however, seems to be fortuitious because the transport properties of the OH- and H-phases are not the same. The deviation in the plasma centre of χ_e^{OH} may be caused by sawteeth, which are not present in L- and H-phases. The drop in χ_e^{H*} at the plasma periphery, which coincides with the observed edge pedestals, will be discussed later.

3.4. Scaling of τ_E in the H-mode

This section deals mainly with the dependence of the energy confinement on various parameters /18/. Where not otherwise noted, the energy confinement times are deduced from β_p measured by the diamagnetic loop and refer to

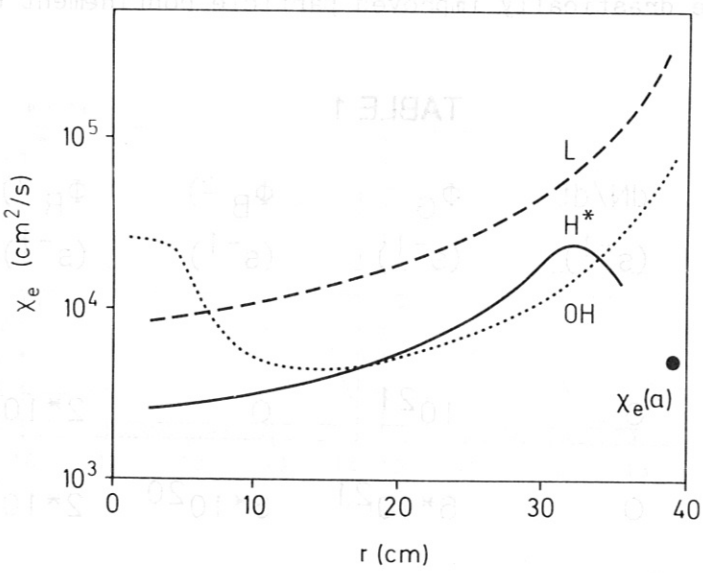

Fig. 31 Radial profiles of the electron thermal diffusivity during the Ohmic, L and quiescent H-phases; the solid circle denotes $\chi_e(a)$ deduced from the profiles of Fig. 5.

quasi-stationary states obtained by averaging over many ELMs. The agreement between confinement times obtained from magnetic measurements (τ_E*) and those calculated from measured plasma profiles (τ_E) is shown in Fig. 29. No correction due to radiation is applied, which is justified for H-discharges with a sufficient ELM frequency where the volume-integrated power losses are between 20% and 30% of the input power.

3.4.1. Density dependence

The density dependence of ohmically heated ASDEX discharges shows a linear increase of the global energy confinement time τ_E with $\bar{n}_e$ for lower densities ($\bar{n}_e \lesssim 3\times10^{13}$ cm^{-3}) and a levelling off at higher densities, which was attributed to an increasing contribution of ion heat conductivity /19/. For L-discharges as well as for neutral-beam-heated limiter discharges, however, τ_E* was found to be largely independent of the plasma density. Contrary to the ohmic case, however, the lack of $\bar{n}_e$-dependence is exclusively an electron transport property /17/.

The experimental investigation of the density dependence in H-mode discharges is hampered by the large variation in the frequency of the usually observed ELM activity which affects both particle and energy confinement. In cases where a quasi-stationary state, averaged over the ELM's, has been obtained during the injection pulse, the deduced global confinement time does not reveal a marked $\bar{n}_e$-dependence over a wide density range within the scattering of the data points (see Fig. 29). The interpretation of the non-stationary high-density H-discharges is more complicated: high densities during the limited NI pulse length are obtained only by strong gas puffing, which, in turn, leads to a higher ELM frequency and therefore tends to lower τ_E-values. At densities above 7-8x10^{13} cm^{-3}, only L-discharges seem to be possible with gas puff refuelling. The actual classification of the discharges into L or H is not always definitely possible because the density and, with it, H_α sharply increase and transitions may escape the observation. Phases without any ELMs, on the other hand, are governed by a long particle confinement time (as discussed in Sect. 3.2). To what extent τ_E of these quiescent H-phases exhibits any density dependence is still unresolved.

3.4.2. Current dependence

The important new parameter which enters the scaling of the neutral-beam-heated plasmas in ASDEX as well as in other machines /18, 20, 21/ is the plasma current I_p. The global energy confinement time τ_E was found to

increase linearly with I_p over almost the full current range accessible to ASDEX (150 kA $\leq I_p \leq$ 450 kA). This applies to L- and H-mode discharges, as shown in Fig. 32. The τ_E*-values for H-discharges are averaged over ELMs during a quasi-stationary state. At the highest plasma currents, τ_E* for an H-mode D^+-plasma is comparable to the confinement time of ohmic discharges. With ELMs, however, we generally observe the tendency of τ_E* to level off at high I_p. Unfortunately, it is not possible within the ASDEX parameter range to resolve clearly whether the above-mentioned I_p-scaling breaks down at high plasma currents when τ_E should significantly exceed the values of ohmic discharges or whether the breakdown occurs for MHD reasons because q_a is close to 2.

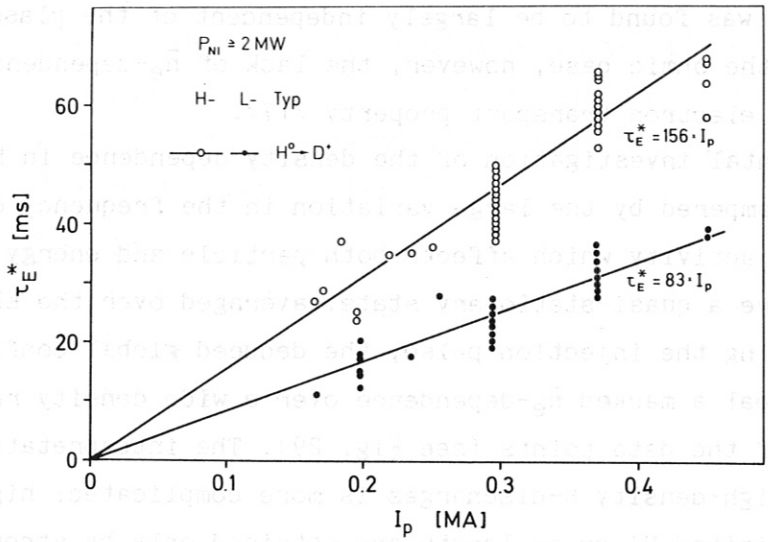

Fig. 32 Current scaling of energy confinement time for D^+-target plasmas ($H^0 \rightarrow D^+$) in L- and H-mode.

3.4.3. Power dependence

The ASDEX neutral beam system with eight ion sources is especially suitable for power scan experiments since it allows changes of heating power in fairly small steps. The power from one ion source of about 0.4 MW is comparable to the ohmic heating power. Additional heating with only one source already completely changes the electron transport. The dependence of τ_E* on the total heating power (P_{tot}) deduced from power scan experiments with H^0- and D^0-injection is illustrated in Fig. 33 in a log-log plot /18/. The values are corrected for the fast ion contribution in β_p, a correction

which is only significant for low densities. The (L-mode) results may well be described by $\tau_E^* \propto P_{tot}^w$ with $w \propto -1/3$ for heating powers of up to 3.5 MW. This finding is in qualitative agreement with the result of other experiments /20, 21/ and is confirmed by detailed transport analyses /17/. The power dependence of H-mode discharges was investigated by operating in a single-null divertor configuration. This configuration yields somewhat lower confinement values than in the double-null configuration but it reduces the power threshold for H-transition and therefore allows a scan over a wider power range. The results are also presented in Fig. 33. They demonstrate that the energy confinement in quasi-stationary H-phases is largely independent of the heating power.

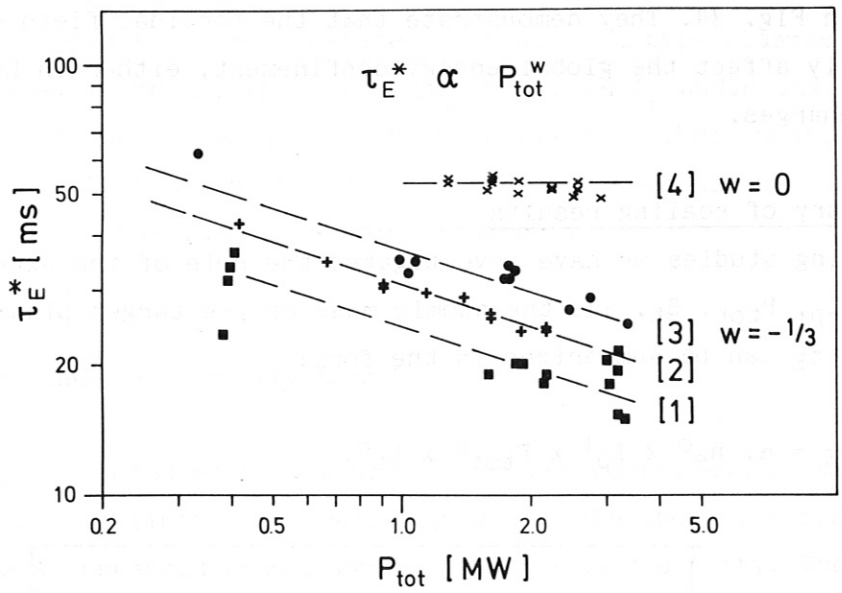

Fig. 33 Heating power scaling ($P_{tot} = P_{abs} + P_{OH}$) of energy confinement time for L- and H-mode discharges under different conditions: (1) $H^0 \rightarrow H^+$: L, 370 kA, (2.1 - 5.8) x 10^{13} cm^{-3}, (2) $H^0 \rightarrow D^+$: L, 370 kA, 1.8 x 10^{13} cm^{-3}, (3) $D^0 \rightarrow D^+$: L, 315 kA, (2.0 - 3.4) x 10^{13} cm^{-3}, (4) $H^0 \rightarrow D^+$: H, 375 kA, (4.0 - 5.0) x 10^{13} cm^{-3}.

3.4.4. Plasma species dependence

The confinement properties of neutral-beam-heated ASDEX discharges have been studied with hydrogen, deuterium and, to a smaller extent, helium target plasmas. Transitions into the H-mode were obtained in all cases, with some differences in the operational range (see Sect. 4). As in the

other confinement regimes, τ_E of deuterium is superior to that of hydrogen: τ_E^H/I_p ($D^o \rightarrow D^+$) = 0.2 ms/kA; τ_E^H/I_p($H^o \rightarrow D^+$) = 0.16 ms/kA; τ_E^H/I_p($H^o \rightarrow H^+$) = 0.08 ms/kA. Though it is primarily the ion mass which is different, the superior confinement properties of a deuterium plasma seem to be a consequence of the electron transport since electron heat losses dominate the energy balance in these discharges.

3.4.5. Toroidal field dependence

The effect of the toroidal magnetic field B_t on the confinement of neutral beam-heated ASDEX discharges was investigated in a few series of experiments where B_t was varied in the range $1.6T \leq B_t \leq 2.6$ T while all other plasma parameters were kept constant. The results of various B_t-scans are shown in Fig. 34. They demonstrate that the toroidal field does not significantly affect the global energy confinement, either in L-mode or in H-mode discharges.

3.4.6. Summary of scaling results

In the scaling studies we have investigated the role of the external parameters $\bar{n}_e$, I_p, P_{tot}, B_t, and the atomic mass of the target plasma. The scaling for τ_E can be summarized in the form:

$$\tau_E = \alpha . \; n_e^{o} \times I_p^{1} \times P_{tot}^{o} \times B_t^{o}.$$

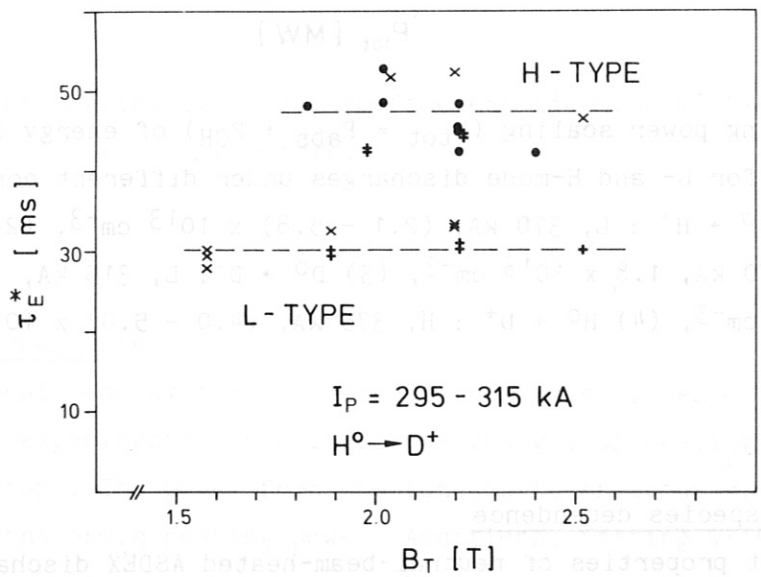

Fig. 34 Variation of energy confinement times with toroidal field for L- and H-discharges. The different symbols belong to different series of experiments.

The proportionality constant depends on isotype mass.

Generally, in the H-mode the confinement results are given by superposition of microscopic transport and energy losses through an MHD process. The scaling results presented above will partly also contain the parameter scaling of the impact of ELMs on the energy losses. It remains to be seen whether the power scaling is affected by this superposition, since ELMs are found to be more frequent at low power. The combined effect of a possible power-dependent microscopic transport, which increases with power with the MHD contribution, which decreases towards higher power, may therefore just yield a power-independent τ_E.
The scaling of τ_E in the H-mode shows a linear current dependence as in the L-mode. As this scaling is not observed in ohmic plasmas, the transport in the H-phase seems to be more related to that of L-type plasmas than ohmic discharges. We regard the dependence of τ_E on I_p under auxiliary heating conditions as a consequence of the negligible ohmic heating input. This common element of L- and H-plasmas therefore does not necessarily imply any common trends in microscopic transport.

4. Operational range of the H-mode

The H-mode can be produced over a wide parameter range, and in ASDEX it is the L-mode which is limited to small regions of the operation space. The H-mode requires a threshold beam power and a threshold density. The H-mode is achieved in hydrogen, deuterium, and helium discharges, in single-null (SN) and double-null (DN) divertor plasmas with either co- or counter injection. The power threshold depends on the plasma configuration, the species, and the NI geometry. The power threshold is 1.2 MW for SN and 1.8 MW for DN plasmas. The configurational aspects of the H-transition are considerable. The H-mode is mass easily accessible in SN operation; the possible reasons will be discussed in Sect. 6. The lowest power with which the H-transition was ever achieved in ASDEX was 0.8 MW (~twice the ohmic power input) for counter-NI in the double-null configuration. Single-null operation did not further reduce the power threshold. However, the H-mode studies with counter-NI are of a preliminary nature because the H-mode developed only for short phases of a few 10 ms and collapsed mostly owing to radiation or MHD problems.

Like the power threshold, the density threshold also depends on the configuration, whereas the SN configuration again has a larger operational range than the DN one. At I_p = 300 kA the H-mode develops in the SN configuration for $n_e > 1.7 \times 10^{13}$ and in the DN configuration for $n_e > 3 \times 10^{13}$ cm^{-3}. The critical density is further found to rise with plasma current. At high density ($n_e > 7 \times 10^{13}$ cm^{-3}) the plasma does not seem to be able to maintain the H-mode and the τ_E-values drop to those of L-discharges. A similar observation was made in PDX /22/. The upper density limit, however, has only been tested under the unfavourable conditions of strong gas puffing during short injection pulses (see also Sect. 5.3 for pellet refuelling in the H-mode).
The H-mode was achieved at all current values at which ASDEX was operated in the range $160 \leq I_p \leq 490$ kA. In particular, the high-current plasmas are of interest because $q_a = 2$ (B_t = 1.86 T). The quality of the H-phase at these low q_a-values seems to be degraded, most probably because of the large ELMs appearing at low q_a. The investigation of the low-q_a H-mode regime is not yet finished and the results are of a preliminary character.

A specific operational premise for the H-mode in ASDEX is the need for the divertor configuration. In ASDEX we never succeeded in establishing the H-mode in the limiter configuration though various limiter configurations were tested, such as poloidally closed ring limiters, poloidal arc limiters either placed on the high or low field side, mushroom limiters, or a toroidally closed belt limiter on the bottom side of the plasma. The limiter material was in all cases iron and in a second version graphite. All experiments with auxiliary limiters in ASDEX have shown that the H-mode is quenched at a separatrix limiter distance of 2.5 cm.

A specific limitation for H-mode confinement studies is the high-β stability limit. It is a disappointing result that the H-mode, with its superior confinement, seems to have the same low β-limit as the L-mode /14, 23, 24/. However, this result may be an indication that different mechanisms are responsible for the stability limit at high β on the one hand, and the gradual degradation of confinement in the L-regime already at low β on the other.

H-mode plasmas conform to the β-limit scaling $\beta_{MAX} = C \times I_p / a\, B_t$ /25/ with C=2.8 for the thermal plasma or with C=3.5 when plasma rotation and beam pressure are included. Figure 35 shows the operational space of the H-mode

in a β_t versus heating power diagram and compares it with that of the L-mode of ASDEX. The power range of the H-mode is restricted by the low power limit of 1.2 MW and the maximal NI power of 4 MW installed in ASDEX for hydrogen injection; the operation space is limited by a (not well-defined) high q_a-limit beyond which plasma studies were generally not carried out and a low q_a-limit of $q_a \approx 2$. Low-q_a and high-q_a operation limits introduce two high-β boundaries, which complete the operational space (hatched area in Fig. 35). The data points in Fig. 35 show the results of a power scan at $q_a = 3.4$ at the transition from the linear range (τ_E independent of power) up to the β-limit. At the β-limit, ASDEX discharges generally do not disrupt but the confinement degrades irreversibly during the NI pulse, causing β to drop after a maximum /26/ ending at the lower values denoted by open circles in Fig. 35.

In conclusion, the operational power range within which the intrinsic confinement properties of the H-mode can be studied is small. First, the H-mode is possible only at a power above 1.2 MW, and, because of the good confinement, a relatively low power of 3 MW brings the plasma up to the β-limit. Close to and at the β-limit, the confinement properties are additionally affected by superimposed stability effects.

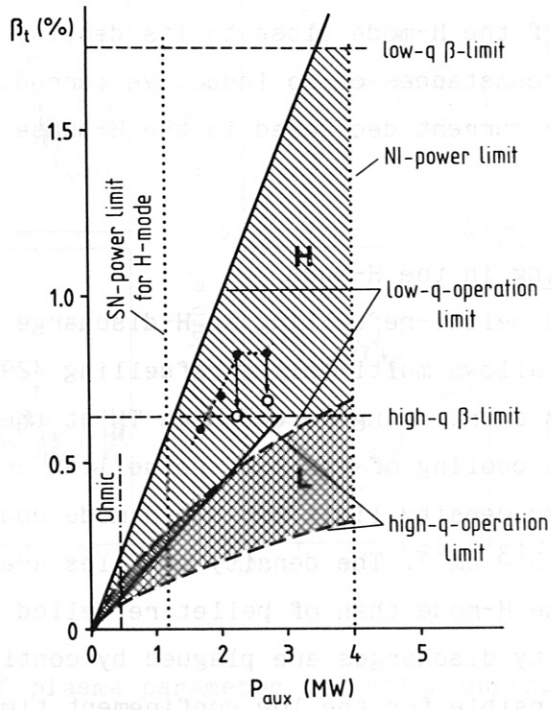

Fig. 35 Operational diagram of L- and H-phases of ASDEX. The data points are the results of a power scan up to the β-limit; the open circles denote the β-degradation observed during the NI-pulse at high power.

5. Combination of H-mode plasmas with other heating and refuelling techniques

5.1. ICRF heating

Plasmas can also be operated in the H-mode with a combination of NI and ICRF where either NI or ICRF is the major heating method. The H-mode transition is also possible with ICRF alone /27/. In ASDEX, we succeeded in causing H-mode transition in only ICRF heated plasmas with minority heating when the plasma operates basically with deuterium. In the $2\Omega_{CH}$ mode with hydrogen only, no H-mode operation was possible. The drastic changes of the s.o.l. conditions at the H-mode transition which were discussed in Sect. 2.2.2. give rise to a sudden change in the coupling conditions of the wave field onto the plasma. This technical complication invariably switched off one of the generators, with the consequence that the ICRF H-mode was transient. We are not yet able to qualify the ICRF H-mode and compare it with that of NI.

5.2. LH current drive in the H-mode

We tried to study H-mode plasmas with lower hybrid (LH) current drive. The experiments are complicated because the density limit for current drive of the 1.3 GHz LH-system of ASDEX is between 1.5 and 2×10^{13} cm^{-3} /28/, which requires operation of the H-mode close to its density limit. We achieved the H-mode under circumstances of no inductive current drive, but with the consequence that the current decreased in the H-phase owing to the increase in density.

5.3. Pellet refuelling in the H-mode

We also succeeded in pellet-refuelling an H-discharge in ASDEX by means of a centrifuge, which allows multi-pellet refuelling /29/. The penetration length of pellets is short owing to the high T_e at the edge. Nevertheless, the deleterious edge cooling of gas-puff refuelling could thereby be avoided and the upper density limit for the H-mode could be shifted from 7-8×10^{13} cm^{-3} to 1.4×10^{13} cm^{-3}. The density profiles are broad and more characteristic of the H-mode than of pellet-refuelled discharges. Pellet-refuelled high-density discharges are plagued by continuous ELMs, this probably being responsible for the low confinement time of 50 ms.

6. Physics aspects of the H-mode transition

The H-transition can be viewed as a bifurcation phenomenon in the sense that the properties of the final state (e.g. the confinement properties) are very different, while those of the intial state - the plasma parameters of a discharge just prior to the H-transition compared with those of one which remains in the L-mode - can hardly be discriminated experimentally. Figure 36 compares a few typical diagnostic traces of two consecutive discharges, the one being an L- and the following an H-discharge. Operation close to the power threshold occasionally yields L- and H-discharges at identical external parameter settings for the plasma and beam. The arrows indicate the moment of transition. The tableau of diagrams in Fig. 36 con-

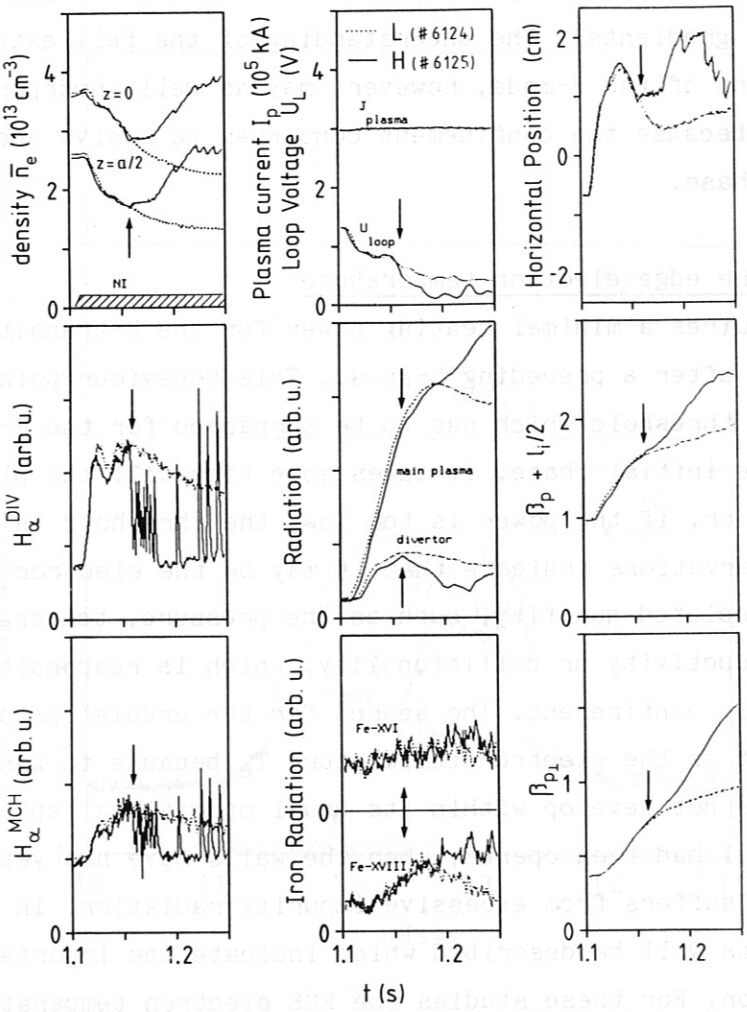

Fig. 36 Comparison of plasma parameter variation during the NI-phase of two consecutive discharges, the first being an L- and the second an H-discharge. The arrow indicates the H-transition. (H_α^{MCH}(H_α^{DIV}) = H_α-radiation in the main plasma (divertor) chamber).

tains traces which document the variation of external parameters like such as the current, density and horizontal plasma position, traces which portray the recycling conditions in the main plasma and divertor chamber, the impurity conditions (main plasma radiation, iron radiation and loop voltage) and finally the development of the energy content of the two discharges. Within the noise of the different traces, the plasma parameters at the transition are identical to those of the discharge, which remain in the L-mode throughout the pulse. This comparison shows that the search for the decisive parameter which causes the plasma to carry out the H-transition will not be easy. This search has to concentrate on the plasma conditions at the end of the L-phase. The understanding of the H-mode transition physics must concentrate on this phase and may not incorporate structural elements of the fully developed H-phase (such as the changed profiles or the steep edge gradients). The understanding of the full extent of confinement improvement of the H-mode, however, may as well incorportate these modifications because the confinement continues to evolve and to improve during the H-phase.

6.1. Role of the edge electron temperature

The plasma requires a minimal heating power for the H-transition and the H-phase develops after a preceding L-phase. This behaviour points to the existence of a threshold which has to be surpassed for the H-mode to develop. In the initial phase, it takes some time till the plasma is sufficiently heated or, if the power is too low, the threshold is not reached at all. These observations indicate that it may be the electron or ion temperature or a related quantity, such as the pressure, temperature gradient, electrical conductivity or collisionality, which is responsible for the sudden change in confinement. The search for the crucial parameters concentrated first on the electron temperature T_e because it was observed that the H-mode does not develop within its usual operational space shortly after the vessel had been opened, when the walls have not yet been cleaned and the plasma suffers from excessive impurity radiation. In the following, some experiments will be described which indicate the importance of T_e for the H-transition. For these studies the ECE electron temperature diagnostic is used since this is the only diagnostic which gives a continuous reading with sufficient time resolution. In the course of these experiments we learned that it might be the electron temperature of the plasma periphery which decides about the further confinement development /30/. For the following diagrams we therefore plot the variation of T_e at the outermost

channel located at -31 cm in the mid-plane on the high-field side, where measurement is possible with ECE. Owing to the horizontal plasma shift during the discharge, the measuring point is about 7-8 cm away from the inner separatrix.

6.1.1. Addition of impurities

By introducing artificial impurities their detrimental effect on the development of the H-transition has been studied in detail. Figure 37 compares two cases where methane was puffed into the discharge: in one case (solid curve) at the beginning of the NI pulse, in the other case (dashed curve) during the H-phase. Methane, puffed in at the beginning, keeps the edge electron temperature low and prolongs the L-phase. When the impurity pulse

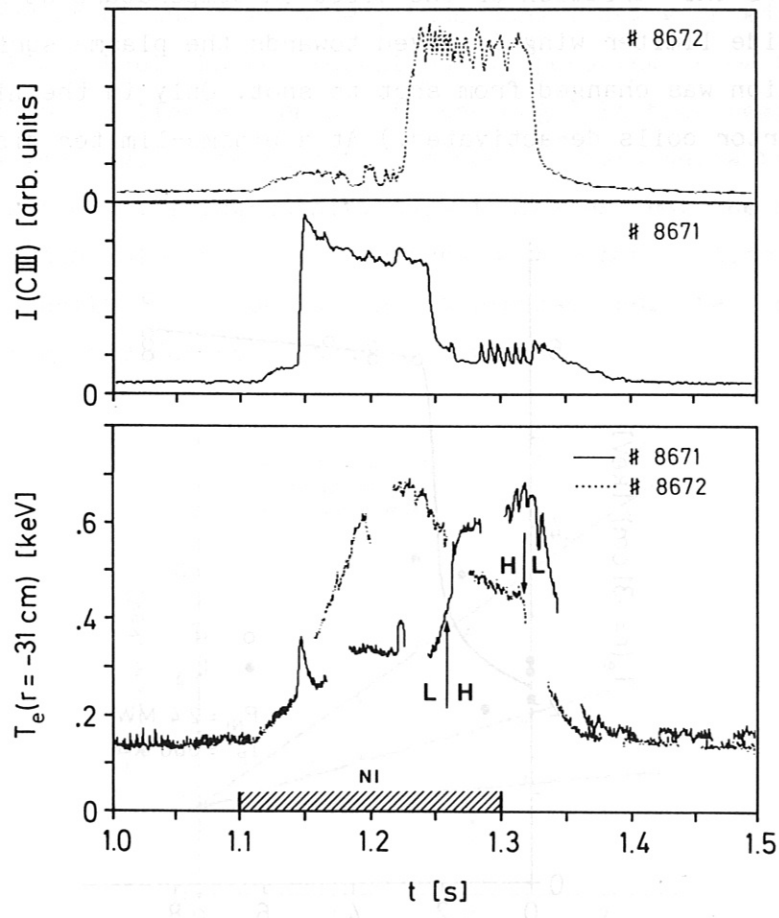

Fig. 37 CIII line radiation and edge electron temperature T_e of two discharges into which methane was puffed in during the NI-phase from 1.14 - 1.24 s (#8671) and 1.22 - 1.32 s (#8672), respectively. The impurity radiation cools the plasma edge and affects the L-H transition. I_p = 0.38 MA, $\bar{n}_e$ = 4 x 10^{13} cm^{-3}, P_{NI} = 3.0 MW.

is switched off, T_e rises and the transition into the H-phase occurs. By contrast, CH_4 puffed into the H-phase reduces the edge temperature and at about the same T_e-value the L-transition occurs. (Without CH_4 puff the transition occurs 30 ms later at about the same temperature.) In comparison with CH_4, smaller amounts of neon (high Z) are sufficient to suppress the H-mode.

With these results in mind, it is tempting to correlate the prevention of the H-mode in limiter discharges to excessive impurity cooling at the edge.

6.1.2. T_e-development in limiter discharges

Different limiter configurations have been investigated, as summarized in the previous chapter. All limiter discharges showed deteriorated energy confinement even in the parameter range of H-type discharges.

Figure 38 shows the variation of the electron temperature at r = -31 cm, when the outside limiter wing is moved towards the plasma surface. (The limiter position was changed from shot to shot. Only in the ΔR_L=0 shots were the divertor coils de-activated.) At a plasma-limiter distance

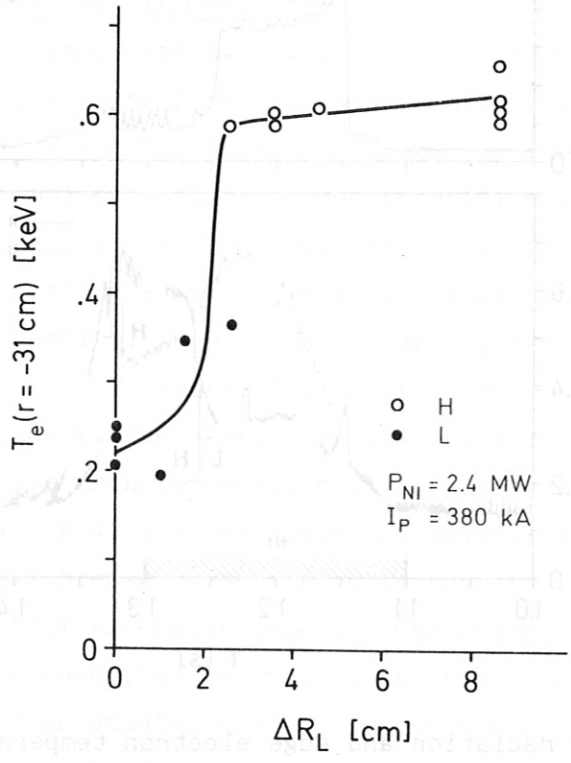

Fig. 38 Variation of the edge electron temperature T_e when the outside poloidal limiter wing is moved to the plasma surface. The ∇R_L = 0 data points are obtained from limiter discharges without energized divertor coils.

$\Delta R_L \leq 2.5$ cm (roughly one to two density or temperature fall-off lengths in the s.o.l.), the edge temperature sharply decreases and the H-regime is suppressed. The edge temperatures are a factor of about 3 lower in limiter discharges than in H-discharges. These results are also supported by Thomson scattering measurements at the edge and a similar decrease is observed for the edge ion temperature.

Figure 39 compares the variation of the edge electron temperature (r = -31 cm) with beam power in limiter discharges with that in L- and H-type divertor discharges. A linear increase with P_{NI} is observed for L- and H-discharges, while limiter discharges show a very weak dependence. The comparison indicates that the divertor configuration allows the edge temperature to evolve without constraints. In limiter discharges, however, a mechanism seems to exist (e.g. impurity erosion from the limiter with a yield increasing with beam power) which keeps the edge electron temperature largely independent of the beam power, thus constituting an additional boundary condition. L-discharges (obtained by operating below the density limit) also exhibit a linear increase in the edge electron temperature, but even at the maximal available injection power T_e stays below the threshold for the H-transition. The low-density case indicates that the H-mode might ultimately be accessible, too, but requires higher power. Also the difference in density limits of DN and SN plasmas indicates that the critical densities may depend on heating power.

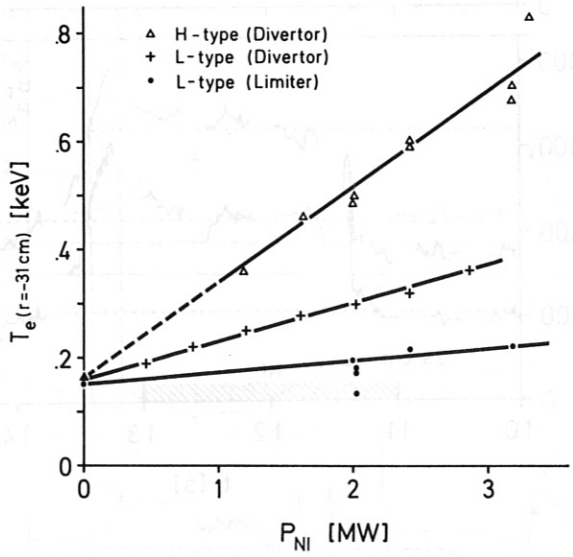

Fig. 39 Variation of edge electron temperature T_e with beam power P_{NI} in limiter, L- and H-type discharges. I_p = 0.38 MA; $\bar{n}_e \simeq 3 \times 10^{13}$ cm^{-3} (H), $\bar{n}_e \leq 2 \times 10^{13}$ cm^{-3} (L) and $\bar{n}_e \simeq 5 \times 10^{13}$ cm^{-3} (limiter).

6.1.3. Post-beam pulse H-phase

An interesting technique to unravel the crucial parameters for the H-transition is to heat the plasma with a power just below the power limit. Operating under such marginal conditions increases the sensitivity because already small parameter changes which do not affect the global plasma conditions in a complicated and involved way will enter into the transition conditions. This technique has been successfully applied in different investigations.

It is a common observation in beam-heated plasmas that the electron temperature rises once more when the beams are switched off /31/. In the short phase following the beam pulse when the orbiting beam ions still heat the plasma (slowing-down time ~15 ms) the heating per particle is suddenly improved when the flux of cold electrons injected with the beam atoms is

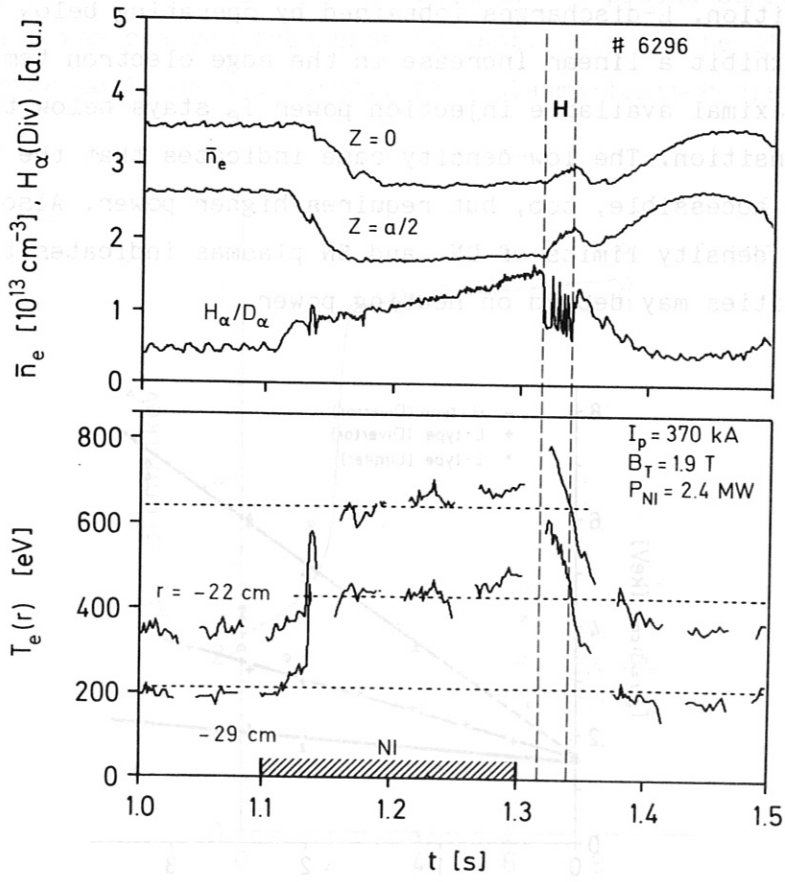

Fig. 40 Line density $\bar{n}_e$ through the plasma centre (z = 0) and along the z = a/2 chord, H_α/D_α radiation in the divertor chamber, and electron temperature T_e at two radial positions. The H-phase (between dashed lines) occurs after the NI pulse during a phase of elevated temperature.

suddenly terminated. This phenomenon has been dubbed "post-beam pulse electron temperature rise" /31/. Figure 40 shows such a case with medium heating power where the H-phase develops shortly after the beam pulse has been switched off. Confinement during the beam pulse is of the L-type. The H-phase is short because there is no auxiliary heating power but it is long enough to be interrupted by a few ELMs.

6.1.4. Comparison of L→H and H→L transitions

Because of the confinement sequence OH-L-H-L-OH the plasma properties can be compared at the L→H transition in the initial beam phase with the H→L transition after the beams have been switched off. The comparison is only meaningful when the conditions for the two transitions are rather transparentwith a longer L-phase preceding the H-transition and with an H→L transition not disturbed by ELMs. Such a case is shown in Fig. 41. The second L-transition occurs 40 ms after the beam pulse in a phase where the plasma is cooling down. As indicated in Fig. 41, the transition back into the L-phase occurs roughly at the same peripheral electron temperature as the transition into the H-phase. All other plasma parameters and also the plasma profiles are widely different at these two moments. This observation indicates that it could be specifically the edge electron temperature which has to surpass a certain threshold for the H-transition to occur.

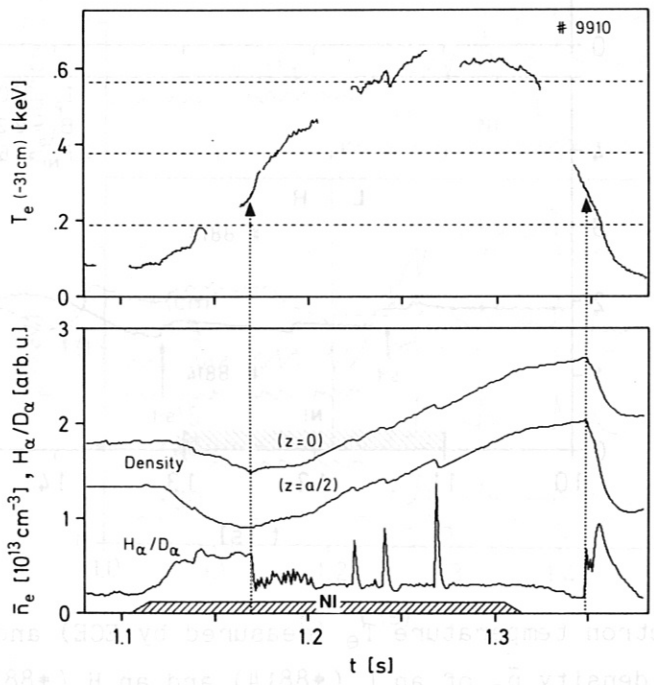

Fig. 41 Peripheral electron temperature, line averaged density along two chords and H_α/D_α-radiation in the divertor chamber during NI; the L → H and H → L transitions are indicated by arrows.

6.1.5. Sawteeth as H-mode trigger

An interesting feature of the H-transition is that it can be initiated by a sawtooth crash. In Sect. 2.3. we pointed out that it is irrelevant for the H-transition whether q(0) is above or below 1. The triggering of the H-mode by a sawtooth occurs when the thermal wave of a sawtooth arrives at the plasma edge. The observation of this trigger mechanism, which was also made by others /5/, is the most convincing evidence of the role of T_e at the plasma periphery (or of a parameter depending on it) for the H-transition. Generally the transition to the H-mode occurs during non-stationary plasma conditions, when the edge electron temperature is still increasing. At high plasma current and low injection power, the H-transition can be triggered by a sawtooth. Such a case is shown in Fig. 42 in comparison with an L-type

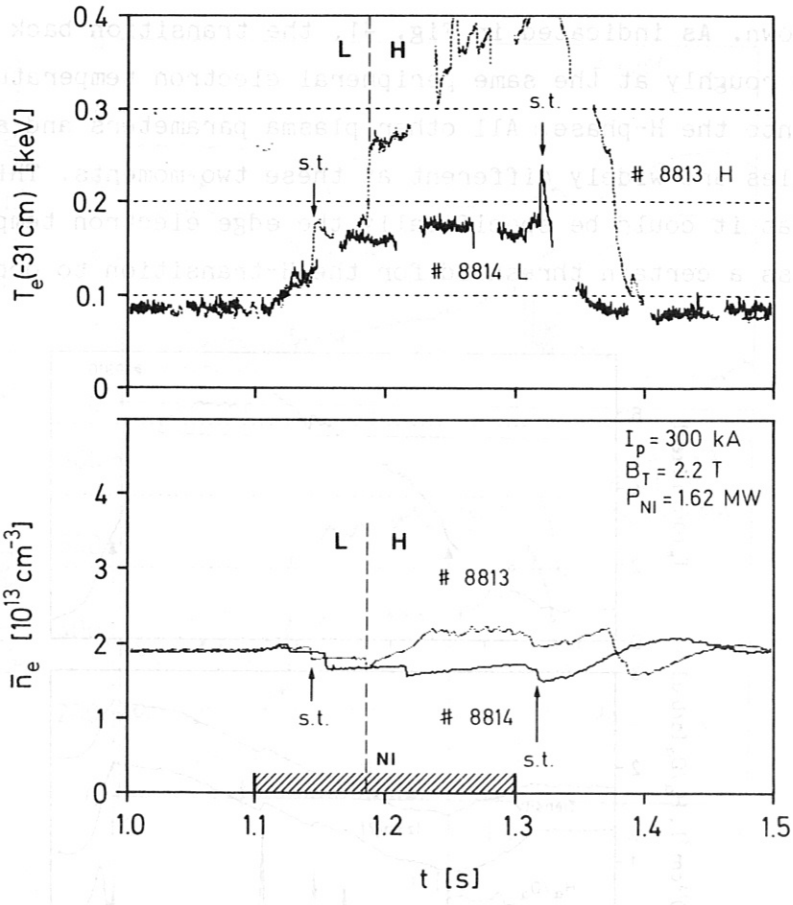

Fig. 42 Edge electron temperature T_e (measured by ECE) and line averaged electron density $\bar{n}_e$ of an L (#8814) and an H (#8813) discharge. Some sawteeth (st) are indicated by an arrow. The L-H transition is triggered by a sawtooth. (The ECE signals are periodically interrupted by a chopper to monitor the base-line.)

discharge. (The only difference between the two discharges is the vertical shift: the H-discharge was an upper, the L-discharge a lower single-null shot.) Figure 42 shows the edge temperature and variation of the line density $\bar{n}_e$ during the NI pulse for the two cases. Sawteeth disruptions appear as sharp drops in the density signal. As shown in Fig. 42 (arrows), the heat wave of a sawtooth increases T_e at the periphery but after its passages T_e relaxes again.

The sawtooth which causes the H-transition also increases the temperature at the edge but then the temperature does not decrease as in the case of a normal sawtooth. The temperature stays at the high level and, in the course of the H-phase, further increases as a consequence of the improved confinement. The heat pulse is dissipated in the plasma periphery. Indeed, the sawtooth that triggers the H-transition usually does not give rise to a thermal or particle pulse at the neutralizer plate, as it is the case for a normal sawtooth. This case is shown in Fig. 43. It plots the line-averaged density $\bar{n}_e$, the H_α-radiation in the divertor chamber and the electron

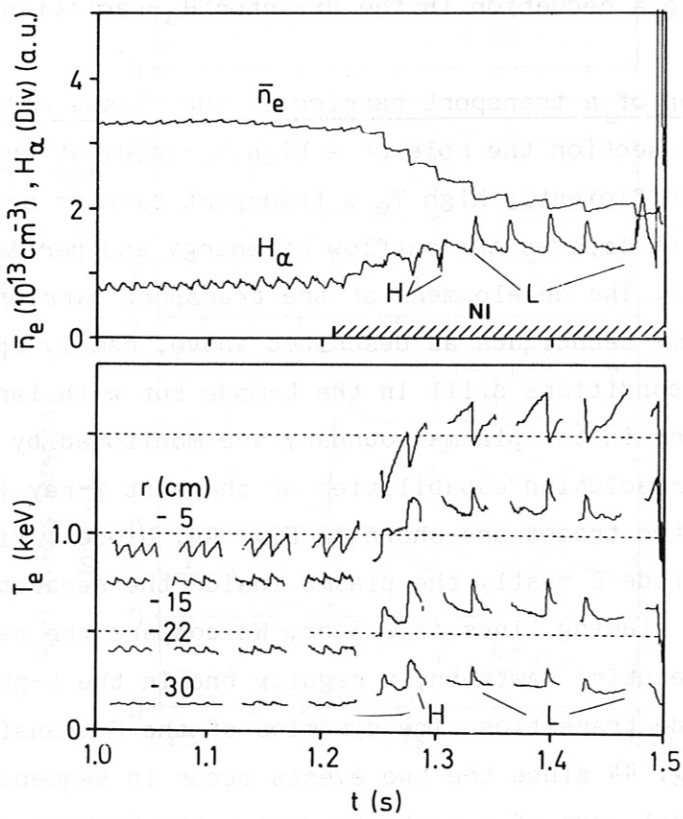

Fig. 43 Line averaged density $\bar{n}_e$, H_α-radiation in the divertor chamber and ECE-electron temperature T_e during an L-discharge with large sawteeth. Two sawteeth give rise to a short H-phase.

temperature T_e at four different radii of an L-discharge with large sawteeth and a heating power close to the power threshold. The sawteeth modulate T_e in the known form of a reduction within the q=1 surface and pulse-like variation outside it, caused by the thermal wave travelling to the plasma surface. The plasma density is modulated in a similar way. Sawteeth also modulate the H_α-signal in the divertor chamber, causing a signal rise there which is very conspicuous during the beam heating phase. Two exceptions to this behaviour are shown in Fig. 43. These are large sawteeth (only one is documented by the T_e-diagnostic), which cause an H-transition. The comparison of the parameter variation caused by a sawtooth in the L-phase with that of a sawtooth triggering the H-phase reveals a distinct difference in the outer plasma zones but rather similar behaviour in the plasma core: A regular sawtooth gives rise to a fast pulse-like temperature variation in the plasma periphery; the energy pulse travels across the separatrix, along the scrape-off layer into the divertor chamber and causes the H_α-radiation to increase there. A sawtooth correlated with an H-transition gives rise to a slow decay of the temperature in the plasma periphery and to a reduction in the divertor H_α-radiation.

6.2. Formation of a transport barrier at the plasma edge

In the previous section the role of a high T_e-value at the plasma edge was discussed. At sufficiently high T_e a transport barrier develops at the plasma edge which impedes the outflow of energy and particles and initiates the H-phase /32/. The development of the transport barrier is studied by applying the same techniques as described above, namely operating under marginal power conditions still in the L-mode but with large sawteeth. The parameter changes in the plasma boundary are monitored by using the high time and space resolution capabilities of the soft X-ray (SX) diode array. As an example, two traces are shown in Fig. 44. Diode 1 views the scrape-off layer and diode 2 mostly the plasma inside the separatrix. The distance between the two viewing lines is 2.5 cm. We compare the parameter changes due to two consecutive sawteeth, a regular one in the L-phase and one causing an H-mode transition. The dynamics of the H-transition becomes evident from Fig. 44 since the two events occur in sequence and only 50 ms apart. The thermal wave of a sawtooth during the L-phase (sthL) causes T_e to increase first in the main plasma periphery, subsequently in the s.o.l., where the T_e-variation modulates the SX signal. This signal variation cause by a sawtooth is well known.

The large sawtooth (sthH), which triggers an H-phase transition, gives rise

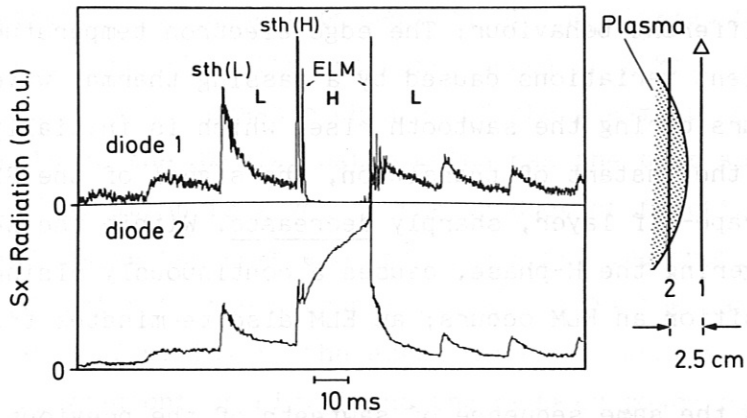

Fig. 44 Soft X-ray radiation during the L-phase with large sawteeth. Diode 1 views the scrape-off layer, diode 2 mostly the plasma within the separatrix. One sawtooth sth(H) gives rise to a transient H-phase.

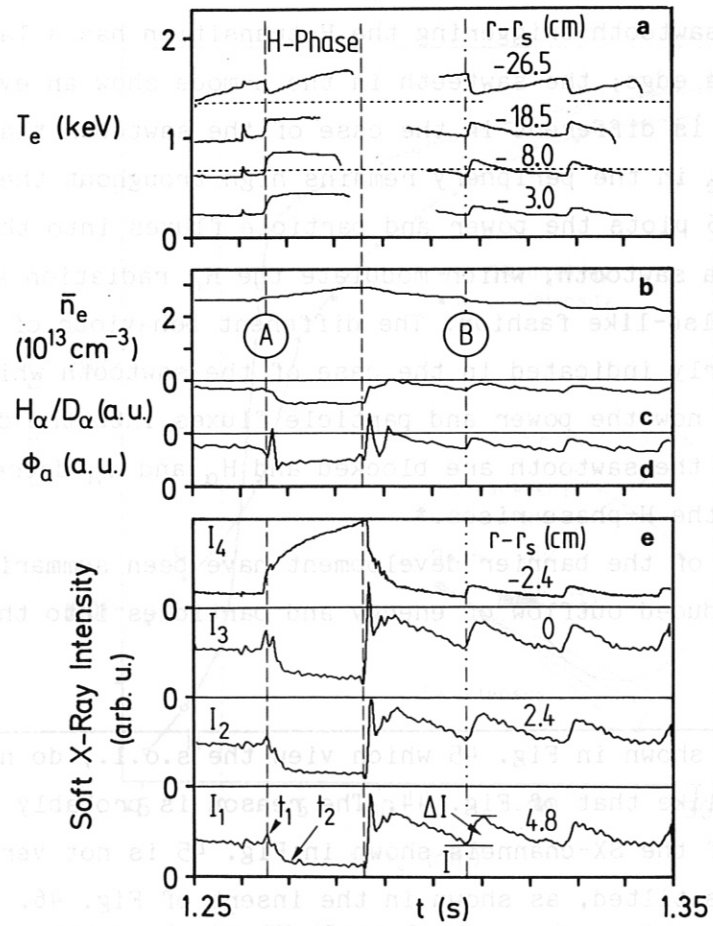

Fig. 45 Time evolution of the ECE electron temperature T_e (measured by electron cyclotron emission), (b) line averaged density $\bar{n}_e$, (c) D_α radiation in the divertor, (d) backreflected flux ϕ_a from the neutralizer plate, and (e) four SX traces from the plasma edge. (The ECE traces are interrupted by a chopper).

to a totally different behaviour: The edge electron temperature does not show the transient variations caused by a passing thermal wave. The transition occurs during the sawtooth rise, which is initially still resolvable. At the instant of transition, the signal of the SX diode, viewing the scrape-off layer, sharply decreases. Within the separatrix, the sawtooth, triggering the H-phase, causes a continuously rising signal. Just after the transition an ELM occurs; an ELM also terminates the short H-phase.

Figure 45 shows the same sequence of sawteeth of the previous figure in the L-phase and the one that triggers an H-transition. In addition, more SX-ray channels are plotted. The electron temperature in the main plasma for 4 radial positions, the line-averaged density $\bar{n}_e$, the H_α radiation in the divertor chamber, and the atomic flux Φ_a emerging from the target plate are additionally given. Supplementing the information of Fig. 44, Fig. 45 shows that the sawtooth triggering the H-transition has a large T_e-amplitude at the edge; the sawteeth in the L-mode show an evanescent behaviour which is different in the case of the sawtooth that triggers the H-mode, where T_e in the periphery remains high troughout the H-phase. In addition Fig. 45 plots the power and particle fluxes into the divertor chamber due to a sawtooth, which modulate the H_α radiation and the atomic flux Φ_a in a pulse-like fashion. The different behaviour of these divertor signals is clearly indicated in the case of the sawtooth which triggers the H-phase because now the power and particle fluxes into the divertor chamber associated with the sawtooth are blocked and H_α and Φ_a decrease. The density during the H-phase rises.*

The consequence of the barrier development have been summarized above: It leads to the reduced outflow of energy and particles into the divertor

---

* The SX-traces shown in Fig. 45 which view the s.o.l., do not go to zero in the H-phase like that of Fig. 44. The reason is probably that the viewing angle of the SX-channels shown in Fig. 45 is not vertical as in Figs. 45, but is tilted, as shown in the insert of Fig. 46. The advantage of this viewing geometry is that the actual position of the separatrix at the tangent point - obtained from equilibrium calculations - is known with a higher accuracy (~0.5 cm instead of ~1 cm in the midplane). But these channels view the lower X-point of the outer separatrix (the results of Figs. 44 and 45 are obtained in an SN configuration), where some radiation still seems to be emitted.

chamber, the improved confinement properties of the plasma, the steep gradients at the plasma edge with the consequence of ELMs.
Figure 46 demonstrates the drastic changes of the plasma profile at the edge with the help of the SX-diagnostic which has the best spatial resolution. The SX-ray radiation is given by the product of functions of n_e and T_e which also determine the edge electron pressure. The profiles of Fig. 46 are obtained just prior to the H-transition and 50 ms thereafter.
The electron heat diffusivity in the edge transport barrier is calculated from the steep T_e gradient of Fig. 5 and the reduced power outflux to $\chi_e = 5 \times 10^3$ cm^2/s and plotted in Fig. 31 together with χ_e as obtained from the transport analysis. The edge χ_e-value is comparable to the neoclassical ion heat conductivity but is still far above the neoclassical value for the electrons.

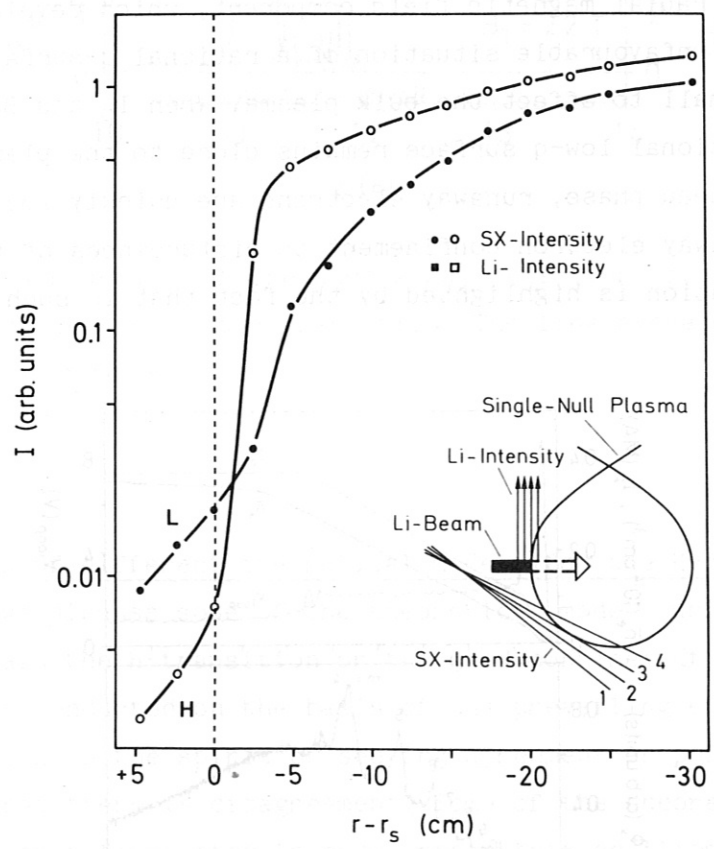

Fig. 46 Radial profiles of the SX (2-µm Be filter) in the L phase prior to the H transition and shortly afterwards Δt = 20 ms. I_p = 375 kA, B_T = 2.2 T, $\bar{n}_e = 3.3 \times 10^{13}$ cm^{-3}, P_{NI} = 0.8 MW. The inset depicts the observation geometry.

6.3. Study of runaway electron confinement to explore the nature of microscopic turbulence

The confinement of runaway electrons depends sensitively on the quality of the magnetic configuration. They are measured via the hard X-radiation Φ_X which is emitted from a molybdenum target hit by runaway electrons. The target is placed outside the plasma in the midplane on the low-field side. Runaway electrons are produced in ASDEX during the first 50 ms in the discharge breakdown phase; they are accelerated during the current ramp phase and gradually lost during the plateau phase defining a confinement time τ_R from the exponential variation of Φ_X. The increase of Φ_X indicates increased runaway electron losses.

Figure 47 plots the variation of Φ_X during the current ramp phase. The transit of rational q-surfaces across the separatrix leads to increased runaway electron losses because the magnetic configuration is somewhat disturbed. The radial magnetic field component, which develops at the configurationally unfavourable situation of a rational q-surface at the plasma edge, is too small to affect the bulk plasma. When I_p and B_t are chosen such that a rational low-q surface remains close to the plasma surface during the plateau phase, runaway electrons are quickly lost. The sensitivity of the runaway electron confinement to disturbances of the magnetic field configuration is highlighted by the fact that in such a case the

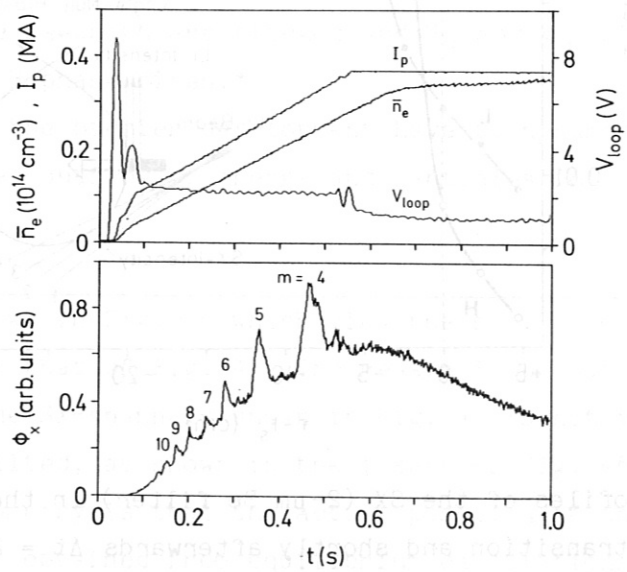

Fig. 47 Variation of the hard X-ray radiation ϕ_x during the initial discharge phase when the current is ramped up and rational q-surfaces cross the plasma surface.

sawteeth strongly couple to the runaway electron population, leading to strong sawtooth modulation of Φ_X.

The confinement of runaway electrons is sharply degraded with auxiliary heating. At the H-transition, however, the confinement of runaway electrons is again improved. The increase of Φ_X in the L-mode and the sudden reduction at the H-transition is plotted in Fig. 48 together with the line-averaged density. According to Fig. 48 the L-phase is a state of high magnetic turbulence, while the H-transition again leads to a quiescent phase.

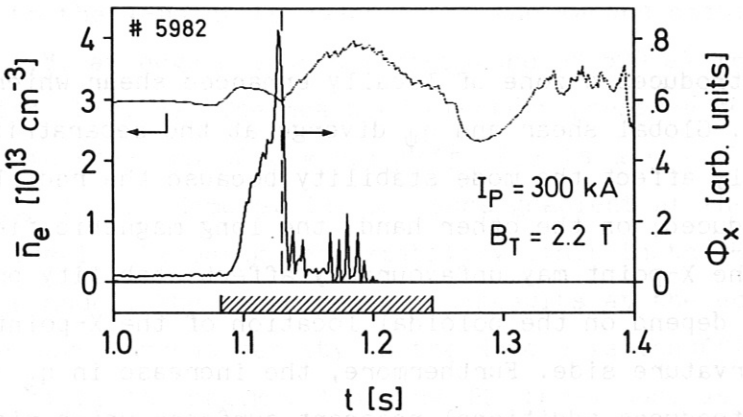

Fig. 48 The time dependence of the hard X-ray radiation with neutral injection and the L to H transition. The line averaged density is given as a reference.

6.4. Discussion of different theoretical models for the H-mode

In this section we discuss some of the theoretical models which have been proposed to explain the H-transition or the good confinement in the H-mode. The discussion is conducted on the basis of the prevailing experimental material from ASDEX in the spirit of seeking agreement or pointing out where we think that there is disagreement. Some of the theoretical investigations are made as a first step in model separatrix equilibria, which might complicate the direct comparison with the experimental data. As we are not able in all cases to use the same experimental results which we put forward to demonstrate a contradiction to confirm alternatively another hypothesis, we feel that the foundation of our argumentation is still rather weak. As the H-mode is initiated at the plasma periphery, edge measurements of high credibility are required. But precise edge diagnostics

is a difficult task. The conclusions from the different pros and cons therefore still have to be taken with caution and are far from being final.

Most of the theoretical efforts deal with the effects of the separatrix configuration on the stability conditions of modes which have the potential to cause the enhanced transport in the L-mode. It is unclear at present whether all these considerations are futile, in view of the H-mode achieved with JFT-2M in a limiter configuration, or whether the same theoretical concepts still hold in a modified form with elongated limiter plasmas under high-β_p conditions.

The X-point introduces a zone of locally enhanced shear which could affect mode stability. Global shear and q_ψ diverge at the separatrix. High shear could positively affect the mode stability because the radial scale length of modes is reduced; on the other hand, the long magnetic field length in proximity of the X-point may unfavourably affect stability properties in a way which will depend on the poloidal location of the X-point with respect to the good curvature side. Furthermore, the increase in q_ψ toward the plasma edge introduces additional resonant surfaces which might broaden the spectrum of macroscopic MHD modes in the plasma.
If the separatrix indeed exerts an overall stabilizing effect, the pressure gradients at the edge could be increased in the way that is observed experimentally. This leads to high edge temperatures which, in a second step, could directly affect resistive modes or change the turbulence level in the bulk plasma by shifting the driving gradients into the edge region. One could therefore construct a scenario where the transition into the H-phase is the trigger for the stabilizing effect of the separatrix: it moves the destablizing gradients into the edge zone so that transport is reduced in the bulk plasma and more effective use is made of the plasma volume.

6.4.1. Possible explanations for the edge barrier

In Ref. 33 the stability conditions of ideal ballooning modes are investigated in the presence of a separatrix. It is shown that shear does not favourably affect their stability, while the long magnetic field lengths at the X-point, where B_p vanishes, have a destabilizing effect to an extent which depends on the poloidal location of the X-point. Its position in the midplane on the high-field side (at the good curvature side) is the most favourable one; the worst location is the opposite one in the outside midplane. In Ref. 34 it is shown that in this unfavourable situation close to

the X-point interchange modes reach the critical pressure gradients before the ideal ballooning modes do. No difference is expected for plasmas with the X-point located either up or down the way as in ASDEX single-null discharges.

The stability conditions of ideal ballooning modes change when a finite current density is allowed at the separatrix, as demonstrated in Ref. 34. In this case the first and second stability regimes merge in a radial region close to the X-point and the pressure gradient is no longer limited by ideal ballooning modes. The required current density is parameterized in the form of $\Lambda = rV_l/2\pi RB_p\eta$ (η= electrical resistivity), which has to be above 0.7 close to the λ-point to reach there the second stability regime. Assuming $Z_{eff} = 1.8$, an edge electron temperature of 500 eV is required (see for comparison Fig. 5). The measured electron pressure gradient at the edge (normalized in the form of $\alpha = -2\mu_o Rq^2 p'/B_t^2$) is $\alpha = 0.07$ in the L-mode and $\alpha = 0.35$ in the H-mode. The pressure gradient at the edge could be close to the ideal ballooning mode stability limit in the H-mode (but is far away in the L-mode). The experimental T_e-results at the edge do not exclude that the edge current density in the H-mode is insufficiently to reach the second stability regime. Also the MHD behaviour, as described in Sect. 2.3, indicates a broadening of the current density profile after the H-transition when the m=1 activity slowly disappears (see Fig. 18). Nevertheless, the triggering of the H-mode according to the model of Ref. 34 requires the development of current density at the edge in the course of the preceding L-mode to suddenly establish the second stability regime and the transition into the H-mode. The measurements in the L-mode do not support this. It is also not indicated by the edge measurements that ideal ballooning modes are destabilized at the edge in the L-phase. It is also not clear whether the change in current density profile can happen fast enough in the case of a sawtooth-initiated H-transition. Experiments on ASDEX were specifically done to study the effect of current profile change on the H-mode.

Figure 49 shows the plasma current which was ramped up and down in the H-phase, the line-averaged density, and H_α in the divertor chamber to monitor the confinement regimes. When current is added to the edge, the H-mode is suddenly quenched; in the opposite case, when current is removed from the edge, the H-mode appears again. Under steady-state conditions the H-mode can be maintained at a current level well above the critical one of Fig. 49, indicating that the results of Fig. 49 are not caused by a current

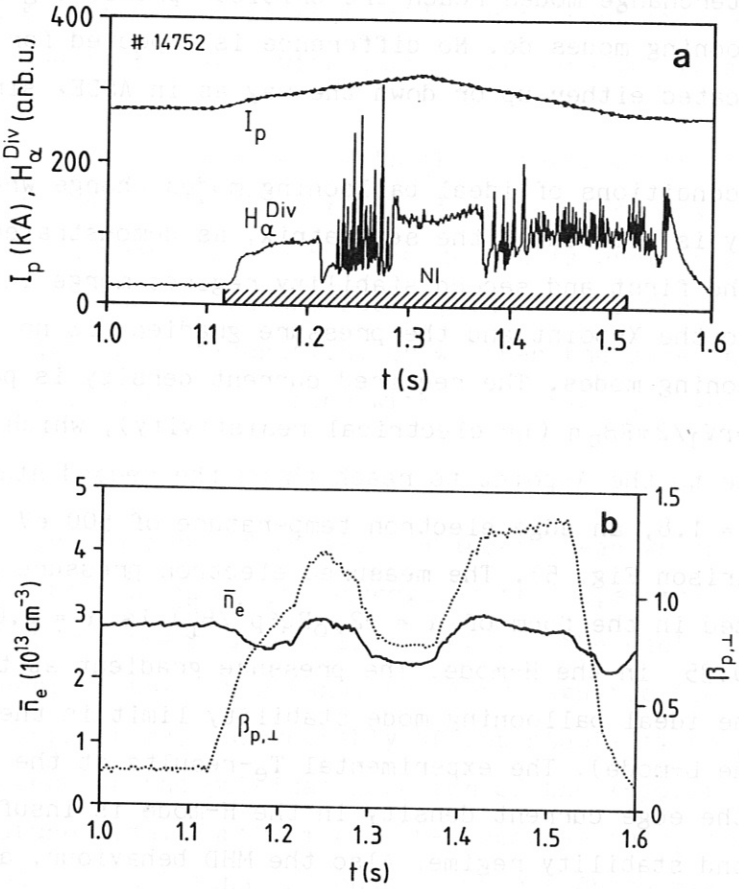

Fig. 49 Forced L to H and H to L transitions by current ramp and decay; density and β_p are plotted as reference; the H_α-radiation in the divertor chamber indicates the regime transitions.

limit for the development of the H-mode. Though the interpretation of dynamic experiments as shown in Fig. 49 is not unambiguous, the result does not confirm a possible favourable effect of edge current density on the development of the H-mode.

In Ref. 35 the effect of the separatrix on resistive kink modes is investigated. These modes are stabilized by sufficiently large shear and, in particular, it is shown in Ref. 35 that those modes are stabilized whose resonant surfaces are localized within the increased shear region inside the separatrix. The conclusion from this work is that the improvement of the MHD stability conditions due to the broad current density profile in the H-mode (no sawteeth, low j-gradient at the q=2 surface) is not paid for by intensified resistive kink mode activity in the edge region.

The stability of resistive pressure gradient driven turbulence in the separatrix vicinity is also investigated in Ref. 35 . It is noted that in the L-mode the edge parameters are such that this type of turbulence could be present. The growth rate of the resistive ballooning mode is not affected by enhanced shear or increased q_ψ, but the saturation level of the turbulence is reduced and with it the energy transport coefficient. It is further commented in Ref. 35 that the stabilization of resistive pressure gradient driven turbulence is in agreement with the notion of a transport barrier at the edge and with the observation in ASDEX of improved runaway electron confinement in the H-mode. The ratio of the electron heat diffusivity caused by resistive ballooning modes with and without the separatrix stabilization is given in Ref. 35. From this ratio χ_e is determined in the edge region of the H-mode from the radial dependence of χ_e in the periphery of an L-mode plasma (as determined from transport calculation and given in Fig. 31), but starting at the level of the H-mode χ_e at 30 cm. It is assumed that the reduction of χ_e inside 30 cm is due to processes not directly caused by the separatrix configuration.

Another topic studied in Ref. 35 is the stability of rippling modes causing resistivity gradient driven turbulence. It is observed that this mode is stabilized at the high electron temperature developed in the H-mode at the plasma periphery.

6.4.2. Possible mechanisms linking the bulk transport to the edge conditions in the H-phase

Transport analysis indicates that the overall improvement of the good confinement in the H-mode may consist of a sudden jump correlated with the development of the edge barrier and a gradual improvement thereafter along a slower time scale determined by diffusive processes along which profiles can be changed. The obvious freedom under H-mode conditions to move the steep pressure, particle and current density gradients into the immediate edge zone, thereby reducing the free energy in the bulk plasma, may improve the transport conditions there. The specific edge structure in the H-mode may allow a class of plasma profiles with better confinement aspects.
The change in the current density profile is obvious in the H-mode because of the high edge electron temperature: the electrical conductivity in the plasma periphery in the H-mode is about the same as it is in the plasma centre during the OH-phase. Improved MHD stability in the bulk plasma is indeed observed in the H-mode because the m=1-mode and sawteeth disappear without being replaced by m=2-mode activity. A specific mechanism to

broaden the current density profile is proposed in Ref. 36. The steep ion pressure gradient at the edge could lead to an ion bootstrap current which is not fully compensated by the electrons because of their trapped fraction. This could change the current density profile. In the case of a sawtooth-triggered H-transition, the steep edge gradients develop rather quickly and one would expect to see an increase in the plasma current till the OH feedback system restores the previous current level. No such transient increase in current is observed in the experiment.
The advantage afforded for MHD stability by broad current profiles with pedestals at the edge and with reduced j-gradients in the bulk is well established /37/. What is unclear is how the improved stability for macroscopic modes couples into the microscopic turbulence. There is a great deal of literature available on this subject, which is also discussed in conjunction with the degradation of confinement in the L-mode and the observed resiliance of the T_e-profile against any changes by auxiliary heating /38/.
A broader density profile in the bulk plasma which develops when the gradient is shifted into the edge could stabilize drift-like turbulene and improve confinement in the outer half of the plasma (this possibility is investigated in Ref. 39). It is interesting to note in conjunction with the density profile shape that under counter-NI conditions rather peaked density profiles develop with gradients much above those even of the L-regime. H-transitions nevertheless also accour under these profile conditions.

In order to compare the different theoretical concepts proposed for the improvement of confinement in the H-phase with experimental results, these models have to be put into transport codes. This is done in Ref. 39 and the time evolution of the plasma, in particular of its energy content, is studied. The transport model contains conceptually the driving mechanisms of steep density and pressure gradients (via drift, rippling, and resistive ballooning modes) and includes the stabilization of increased shear at the edge. The heat transport coefficient χ_e is semi-empirically constructed with an ohmic part $\alpha\ n_e^{-1}\ T_e^{-0.5}$ and an auxiliary heating part proportional to pressure. The model describes the L-phase owing to the pressure term in χ_e and yields an H-transition if the density in the plasma periphery can be increased by a separate mechanism. The increase in density allows the ohmic contribution to χ_e to drop, being supported by the favourable temperature dependence. The pressure gradients which evolve in this phase are moved toward the high shear region. The transition in the model occurs

within 2-3 ms as is observed in the experiment. The trigger mechanism which initiates this involved process has to come from the outside. Possibilities will be discussed in the next section.

6.4.3. Potential H-mode triggers

6.4.3.1. Thermal barrier in the s.o.l.

The model is based on the experimental observation of a hot plasma edge and the resulting high-power fluxes along the s.o.l. with collisionless heat-carrying electrons. It is proposed /40/ that a low power flux can be maintained if the hot electrons do not reach the target plates owing to an electrostatic barrier in the s.o.l. It can develop in the vicinity of the target plate where the electron temperature decreases. Such a potential barrier can reflect the cold electrons. The heat flow along the s.o.l. is reduced when the hot electrons from the plasma are separated from the cold ones by the barrier, which prevents the backflow of cold electrons.
The proposed mechanism requires the sudden development of this electrostatic potential at the H-transition. A strong increase of the ionization rate in front of the target plate is expected to provide the high recycling conditions and the high local density. The temperature of the cold electrons still has to be sufficiently high to provide collisionless conditions for the separation of the two electron components. The electron temperature in the s.o.l. of the main plasma has to increase on account of the parallel thermal resistance.

Experimentally, the opposite is observed: the H_α-radiation in the divertor chamber and T_e in the s.o.l. decrease. The possibility of a parallel thermal resistance crucially depends on the exact localization of the high temperature region at the plasma periphery, i.e. - whether it is inside or outside the separatrix. The required accuracy of the experimental results can be doubted because localization of the separatrix in the plasma mid-plane is mostly done by equilibrium calculations, which do not give the separatrix position in the mid-plane to better than ±1 cm (corresponding to a fall-off length in the s.o.l.). Nevertheless, the results from ASDEX indicate that the high temperature zone and the steep gradients are located inside the separatrix; this result also gives more consistency in all the various s.o.l. and divertor plasma measurements. Other experiments operating in the H-mode confirm the location of the steep gradient zone inside the separatrix, too /5, 41/. The thermal resistance therefore seems to be located inside the separatrix, and the perpendicular and not the

parallel heat flow seems to be impeded. As a consequence of the edge barrier, the plasma parameters in the s.o.l. and the divertor plasma drop at the H-transition.

6.4.3.2. Particle blocking in the s.o.l.

The effect of particle blocking is based on a two-step process: if one succeeds in increasing the density in the steep gradient region and in reducing the gradients there - as described in Sect. 4.4.2. - one can expect some type of drift wave turbulence to disappear. It is proposed in Ref. 39 that a sudden increase of ionization in the divertor chamber causes the peripheral plasma density to rise and, in combination with the high pressure in the divertor chamber which develops during the preceding L-phase, reduces the particle outflow of the main plasma. Consequently, the local edge density is increased but the gradients of the bulk are decreased to such an extent that transport is reduced. The H-transition is triggered in this model by the sudden development of high recycling conditions, and the drop of T_e in the divertor chamber at the H-transition is seen as experimental evidence.

The model is led by the experimental observation of increased density in the plasma periphery and reduced density gradients. The trigger mechanism would require, however, transition into high-recycling conditions in front of the target plates which should transiently increase H_α in the phase when the electron temperature is reduced. As a consequence of the high-recycling conditions, the density in the s.o.l. should increase. Experimentally, a parameter variation at the H-transition is observed which does not agree with the expectations for the transition into high recycling. The H_α-radiation does decrease at all locations which are relevant for recycling changes (see Fig. 15); the decrease of T_e in the divertor chamber is not accompanied by an increase in density, but rather the density is observed to decrease in the s.o.l. and the divertor chamber. The experimental results rather indicate that the rise in the plasma periphery is corollary to the H-transition and is caused by an improvement of particle confinement instead of a transiently increased source term.

6.4.3.3. Effect of collisionality on the edge ion transport

Bifurcation in the ion energy transport is possible /42/ when the collisionality decreases during heating and the plasma ions enter the collisionless regime: the ion energy transport mechanism across the separatrix then changes. Under collisionless conditions, ions have to be scattered onto

diverted drift orbits which guide them into the divertor chamber. The ion loss rate is then determined by ion-ion collisions into the loss cone; the ion temperature gradient develops according to the flux continuity of neoclassical ion heat flow from the bulk plasma and to the ion energy loss rate due to scattering into the loss cone. T_i-gradients of several hundred eV/cm are estimated as observed experimentally for T_e-gradients. The absolute value of T_i develops inversely to the particle flow across the separatrix and can be high with good particle confinement. A possible process relating the electron transport, variation of which causes L- and H-mode confinement features, to the ion energy transport was discussed in the previous section in conjuntion with changes of the current distribution induced by an ion bootstrap current at the edge.

At the plasma edge the radial ion energy transport, under normal conditions, occurs through diffusion and charge exchange processes. If the edge neutral density is kept low, however, as may be the situation in the divertor configuration, where recycling predominantly occurs within the divertor chamber neoclassical ion heat conduction may indeed prevail up to the separatrix.

The detrimental role of enhanced recycling and gas puffing has been experimentally observed. In both PDX /5/ and ASDEX it has been observed that gas fuelling from the divertor dome instead of the main plasma chamber facilitates the H-transition. Excessive gas puffing could quench the H-phase of PDX, yielding low confinement. ASDEX obtains the H-mode with hydrogen neutral injection into hydrogen plasmas if the location of the external gas flux - required to maintain constant density - is moved from the main plasma into the divertor chamber. The experiments on PDX have further revealed that the H-phase is only possible with the closed divertor configuration when the molecular hydrogen backflow from the divertor into the main plasma space is reduced. The detrimental effect of the proximity of a material limiter was discussed in Sect. 6.1.2. The limiter prevents the transition into the H-phase at a distance corresponding to about two scrape-off layer fall-off lengths. At this distance, impurity erosion may still be low, while the local neutral density at the limiter has already increased (in the ohmic phase by a factor approximately five). Like the electron temperature, the ion temperature T_i increases after the H-transition.

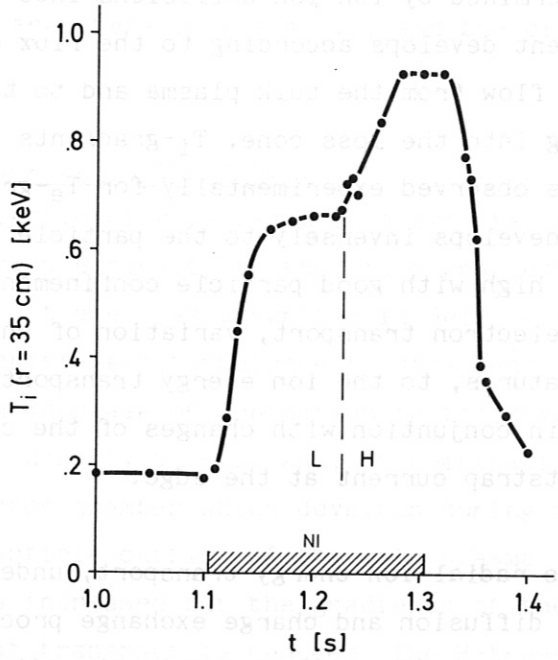

Fig. 50 Time depencence of ion temperature at plasma periphery (r = 35 cm = (7/8a) during neutral-injected pulse. L- to H-transition is indicated. I_p = 0.3 MA; B_T = 2.2 T; P_{NI} = 2.5 MW.

Figure 50 shows the time dependence of T_i in ASDEX at r = 35 cm (≈7/8 a). The H-transition is clearly marked by a sudden further rise of T_i from the plateau value of the preceding L-phase. A steep T_i-gradient develops. Figure 51 shows the ion and electron collisionality parameter ν_e^* deduced from electron and ion temperature profiles measured just prior to the H-transition and 100 ms after it. The ion collisionality parameter at the plasma edge is slightly above one in the L-phase and clearly drops below one after the H-transition. The electron collisionality parameter ν_e^* at the plasma edge is about one in the L-phase and about 0.4 in the H-phase.

These measurements indicate that electrons and ions are close to collisionless conditions even at the plasma edge and a steep T_i-gradient develops after the H-transition. In the pre-transition L-phase the collisionality parameters are close to 1. The actual collisionality parameters are higher because the singularity in q of the separatrix configuration has not been included in the ν^* calculation of Fig. 51. Despite these uncertainties it is very possible that the the collisionality regime at the plasma edge is changed at the H-transition.

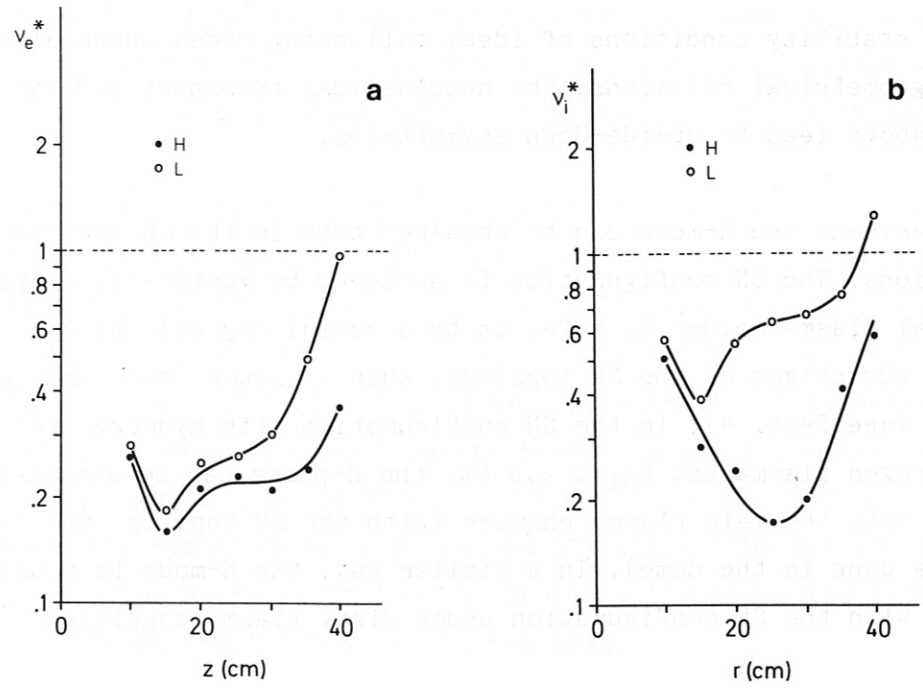

Fig. 51 Electron- and ion-collisionality parameters deduced from the measured profiles. The transition from the plateau into the collisionless regime is indicated; P_{NI} = 3.3 - 3.5 MW; B_T = 2.2 T; (a) I_p = 0.31 MA; (b) I_p = 0.38 MA.

At low collisionality an interesting situation occurs since there are two solutions possible for the neoclassical ion energy transport across the separatrix - a low-gradient and a high-gradient solution /42/. The specific features of neoclassical ion transport in the vicinity of a separatrix with an X-point represents the sink for the heat flux, which crosses the separatrix and flows along the s.o.l. The presence of an X-point can change the radial thermal ion flux because the Pfirsch-Schlüter heat currents in the flux surfaces either flow parallel to the global flux onto the X-point or opposite to this flux. At a given heat flux through the separatrix, the parallel fluxes give rise to low T_i-gradients, while the anti-parallel fluxes cause steep gradients. The direction of the parallel Pfirsch-Schlüter heat currents depends on the ion grad-B drift. If it is in the direction of the X-point, steep gradients develop and the H-transition should be facilitated; away from the X-point the H-transition is aggravated. In the symmetric double-null configuration with 2 X-points these geometrical effects should just cancel. At high heating power these aspects again play no role because the heat transport under collisionless conditions is not affected by the X-point topology.

Unlike the stability conditions of ideal ballooning modes which also introduce geometrical relations, the neoclassical transport effects as described above lead to upside-down asymmetries.

In the experiment the H-mode can be obtained both in the SN and the DN configurations. The SN configuration is achieved by vertically displacing the toroidal plasma column by a few cm by a radial magnetic field. There are severe advantages of the SN topology, such as lower power and density thresholds (see Sect. 4); in the SN configuration with hydrogen injection into a hydrogen plasma and $P_{NI} \geq 2.5$ MW, the H-phase can be obtained with refuelling into the main plasma chamber (with the DN topology the refuelling must be done in the dome). In a similar way, the H-mode is found to be accessible with the SN configuration under dirty plasma conditions (e.g.

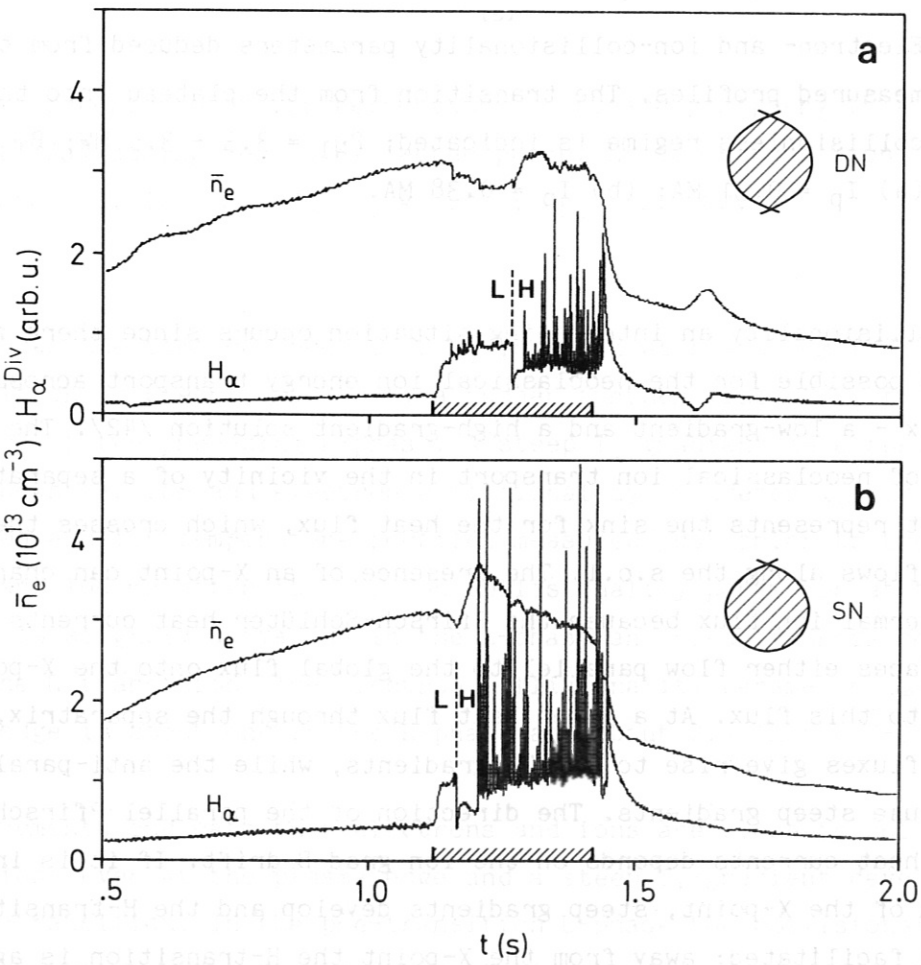

Fig. 52 Comparison of L- to H-transition of two consecutive shots (#15564 and #15565), one being a double-null (DN) and the other a single-null (SN) discharge. Vertical displacement of SN discharge is 1 cm. I_p = 0.31 MA; B_T = 2.2 T; P_{NI} = 3.5 MW.

resuming operation after the vessel has been vented), when the development of the edge electron temperature is impeded by impurity radiation and the available heating power is insufficient to produce it in the DN geometry.

In the SN configuration, the L-phase preceding the H-transition is always observed to be shorter than in a DN plasma with the same plasma and beam parameters. Two subsequent discharges - one a DN, the other an SN plasma - are compared in Fig. 52. The vertical displacement is 1 cm in the case shown in Fig. 52b and corresponds to a typical (density or temperature) fall-off length in the scrape-off layer. Figure 52 plots the line-averaged density and H_α-D_α-radiation in the divertor chamber. The drop in H_α-D_α-radiation and the simultaneous rise in density (till ELMs set in) mark the transition into the H-phase. In the DN topology, the preceding L-phase is 150 ms and is shortened to 45 ms in the SN case.

The most important aspect of Hinton's theory is the expected impact of the ion grad-B drift direction on the H-transition, which is indeed observed experimentally. Figure 53 shows an operational diagram of the H-phase with

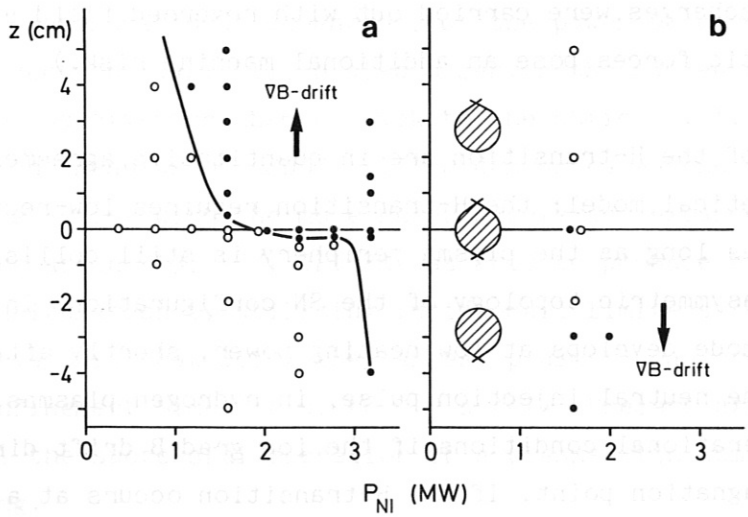

Fig. 53 Operational diagram for L- and H-discharges (H^0-injection into D^+-plasmas). z is vertical plasma position; z > 0; upper SN; z = 0: DN; and z < 0: lower SN configuration. P_{NI} is the beam power into vessel. The arrows indicate ion grad-B drift direction; the curve in (a) denotes operation boundary between L- and H-discharges and insert to (b) indicates plasma configuration. Solid points: H-, circles: L-discharges.

respect to power and vertical plasma position (determining plasma configuration). Centred (z=0) plasmas are DN discharges, while those shifted upward (downward) are upper (lower) SN plasmas (see insert to Fig. 53). The solid points in Fig. 53 denote H-plasmas, the open circles L-discharges, and the arrows indicate the ion grad-B drift direction.
As predicted in Ref. /42/, the H-regime can be obtained at high beam power, when even the plasma edge becomes collisionless irrespective of the symmetry of stagnation points or the ion grad-B drift direction. Figure 53 also documents that the DN configuration requires more power than the SN topology (e.g. the cases at z=4 cm) to allow the H-mode, provided that the ion grad-B drift direction is correct. For positive vertical displacements, when the ion grad-B drift direction is towards the stagnation point, H-discharges are obtained, while in the lower SN topology, with the ion grad-B drift direction away from the stagnation point, only L-discharges are obtained at medium heating power levels.
When the toroidal field is reversed (the direction of the plasma current is the same to maintain the co-injection geometry), the upper SN plasmas are L-discharges, while the lower SN plasmas - now with the ion grad-B drift towards the (lower) stagnation point - mostly turn out to be H-plasmas. (Only a few discharges were carried out with reversed field since the reversed magnetic forces pose an additional machine risk.)

Many features of the H-transition are in quantitative agreement with Hinton's theoretical model: the H-transition requires low-recycling conditions and - as long as the plasma periphery is still collisional (at low beam power) - asymmetric topology of the SN configuration. In an SN discharge, the H-mode develops at low heating power, shortly after the beginning of the neutral injection pulse, in hydrogen plasmas, and even under dirty operational conditions if the ion grad-B drift direction is towards the stagnation point. If the H-transition occurs at a critical gradient (which requires a critical T_i-gradient), the existance of a power threshold is predicted.

7. Summary

The unique feature of the H-mode is the development of a transport barrier close to, but inside, the separatrix that is characterized by lower energy and particle transport coefficients. The prerequisite of the transport barrier seems to be the achievement of a high edge electron temperature. The main characteristics of the H-mode follow as a consequence of the transport barrier, such as the steep edge gradients, the broad profiles and an MHD spectrum which is determined by improved central stability against current gradient driven modes, but at the expense of a new type of edge instability.

A possible evolution of an H-discharge could be the development of collisionless conditions up to the separatrix, which act as a trigger, and the development of steep gradients at the edge supported by increased shear and electron temperature, which allow reduced gradients in the bulk plasma with less free energy to drive turbulence. In the meantime, several experiments operate successfully in the H-mode. The importance of the plasma edge for the H-transition, the correlation with the edge electron temperature, and the existence of a power limit for the H-mode are confirmed. JFT-2M reproduced the configurational dependence of the power threshold on the ion grad-B drift direction /44/; DIII-D also observes the sudden drop of the power flow into the divertor chamber back to the ohmic level.
In addition to the results of ASDEX, DIII-D demonstrated the successful operation of the H-mode with the more reactor-relevant expanded boundary divertor configuration /13, 45/. JFT-2M was able to produce the H-mode in the limiter configuration by utilizing inside rail limiters /46/. Most important, however, is that JET - the largest plasma - can operate in the H-mode with confinement times of up to 0.9 s /47/. Present extrapolations predict for JET the successful operation of a plasma with dominant α-particle heating.
But there are still severe problems. The quiescent nature of the H-mode without ELMs and sawteeth allows uncontrolled impurity accumulation; in this regime there is also no technical means available to control the density rise. The question of a power dependance of τ_E in the H-phase has not been finally clarified. The intrinsic transport of the H-mode as displayed in the ELM-free version could be such that the global confinement time assumes a power dependence like the L-mode. The results from JET and JFT-2M indicate this trend. ELMs in the H-mode could pose an additional challenge to construction of the divertor hardware, which has to sustain the intense power pulses.

References

/1/ F. Wagner, G. Becker, K. Behringer, D. Campbell, A. Eberhagen et al., Phys. Rev. Lett. 49 (1982) 1408.

/2/ F. Wagner, G. Becker, K. Behringer, D. Campbell, A. Eberhagen et al., Plasma Phys. and Contr. Nucl. Fusion Research, Vol. 1, IAEA, Vienna (1983) p. 43.

/3/ M. Keilhacker, G. Becker, K. Bernhardi, A. Eberhagen, M. ElShaer et al., Plasma Physics and Controlled Fusion, 26 (1984) 49.

/4/ O. Gruber, W. Jilge, K. Bernhardi, A. Eberhagen, G. Fußmann et al., Proc. 12th Europ. Conf. on Contr. Fusion and Plasma Phys., Budapest, part I, p. 18 (1985).

/5/ S.M. Kaye, M.G. Bell, H. Bol, D. Boyd, K. Brau, Jour.Nucl. Mat. 121 (1984) 115.

/6/ J. Luxon et al., 11th Intern. Conf. on Plasma Phys. and Controlled Nucl. Fusion Research, IAEA, Vienna, Vol. I (1987) p. 159.

/7/ K. Odajima et al., 11th Intern. Conf. on Plasma Phys. and Controlled Nucl. Fusion Research, IAEA, Vienna, Vol. I (1987) p. 151.

/8/ A. Tanga et al., 11th Intern. Conf. on Plasma Phys. and Controlled Nucl. Fusion Research, IAEA, Vienna, Vol. I (1987) p. 65.

/9/ F. Wagner et al., "Confinement and β_p-Studies in Neutral Injection Heated ASDEX Plasmas", Report IPP III/86 (1983).

/10/ K. McCormick, Z.A. Pietrzyk, H. Murmann, G. Becker, H.-S. Bosch et al., Proc. 14th Europ. Conf. on Contr. Fusion and Plasma Phys., Madrid, part II, p. 666 (1987).

/11/ F. Wagner et al., "Variation of the Particle Confinement during Neutral Injection into ASDEX Divertor Plasmas", Report IPP III/78 (1982).

/12/ F. Wagner et al., "Variation of the Particle Confinement during Neutral Injection into ASDEX Divertor Plasmas", Report IPP III/78 (1982).

/13/ K.H. Burrell, S. Ejima, D.P. Schissel, N.H. Brooks, R.W. Calles, Phys. Rev. Lett. 59 (1987) 432.

/14/ M. Keilhacker et al., Proc. 10th Intern. Conf. on Plasma Phys. and Controlled Nucl. Fusion Research, IAEA, Vienna, Vol. I, p. 71 (1985).

/15/ R. Müller, G. Janeschitz, P. Smeulders, G. Fußmann, submitted to Nucl. Fusion.

/16/ H. Niedermeyer, F. Wagner, G. Becker, K. Büchl, A. Eberhagen, Proc. 11th Int. Conf. on Plasma Phys. and Contr. Nucl. Fusion Research, IAEA, Vienna, Vol. I (1987), p. 125.

/17/ G. Becker, ASDEX-Team, Neutral Injection Team, Nucl. Fusion 22 (1982) 1589.

/18/ A. Stäbler, F. Wagner, G. Becker, K. Bernhardi, U. Ditte et al., 4th Intern. Symp. on Heating in Tor. Plasmas, Rome (1984), Vol. I, p. 3.

/19/ O. Gruber, Proc. Invited Papers. Intern. Conf. on Plasma Phys., Lausanne (1984) Vol. I, p. 67.

/20/ S.M. Kaye, Phys. Fluids 28 (1985) 2327.

/21/ S.M. Kaye, R.J. Goldston, Nucl. Fusion 25 (1985) 65.

/22/ R.J. Fonck et al., Proc. 4th Symp. on Heating in Toroidal Plasmas, Rome, (1984) Vol. I, p. 37.

/23/ G. v.Gierke, M. Keilhacker, R. Bartiromo, G. Becker, A. Eberhagen et al., Proc. 12th Europ. Conf. on Contr. Fusion and Plasma Phys., Budapest, part I (1985) 331.

/24/ O. Gruber, G. Becker, G. v.Gierke, H. Grassie, O. Klüber et al., Proc. 11th Intern. Conf. on Plasma Phys. and Controlled Nucl. Fusion Research, IAEA, Vienna (1987) Vol. I, p. 357.

/25/ F. Troyon et al., Plasma Physics and Controlled Fusion 26 (1984) 49.

/26/ G. v.Gierke, G. Becker, H.-S. Bosch, K. Büchl et al., Proc. 13th Conf. on Contrl. Fusion and Plasma Phys., Schliersee, part I (1986) p. 33.

/27/ K. Steinmetz, J.-M. Noterdaeme, F. Wagner, F. Wesner et al., Phys. Rev. Lett. 58 (1987) 124.

/28/ F. Leuterer, F.X. Söldner, D. Eckhartt, A. Eberhagen et al., Plasma Physics and Controlled Fusion 27 (1985) 1399.

/29/ M. Kaufmann et al., submitted for publication to Nucl. Fusion.

/30/ F. Wagner, M. Keilhacker, ASDEX and NI teams, Jour.Nucl. Mat. 121 (1984) 193.

/31/ H. Eubank, R.J. Goldston, V. Arunasalam, M. Ritter, K. Bol et al., Plasma Phys.and Controlled Nucl. Fusion Research, IAEA, Vienna (1979) 167.

/32/ F. Wagner, G. Fußmann, T. Grave, M. Keilhacker, M. Kornherr et al., Phys. Rev. Lett. 53 (1984) 1453.

/33/ C.M. Bishop, et al., Phys. Fluids 24 (1984) 1579.

/34/ C.M. Bishop, Nucl. Fusion 26 (1986) 1063.

/35/ T.S. Hahn, P.H. Diamond, Phys. Fluids 30 (1987) 133.

/36/ F.L. Hinton, preprint

/37/ A.H. Glasser, H.P. Furth, P.H. Rutherford, Phys. Rev. Lett. 38 (1987) 234.

/38/ H. Furth, Plasma Physics and Controlled Fusion, 28 (1986) 1305.

/39/ C.E. Singer et al., Nucl. Fusion 25 (1985) 1555.

/40/ T. Ohkawa et al., Phys. Rev. Lett. 51 (1983) 2101.

/41/ K. Hoshino, T. Yamamoto, H. Kawashima, T. Yamanchi, Y. Uesugi, Jour. Phys. Soc. of Japan 56 (1987) 1750.

/42/ F.L. Hinton, Nucl. Fusion 25 (1985) 1457.

/43/ F. Wagner, R. Bartiromo, G. Becker, H.-S. Bosch, A. Eberhagen et al., Nucl. Fusion 25 (1985) 1457.

/44/ N. Suzuki, Y. Miura, M. Hasegawa, K. Hoshino, S. Kasai et al., Proc. 14th Europ. Conf. on Contr. Fusion and Plasma Phys., Madrid (1987), Vol. I, p. 9.

/45/ M. Shimada, K.H. Burrell, S. Ejima, B.P. Schissel, S. Allen et al., Proc. 14th Europ. Conf. on Contr. Fusion and Plasma Phys., Madrid (1987), Vol. I, p. 9.

/46/ M. Matsumoto, A. Fumakoshi, M. Hasegawa, K. Hoshino, S. Kasai, Proc. 14th Europ. Conf. on Contr. Fusion and Plasma Phys., Madrid (1987), Vol. I, p. 5.

/47/ M. Keilhacker, C.M. Bishop, J.G. Cordey, D.G. Muir, M.L. Watkins, Proc. 14th Europ. Conf. on Contr. Fusion and Plasma Phys., Madrid (1987), Vol. III, p. 1339.

Acknowledgement

Die Arbeit in der experimentellen Fusionsforschung an Tokamak Experimenten der Größe von ASDEX erfolgt in teams. Es sind Wissenschaftler, die die Maschine samt ihrer Peripherie betreiben, die mit komplexen Diagnostiken die Daten gewinnen und sie interpretieren. An einem derartigen Experiment herrscht ein hohes Maß an Arbeitsteilung. Deshalb hängt der Fortschritt in der experimentellen Fusionsforschung an der erfolgreichen Zusammenarbeit in einem solchen team, und der Erfolg des einzelnen wird zu einem hohen Maß von der Qualität der Zuarbeit anderer bestimmt.

Aus diesen Gründen möchte ich mich zunächst bei meinen Kollegen vom ASDEX team bedanken für die Unterstützung in meinem Interessengebiet mit Meßergebnissen und Ideen. Es würde hier den Rahmen sprengen, wenn ich alle nennen wollte, auf deren Meßdaten oder Anregungen ich zurückgreifen konnte. Es soll aber erwähnt werden, daß die ECE-Messungen an ASDEX von Herrn Eberhagen, die der Liniendichte von Herrn Gehre, die Verunreinigungsmessungen von den Herren Fußmann und Müller, die Thomsonstreuung von Herrn Murmann, die Modenmessungen von den Herren Kornherr und Gernhardt, die Divertor- und Randschichtmessungen von den Herren Haas, McCormick, Siller, Grave, Ditte und Niedermeyer betrieben werden. Für den Betrieb an ASDEX ist Herr Rapp verantwortlich, die Neutralinjektion wird von den Herren Stäbler und Vollmer betrieben. Ein großer Teil der Transportanalysen stammt von Herrn O. Gruber. Ich möchte mich ferner bei all denen bedanken, die mich bei meiner Arbeit technisch unterstützt haben, wie Herr Sahner oder Herr G. Zimmermann, oder die weitgehend den Zwang des Programmierens von mir genommen haben, wie Frau Karl.

Mein Dank gilt insbesondere Herrn von Gierke und Herrn Keilhacker, die mir die Aufgabe stellten, an ASDEX den Plasmaeinschluß zu untersuchen und die mich in all diesen Jahren unterstützt und ermutigt haben. Ich wurde mit einem Thema betraut, das sich in den letzten Jahren weltweit als eines der wichtigsten Untersuchungsziele am Tokamak erwies, und wofür gerade ASDEX - wie sich zeigen sollte - die besten Voraussetzungen mitbrachte.

Zuletzt möchte ich Herrn Lackner für die langjährige Unterstützung und Beratung danken, für die ständige Bereitschaft mit Deutungen zu helfen und zu führen und gelegentlich dann einzuschreiten, wenn der Enthusiasmus des Experimentators die Grenzen des sicher Erkannten zu verletzen drohten.

Das vorliegende Manuskript ist umfangreich geraten. Ich möchte mich bei Frau Thormählen, Frl. Weller und Frau Volkenandt und Herr Henningsen für das Schreiben des Textes und die Erstellung der Bilder bedanken.